MASARYKOVA UNIVERZITA
PŘÍRODOVĚDECKÁ FAKULTA
ÚSTAV TEORETICKÉ FYZIKY A ASTROFYZIKY

Bakalářská práce

BRNO 2026 JAN MÜLLER

MASARYKOVA
UNIVERZITA
PŘÍRODOVĚDECKÁ FAKULTA
ÚSTAV TEORETICKÉ FYZIKY A ASTROFYZIKY

Modelování dynamických procesů centrálních galaktických oblastí

Bakalářská práce

Jan Müller

Vedoucí práce: Mgr. Ing. arch. Petr Kurfürst, Ph.D. **Brno 2026**

Bibliografický záznam

Autor: Jan Müller
Přírodovědecká fakulta, Masarykova univerzita
Ústav teoretické fyziky a astrofyziky

Název práce: Modelování dynamických procesů centrálních galaktických oblastí

Studijní program: Fyzika

Studijní obor: Astrofyzika

Vedoucí práce: Mgr. Ing. arch. Petr Kurfürst, Ph.D.

Akademický rok: 2025/2026

Počet stran: xiii + 90

Klíčová slova: Pozůstatky supernov, Aktivní galaktická jádra, Akreční disky, Superhmotné černé díry, Hydrodynamika, Orbitální dynamika, Numerické modelování.

Bibliographic Entry

Author:	Jan Müller Faculty of Science, Masaryk University Department of Theoretical Physics and Astrophysics
Title of Thesis:	Modelling dynamical processes in central galactic regions
Degree Programme:	Physics
Field of Study:	Astrophysics
Supervisor:	Mgr. Ing. arch. Petr Kurfürst, Ph.D.
Academic Year:	2025/2026
Number of Pages:	xiii + 90
Keywords:	Supernova Remnants, Active Galactic Nuclei, Accretion Disks, Supermassive Black Holes, Hydrodynamics, Orbital Dynamics, Numerical modeling.

Abstrakt

Tato bakalářská práce se zabývá numerickým modelováním expanze obálek supernov v extrémním prostředí akrečních disků aktivních galaktických jader. Pomocí 2D hydrodynamického kódu *Castro* simulujeme výbuch progenitoru o hmotnosti $15\,M_\odot$ u černých děr o hmotnostech 10^8 a $10^9\,M_\odot$ ve vzdálenostech 10^3 až 10^5 gravitačních poloměrů. Hlavním přínosem je zahrnutí eliptické dráhy hvězdy ($e = 0,6$), která rázové vlně uděluje významnou orbitální hybnost. Výsledky ukazují, že zatímco ve velkých vzdálenostech je expanze symetrická, v těsné blízkosti černé díry dominuje keplerovský střih a vysoká orbitální rychlost (v pericentru až 6×10^9 cm/s), což vede k extrémní deformaci morfologie pozůstatků supernov. Dále se věnujeme analytické rekonstrukci světelných křivek pomocí kódu *SEDONA*, přičemž výsledné profily vykazují strmý nárůst na přibližující se straně orbity v důsledku relativistického Dopplerova jevu. Tyto procesy doprovázené teplotami přes 10^9 K představují potenciální zdroje rentgenových signálů detekovatelných v galaktických jádrech.

Abstract

This bachelor's thesis investigates the numerical modeling of supernova envelope expansion within the extreme environments of Active Galactic Nuclei accretion disks. Using the 2D hydrodynamic code *Castro*, we simulate the explosion of a $15\,M_\odot$ progenitor near black holes with masses of 10^8 and $10^9\,M_\odot$ at radial distances ranging from 10^3 to 10^5 gravitational radii. The primary contribution of this work is the inclusion of an elliptical stellar orbit ($e = 0.6$), which imparts significant orbital momentum to the expanding shock wave. Our results demonstrate that while expansion remains largely symmetric at large distances, close proximity to the black hole leads to dominant Keplerian shear and high orbital velocities (reaching up to 6×10^9 cm/s at pericenter), resulting in extreme morphological distortion of the supernova remnant. Furthermore, we perform an analytical reconstruction of the light curves using the *SEDONA* code, demonstrating that the resulting profiles exhibit a steep rise on the approaching side of the orbit due to relativistic Doppler beaming. These processes, characterized by temperatures exceeding 10^9 K, represent potential sources of detectable X-ray signatures within galactic nuclei.

MUNI
SCI

MASARYKOVA UNIVERZITA
PŘÍRODOVĚDECKÁ FAKULTA
KOTLÁŘSKÁ 2, 611 37 BRNO
IČ: 00216224
DIČ: CZ00216224

ZADÁNÍ
BAKALÁŘSKÉ PRÁCE

Akademický rok: 2025/2026

Ústav:	Ústav teoretické fyziky a astrofyziky
Student:	Jan Müller
Program:	Fyzika
Specializace:	Astrofyzika

Ředitel *ústavu* PřF MU Vám ve smyslu Studijního a zkušebního řádu MU určuje bakalářskou práci s názvem:

Název práce:	Modelování dynamických procesů v centrálních galaktických oblastech
Název práce anglicky:	Modelling dynamical processes in central galactic regions
Jazyk práce:	angličtina

Oficiální zadání:
In central regions of galaxies there is a large number and great variety of objects and formations, both stellar and non-stellar. This increases the frequency and type of their interactions with the surrounding interstellar material and/or with each other, for example, the interaction of stars with the galactic disk or jets, the interaction of supernova expansion envelopes with individual morphologies, etc. The observed properties of such interactions provide a variety of insights, but to fully understand their nature, such processes need to be theoretically investigated and modelled, and the results then compared with observed data. The task of this bachelor thesis will be to model some selected type of interaction, such as the passage of a star through a galactic disk, processes that take place in the torus region, in the broad line region, interactions of supernovae in the dense central galactic region, etc.

Literatura:

FRANK, Juhan; Andrew KING a Derek J. RAINE. *Accretion power in astrophysics*. 3rd ed. Cambridge: Cambridge University Press, 2002, xiv, 384. ISBN 0521629578.

BINNEY, James a Scott TREMAINE. *Galactic dynamics*. 2nd ed. Princeton: Princeton University Press, 2008, xvi, 885. ISBN 9780691130279.

BRANCH, David a J. Craig WHEELER. *Supernova explosions*. Berlin, Germany: Springer, 2017, xix, 721. ISBN 9783662550526.

Vedoucí práce:	Mgr. Ing. arch. Petr Kurfürst, Ph.D.
Konzultant:	doc. RNDr. Michal Zajaček, Dr. rer. nat.
Datum zadání práce:	8. 1. 2025
V Brně dne:	29. 3. 2026

Zadání bylo schváleno prostřednictvím IS MU.

Jan Müller, 13. 11. 2025
Mgr. Ing. arch. Petr Kurfürst, Ph.D., 23. 11. 2025
RNDr. Luboš Poláček, 11. 12. 2025

Poděkování

Na tomto místě bych rád poděkoval svému vedoucímu bakalářské práce, Mgr. Ing. arch. Petr Kurfürst, Ph.D., za odborné vedení, cenné rady a čas, který mi věnoval během konzultací. Dále bych chtěl poděkovat své rodině a blízkým přátelům za jejich neutuchající podporu a trpělivost, kterou mi projevovali po celou dobu mého studia.

Prohlášení

Prohlašuji, že jsem svoji bakalářskou práci vypracoval samostatně pod vedením vedoucího práce s využitím informačních zdrojů, které jsou v práci citovány. Výpočetní zdroje byly poskytnuty projektem „e-Infrastruktura CZ“ (e-INFRA LM2018140) v rámci programu Projektů velkých infrastruktur pro výzkum, vývoj a inovace.

Brno 6. dubna 2026 . . . .

Jan Müller

Contents

Introduction

Galactic centers represent some of the most extreme physical laboratories in the universe, driven by the gravitational dominance of supermassive black holes (SMBHs). These central engines, known as active galactic nuclei (AGN), are characterized by massive, rotating accretion disks that function as both reservoirs for hot plasma and as birthplaces or hosts for dense stellar populations. Within these turbulent environments, two of the universe's most powerful astrophysical phenomena intersect: the explosive deaths of stars such as supernovae (SNe) and the tidal, hydrodynamic, and radiative forces governed by the central black hole.

Traditional models of supernova remnants (SNRs) typically describe their expansion into the diffuse and relatively inactive interstellar medium. In contrast, an SN occurring within an AGN accretion disk faces a radically different environment: steep vertical density gradients, rapid differential rotation following Keplerian dynamics, and the overwhelming gravitational field of the SMBH. Previous studies often simplify by assuming that the progenitor star is stationary with respect to the black hole; yet, the stellar dynamics near galactic centers are far more complex. Many stars follow highly eccentric orbits (e.g., $e = 0.6$), meaning that at the moment of core collapse, the resulting supernova inherits substantial orbital momentum from its progenitor.

Beyond the hydrodynamic and morphological evolution, a crucial component of this thesis is the numerical reconstruction of the light curves. These time-dependent radiation profiles serve as a bridge between theoretical simulations and real astrophysical observations. By post-processing our simulation data using a Monte Carlo radiative transfer code, we investigate how the geometric and dynamical asymmetries of the shock front — induced by disk density gradients, its Keplerian rotation, and orbital momentum — translate into observable characteristics. This approach allows us to identify observational signatures that can trace the presence of embedded SNe on eccentric orbits within AGN disks.

This thesis presents a systematic study of the hydrodynamic evolution of SN shocks in the vicinity of SMBHs with masses $M_\bullet$ of 10^8 and $10^9\,M_\odot$, as well as a lower-mass case modeled after Sgr A* ($4 \times 10^6\,M_\odot$). Using the *Castro* hydrodynamic code, we simulate explosions of SN progenitors of $15\,M_\odot$ at radial distances ranging from $10^3\,R_\mathrm{g}$ to $10^5\,R_\mathrm{g}$, where $R_\mathrm{g} = GM_\bullet/c^2$ is the gravitational radius of the SMBH. The primary focus is to examine how the orbital phase of the progenitor modifies the morphology of the resulting SNR. By explicitly incorporating orbital eccentricity ($e = 0.6$), we quantify how variations in orbital velocity between apocenter and pericenter lead to differential shearing and deformation of the shock front. The ultimate goal is to determine how orbital motion and local disk structure shape the energy distribution, morphology, and thermodynamic evolution of SNe embedded within accretion disks.

Chapter 1

Supernova Expansion in the High-Density Medium of the Galactic Disk

1.1 The Central Galactic Region

The central regions of galaxies, often referred to as galactic nuclei, host the most extreme conditions in the universe. High gas densities, strong radiation, and intense pressures make them very different from the calmer outer areas. This environment is key for modeling supernova (SN) feedback in the dynamical processes of galactic centers, as dense gas fundamentally changes how shock waves evolve.

1.1.1 Structure of Galactic Centers

Supermassive Black Holes

The discovery of quasars (QSOs) in the early 1960s fundamentally shifted our understanding of galactic energetics. The immense luminosities of these objects, often outshining their entire host galaxies by orders of magnitude, suggested a power source far more efficient than stellar nuclear fusion (Schmidt, 1963). It was proposed that this energy originates from the conversion of gravitational potential energy into radiation as matter accretes to a supermassive black hole (SMBH) (Lynden-Bell, 1969). Today, it is widely accepted that nearly every massive galaxy harbors such a central singularity, which remains dormant or active depending on the gas supply in its vicinity. The Event Horizon Telescope (EHT) collaboration, which produced the first-ever image of a black hole in 2019, provided an unprecedented look at the SMBH at the center of the galaxy M87 (Figure 1.1). This milestone was followed in May 2022 by the imaging of Sagittarius A*, the SMBH at the center of our own Milky Way galaxy (Event Horizon Telescope Collaboration, 2022), confirming the presence of a supermassive compact object at the heart of our Galaxy.

In general relativity, a non-rotating, spherically symmetric mass M is described by the Schwarzschild metric. The most critical feature of this metric is the Schwarzschild radius R_S, which defines the location of the event horizon, the limit from which no information

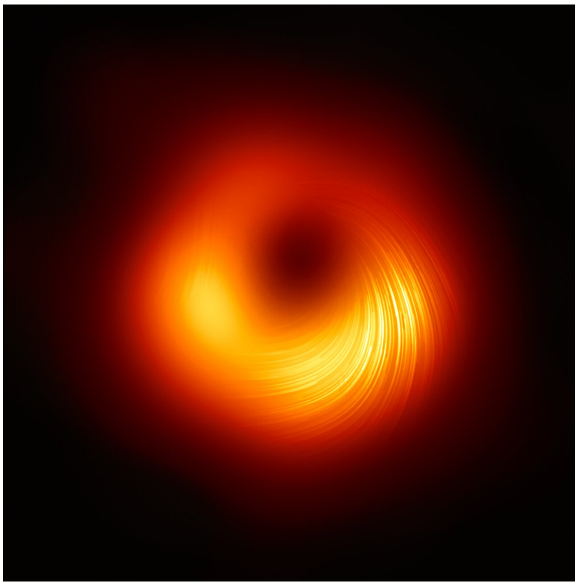

Figure 1.1: The polarized view of the SMBH in M87. The lines mark the orientation of polarization, which is related to the magnetic field around the shadow of the black hole (Event Horizon Telescope Collaboration et al., 2021).

or matter can escape. It is defined as

$$R_{\mathrm{S}} = \frac{2GM}{c^2}, \tag{1.1}$$

where G is the gravitational constant and c is the speed of light. Beyond the horizon, the innermost stable circular orbit (ISCO) at $r = 3R_{\mathrm{S}}$ represents the physical boundary of the hydrodynamic accretion disks. Inside this radius, stable circular motion is impossible, and matter plunges towards the singularity (Frank et al., 2002)(hereafter (F02)).

The luminosity of an active galactic nucleus (AGN) is governed by the competition between the inward pull of gravity and the outward push of radiation pressure. For a steady, spherically symmetrical accretion flow of fully ionized hydrogen, the Eddington luminosity L_{Edd} is the maximum luminosity a body can achieve when gravitational and radiational forces are in balance:

$$F_{\mathrm{grav}} = F_{\mathrm{rad}} \implies \frac{GMm_{\mathrm{p}}}{r^2} = \frac{\sigma_T L}{4\pi r^2 c}. \tag{1.2}$$

Solving for L gives the Eddington limit,

$$L_{\mathrm{Edd}} = \frac{4\pi GMm_{\mathrm{p}}c}{\sigma_T} \approx 1.3 \times 10^{38} \left(\frac{M}{M_\odot}\right) \mathrm{erg\ s^{-1}}. \tag{1.3}$$

In Equation (1.3), σ_T is the Thomson scattering cross-section and m_{p} represents the proton mass. If the accretion luminosity L exceeds L_{Edd}, the resulting radiation pressure can stop the inflow or drive massive outflows, providing critical feedback to the surrounding interstellar medium (ISM) (Rees, 1984).

The conversion of mass into radiant energy during accretion is far more efficient than stellar nucleosynthesis. The luminosity L produced by an accreting SMBH is proportional to the mass accretion rate as

$$L = \eta \dot{M} c^2, \tag{1.4}$$

where η is the radiative efficiency. The efficiency η ranges from 0.057 for non-rotating (Schwarzschild) black holes to nearly 0.42 for maximally rotating (Kerr) cases (F02). These values far exceed those of nuclear fusion (~ 0.007), making SMBHs the most potent energy sources in galactic evolution.

Nuclear Star Cluster

The nuclear star cluster (NSC) surrounds the central SMBH and forms the densest stellar environment in most galaxies, often outshining the rest of the galactic core. The NSC acts as a dynamic interface where gravitational energy, stellar evolution, and gas dynamics intersect. For the study of SN expansion, the NSC is critical because it provides both the massive star progenitors and the high-density medium required for the shock wave to propagate (Genzel et al., 2010).

In the Milky Way, the NSC is a compact, flattened stellar system with a total mass of approximately $2.5 \times 10^7\, M_\odot$ and a half-light radius of ~ 4 pc (Bland-Hawthorn and Gerhard, 2016). Its distinct visual morphology, coupled with the complex surrounding network of gas and dust from star formation, is illustrated in Figure 1.2. The NSC is characterized by a mixed stellar population, which we can divide into:

- **The old population (> 5 Gyr):** Comprising more than 80–90% of the cluster's mass, these late-type giants provide the long-term gravitational stability of the cluster.
- **The intermediate-age population (~ 50 Myr to a few Gyr):** Consisting roughly 5–15% of the mass, this component indicates that star formation in the galactic center was not halted after its initial formation, but rather proceeded episodically over the billions of years.
- **The young population (3-8 Myr):** A surprising concentration of over 100 massive stars resides in the central parsec. These massive stars are the progenitors of the SN explosions.

The sustenance of a central engine, whether it be a dormant singularity like the SMBH in the center of our Galaxy, Sgr A*, or a luminous AGN, requires a consistent influx of mass. Although high-luminosity quasars require accretion rates of $\dot{M} \approx 1 - 100\, M_\odot\, \mathrm{yr}^{-1}$, even less active nuclei rely on the NSC to channel gas into central regions (F02).

Within the dense environment of the NSC, gas is liberated from stars through several high-energy processes:

- **Normal stellar evolution:** Stars naturally lose mass mainly via stellar winds and SN explosions. The time-averaged rate for a typical cluster is $\approx 0.01\, M_\odot\, \mathrm{yr}^{-1}$. However, in the presence of frequent SNe, this gas is often heated and expelled from the cluster before it can be accreted (F02).

- **Tidal disruptions:** Stars whose orbits bring them within the “loss cone” of the SMBH are torn apart by tidal forces. This provides a sudden injection of gas; however, for very massive SMBHs ($M_\bullet > 10^8\,M_\odot$), stars may be swallowed whole without a significant release of radiation or gas.

- **Stellar collisions:** In the high-velocity environment of the NSC, physical collisions between stars frequently result in their disruption. The resulting debris can provide a significant mass supply, with feeding rates exceeding those of tidal disruptions by a factor of approximately $(v_c/v_*)^4$ (F02). Here, v_c represents the cluster velocity dispersion, which is the statistical spread of stellar velocities relative to the cluster's center of mass (characterizing the typical ”random” speed of stars within the NSC). The term v_* denotes the stellar escape velocity—specifically, the velocity required to escape the surface of an individual star (defined as $v_* = \sqrt{2GM_*/R_*}$). When v_c exceeds v_*, the kinetic energy of a collision is greater than the gravitational binding energy of the stars, leading to their total hydrodynamic disruption.

Ultimately, the NSC functions as a regulatory environment where the life cycle of massive stars dictates the thermal and dynamical state of the nuclear region. While the cluster provides the high-density medium and the stellar progenitors required for significant energy injection, their cumulative impact can drive large-scale galactic winds. By periodically clearing the gaseous reservoir of the NSC, this feedback effectively regulates the fuel supply available to the central SMBH, establishing a self-sustaining limit cycle of activity that governs the long-term evolution of the galactic nucleus (Morris and Serabyn, 1996).

The Central Molecular Zone

The central molecular zone (CMZ) represents a distinct high-pressure phase of the ISM found in the innermost regions of galactic nuclei. In the Milky Way, this region extends to a galactocentric radius of approximately 200 pc. Unlike the diffuse gas found in the broader galactic disk, the CMZ exists in a regime where the mechanical and thermal states of the gas are dictated by a precarious balance between self-gravity and intense external tidal forces. The existence of molecular clouds within this region necessitates an exceptionally high density to ensure gravitational stability. This requirement is expressed through a tidal stability criterion, where a density cloud ρ at a spherical galactocentric radius r can only remain bound if it exceeds the critical density (Morris and Serabyn, 1996)

$$\rho_{\rm crit} \approx \frac{2M(r)}{4\pi r^3}, \tag{1.5}$$

where $M(r)$ represents the mass enclosed within a sphere of radius r. The thermodynamics of the environment is further defined by the dominance of supersonic turbulence rather than thermal motion. The effective pressure can be expressed as

$$p_{\rm turb} \approx \rho\sigma_{\rm turb}^2, \tag{1.6}$$

where $\sigma_{\rm turb}$ is the 1D velocity dispersion. In the CMZ, $\sigma_{\rm turb}$ typically ranges from 15 to 50 $\mathrm{km\,s^{-1}}$, leading to a turbulent pressure significantly higher than the thermal pressure $p_{\rm th} = nk_{\rm B}T$. In this expression, n denotes the particle number density, $k_{\rm B}$ is the Boltzmann

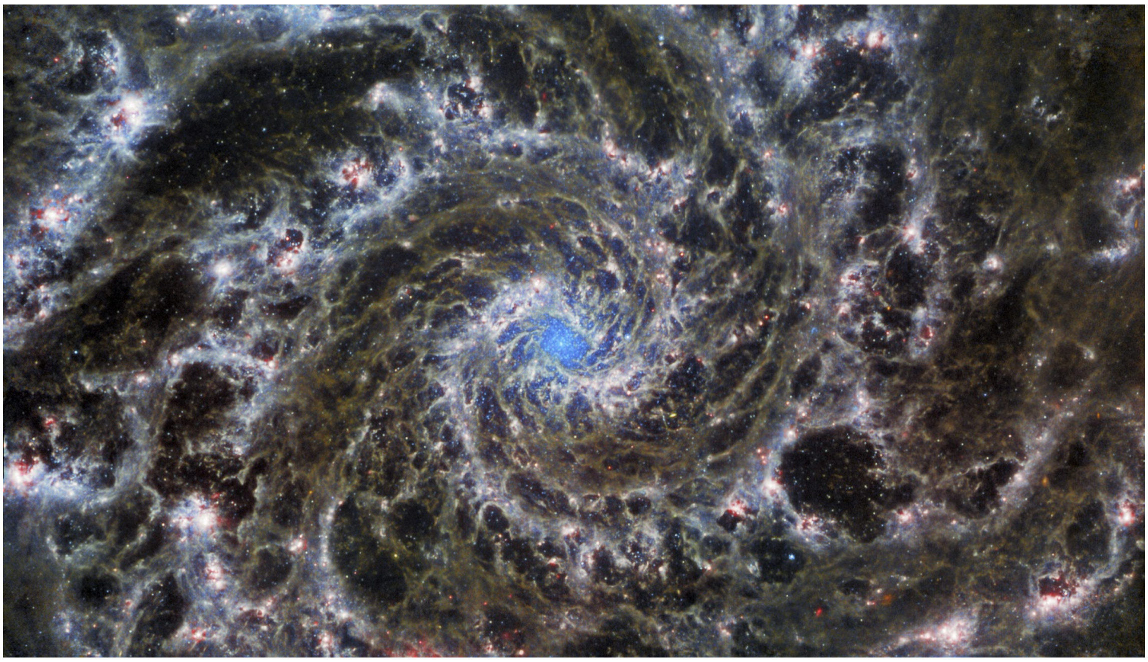

Figure 1.2: A mid-infrared (MIRI) view of the center of the nearby spiral galaxy (NGC 628) captured by the James Webb Space Telescope. The image reveals a detailed, complex network of dust and gas filaments within the central nuclear disk, where intense star formation is occurring. The bright blue core at the center corresponds to the location of a dense NSC. Credit: NASA, ESA, CSA, and STScI (2022).

constant, and T represents the local gas temperature. This high background pressure acts as a confining force for the gas, but also as a source of heating through the dissipation of turbulent kinetic energy,

$$\dot{E}_{\rm diss} \sim \frac{\rho \sigma_{\rm turb}^3}{L}. \tag{1.7}$$

In Equation (1.7), $\dot{E}_{\rm diss}$ represents the volumetric energy dissipation rate (energy per unit volume per unit time), and L is the characteristic scale of turbulence (Wilson et al., 1982). This mechanism leads to significant thermal decoupling, where the gas temperature ($T_{\rm gas} \approx 30 - 200\,{\rm K}$) remains substantially higher than the temperature of the coextensive dust particles (Morris and Serabyn, 1996).

From a hydrodynamic perspective, the high ambient density of the CMZ is very important for the evolution of energy injection, such as SN explosions. The radiative cooling rate per unit volume in the optically thin regime, λ, is proportional to the square of the particle number density n,

$$\lambda = n^2 \Lambda(T), \tag{1.8}$$

where $\Lambda(T)$ is the cooling function (Draine, 2011). The relation $\lambda \propto n^2$ implies that the energy loss becomes increasingly efficient in denser environments. The high cooling efficiency in such dense, yet optically thin environments is best characterized by the radiative cooling timescale, which defines the rate at which the internal energy of the gas is dissipated. This characteristic cooling time, $t_{\rm cool}$, is given by the relation (Binney and

Tremaine, 2008)

$$t_{\text{cool}} \approx \frac{3k_{\text{B}}T}{2n\Lambda(T)}. \tag{1.9}$$

In the CMZ, this timescale is several orders of magnitude shorter than in the diffuse ISM due to its dependence on the inverse of the number density n. Consequently, any SN blast wave that expands through this medium is subject to a rapid transition from its initial adiabatic expansion to a momentum-conserving radiative phase (Branch and Wheeler, 2017; Kurfürst, 2018). Such rapid energy dissipation effectively restricts the volumetric impact of the explosion while ensuring intense local processing of the molecular gas, which is a critical factor that must be taken into account in any dynamic model of the central galactic region (Binney and Tremaine, 2008). Observational evidence of such interactions is provided by radio imaging of the Milky Way's Galactic Center (Figure 1.3), where numerous SN remnants (SNRs) are detected expanding into the turbulent, high-density environment of the CMZ.

The Nuclear Gas Disk

Nuclear gas disks are dense reservoirs of molecular gas and dust, spanning the central 100-500 pc of galaxies. They represent the critical interface between the large-scale galactic disk and the immediate environment of the SMBH (Binney and Tremaine, 2008). An example of such a structure is the silhouette of a massive accretion disk, shown in Figure 1.4.

This subsection outlines the theoretical framework of a viscous nuclear gas disk, transitioning from fundamental conservation laws to vertical hydrostatic equilibrium and stationary approximations. The mathematical description follows the standard hydrodynamic formalism for thin disks.

Mass Conservation and Radial Transport: The radial structure of the disk is primarily governed by the conservation of mass. The surface density Σ is defined as the integral of the volume density ρ in the vertical direction,

$$\Sigma = \int_{-\infty}^{\infty} \rho \, \mathrm{d}z. \tag{1.10}$$

The radial mass conservation for an axisymmetric disk is expressed as

$$\frac{\partial \Sigma}{\partial t} + \frac{1}{R}\frac{\partial}{\partial R}(R\Sigma v_R) = 0. \tag{1.11}$$

In Equation (1.11), R represents the cylindrical radius (the distance from the z-axis), consistent with the coordinate system used in our hydrodynamic simulations (see also the supplementary explanations in Appendix A). As previously distinguished in the context of the CMZ, this cylindrical R differs from the spherical galactocentric radius r (Binney and Tremaine, 2008). Here, v_R denotes the radial velocity component within the disk plane. In the stationary approximation ($\partial/\partial t = 0$), mass conservation results in a constant mass-loss rate $\dot{M}$ throughout the disk (F02):

$$\dot{M} = 2\pi R\Sigma v_R = \text{const}. \tag{1.12}$$

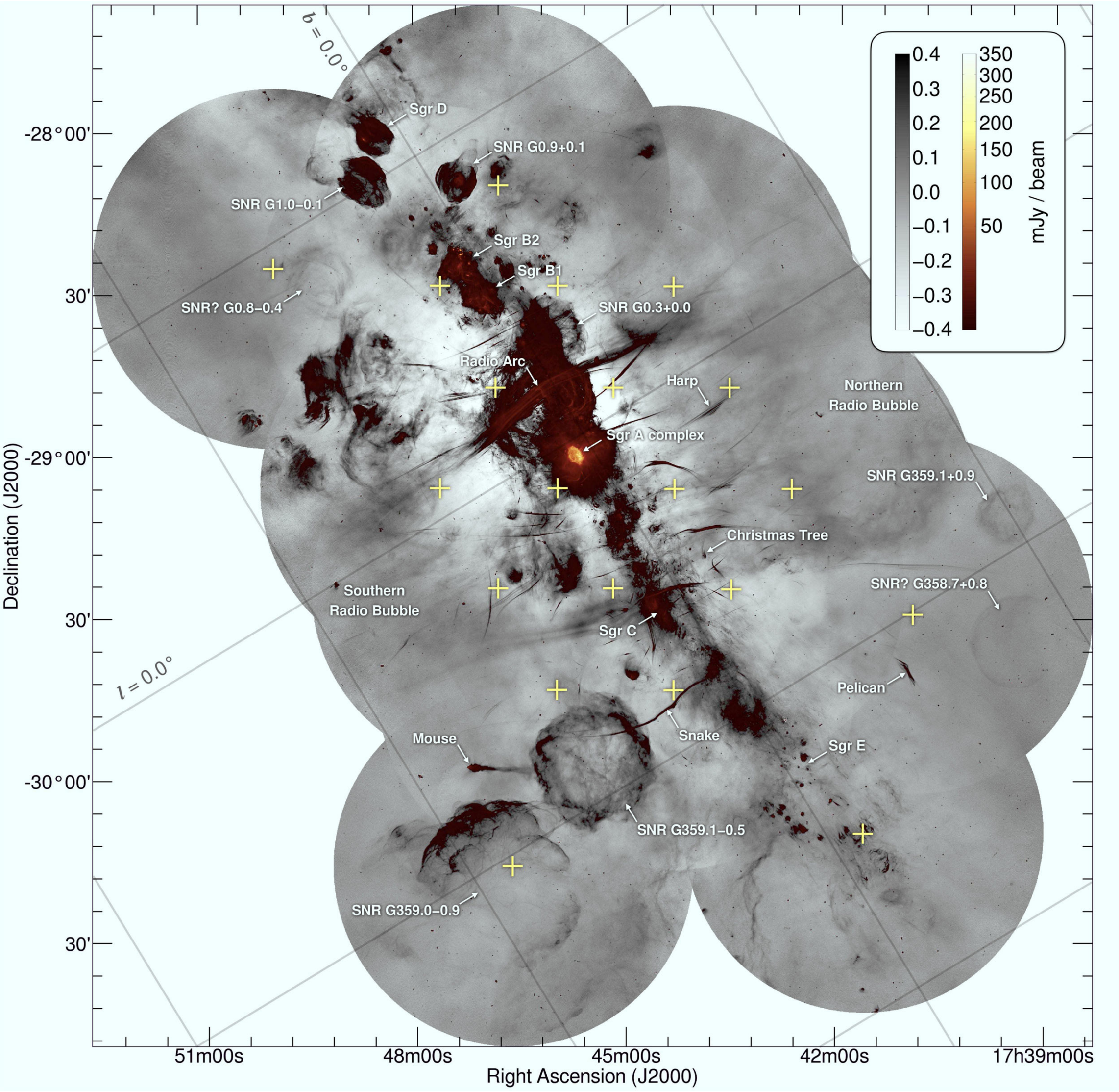

Figure 1.3: Detailed radio image (1.28 GHz) of the galactic center captured by the MeerKAT telescope. Visible features include regions of intense star formation (e.g., Sgr B2), the Sgr A complex surrounding the central SMBH, and numerous filamentary structures. Crucial to this work are the clearly identified SNRs (e.g., SNR G0.9+0.1), which interact with this extremely dense environment. Credit: Heywood et al. (2022).

The transport of angular momentum is driven by viscous torques acting between adjacent radial segments. The conservation equation for the angular momentum density is

$$\frac{\partial}{\partial t}(R\Sigma R^2\Omega) + \frac{1}{R}\frac{\partial}{\partial R}(R\Sigma v_R R^2\Omega) = \frac{1}{2\pi R}\frac{\partial G}{\partial R}. \tag{1.13}$$

The viscous torque $G(R)$, exerted by an outer ring on an inner ring, is defined as (F02)

$$G(R) = 2\pi R\nu\Sigma R^2\frac{\partial\Omega}{\partial R}, \tag{1.14}$$

where ν is the kinematic viscosity (see Equation (1.15) for its parameterization), and Ω is the angular velocity. The process of angular momentum transfer and radial mass flow is

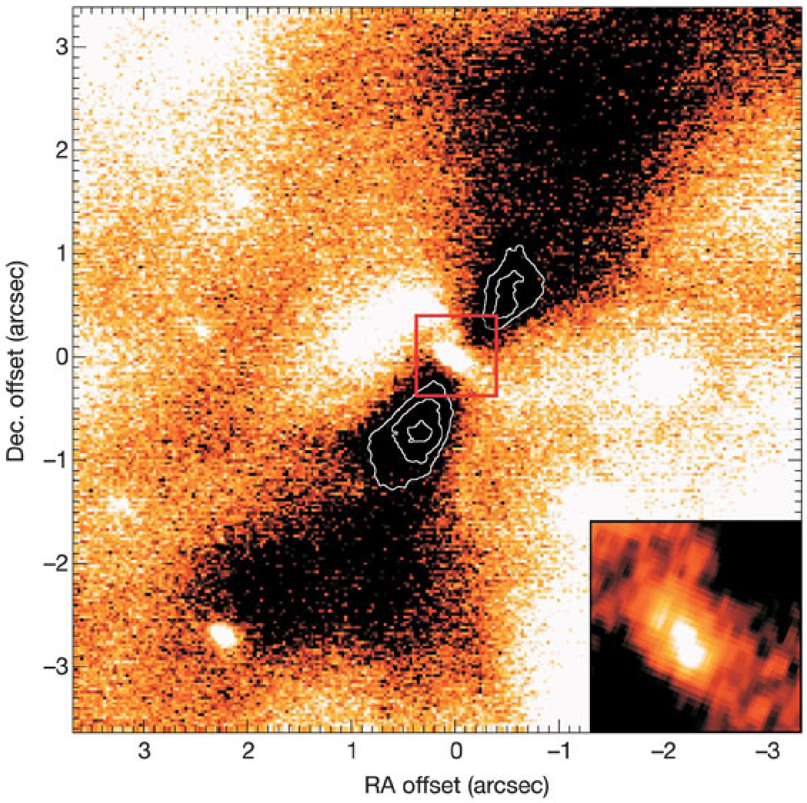

Figure 1.4: A silhouette of a massive accretion disk 20,000 AU in diameter, seen against the background light of an H II region. The white contours delineate the densest part of the disk, the inner torus. Credit: Chini et al. (2004).

shown in Figure 1.5.

The α-Prescription and Kinematic Viscosity: Because molecular viscosity is insufficient to produce large-scale viscous effects, macroscopic turbulent viscosity is used. Following Shakura-Sunyaev α-prescription (Shakura and Sunyaev, 1973), kinematic viscosity ν is parameterized using the sound speed a and the disk vertical scale height H defined as $H = a/\Omega = aR/v_\phi$:

$$\nu = \alpha a H \approx \alpha \frac{a^2 R}{v_\phi}, \tag{1.15}$$

where the parameter α is a dimensionless number that incorporates all uncertainties with respect to the viscosity mechanism. The value of α is generally expected to be less than unity, as higher values would lead to rapid thermalization via shocks. Although often assumed constant, α may decrease outward as a power law (Kurfürst et al., 2014):

$$\alpha = \alpha_0 \left(\frac{R_{\mathrm{eq}}}{R} \right)^n . \tag{1.16}$$

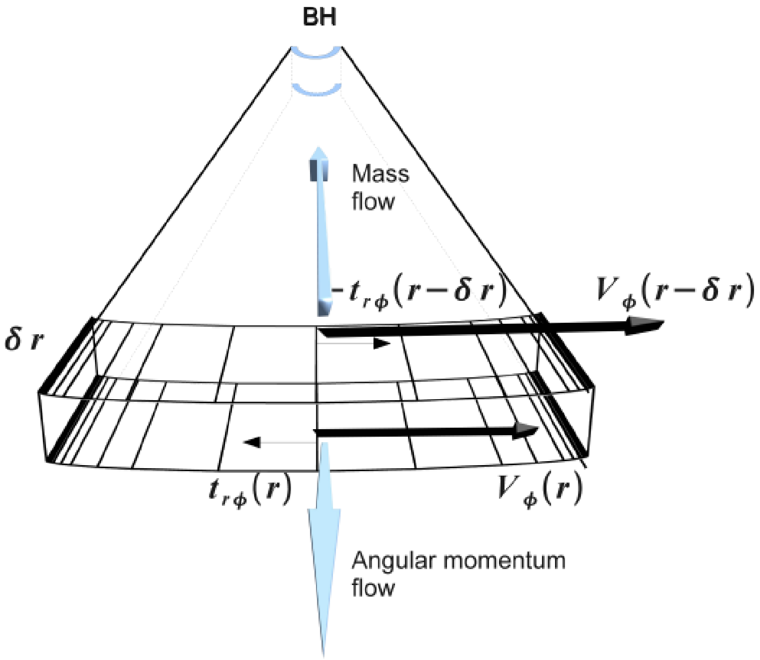

Figure 1.5: Schematic representation of transport in an accretion disk. Mass flows radially towards the central SMBH, while viscous torques transfer angular momentum outward. Credit: Mineshige et al. (2009).

Angular Momentum and Second-Order Viscosity: Angular momentum transport is driven by viscous torques resulting from the exchange of fluid parcels or gas eddies. The 2D axisymmetric conservation equation for the azimuthal component of momentum is

$$\frac{\partial}{\partial t}(R\rho v_\phi) + \frac{1}{R}\frac{\partial}{\partial R}(R^2\rho v_R v_\phi) = f^{(2)}_{\rm visc}. \tag{1.17}$$

The term $f^{(2)}_{\rm visc}$ in Equation (1.17) represents the full second-order Navier–Stokes viscosity term. This term is critical for preventing physically implausible backward rotational motion in the outer region of the disk (Kurfürst et al., 2014):

$$f^{(2)}_{\rm visc} = -\frac{1}{R}\frac{\partial}{\partial R}\left[\alpha a^2 R^2 \rho \left(1 - \frac{\partial \ln v_\phi}{\partial \ln R}\right)\right]. \tag{1.18}$$

In this formulation, the term in the inner bracket is equal to 3/2 for a Keplerian rotation profile ($v_\phi \propto R^{-1/2}$), and 2 for an angular momentum-conserving profile ($v_\phi \propto R^{-1}$), which is evident at large distances from the central object (Kurfürst et al., 2014, 2018).

Vertical Hydrostatic Equilibrium: The vertical structure is determined by the balance between the vertical pressure gradient and the vertical component of the central stellar gravitational acceleration g_z (Binney and Tremaine, 2008),

$$\frac{\mathrm{d}p}{\mathrm{d}z} = \rho g_z = -\rho \frac{GMz}{(R^2+z^2)^{3/2}}. \tag{1.19}$$

Assuming a vertically isothermal gas ($a = $const.), the density profile exhibits a Gaussian distribution centered on the midplane (F02):

$$\rho(R,z) = \rho(R,0)\exp\left(-\frac{z^2}{2H^2}\right). \tag{1.20}$$

The "thin disk" approximation, where $H \ll R$, implies that the local rotational velocity is highly supersonic ($v_\phi \gg a$).

Radial Dynamics and Gravitational Corrections: In the thin disk approximation, the cylindrical radial momentum conservation equation is expressed as

$$\frac{\partial v_R}{\partial t} + v_R \frac{\partial v_R}{\partial R} = \frac{v_\phi^2}{R} - \frac{GM}{R^2} - \frac{1}{\Sigma}\frac{\partial(a^2\Sigma)}{\partial R} + \frac{3}{2}\frac{a^2}{R}. \tag{1.21}$$

The term $3/2(a^2/R)$ serves as a correction for the decrease in the radial component of the gravitational force when moving away from the equatorial plane of the disk (Kurfürst et al., 2014). This term is of the same order as the pressure gradient and must be included in the cylindrical radial momentum equations for thin disks.

Thermal Structure and Viscous Dissipation: While disk temperature is primarily determined by stellar irradiation, viscous heating can dominate in the dense midplane of disks with very high mass-loss rates. The viscous heat flux F_{visc} per unit area is defined as (Shakura and Sunyaev, 1973; Frank et al., 2002)

$$F_{\mathrm{visc}}(R) = \frac{1}{4\pi R} G \frac{\partial \Omega}{\partial R} = \frac{9}{8}\frac{GM\nu\Sigma}{R^3}. \tag{1.22}$$

The vertical temperature gradient produced by dissipative heating is related to optical depth τ and opacity κ (F02):

$$\frac{\mathrm{d}T}{\mathrm{d}z} = \frac{3}{16\sigma T^3} F_{\mathrm{visc}} \frac{\mathrm{d}\tau}{\mathrm{d}z} = \frac{3}{16\sigma T^3} F_{\mathrm{visc}} \kappa\rho. \tag{1.23}$$

Under standard conditions for ideal monoatomic gases, convection is unlikely to develop in optically thick regions as the radiative gradient remains below the adiabatic limit.

Sonic Point Estimation: The radial velocity v_R increases until it reaches the sound speed at the sonic point radius R_{S}, where $v_R = a$. For a disk where the temperature follows a power law $T = T_0(R_{\mathrm{eq}}/R)^p$, the sonic point radius can be estimated as (Kurfürst et al., 2014)

$$\frac{R_{\mathrm{S}}}{R_{\mathrm{eq}}} \approx \left\{ \frac{3}{10+4p} \left[\frac{v_{\mathrm{K}}(R_{\mathrm{eq}})}{a(R_{\mathrm{eq}})} \right]^2 \right\}^{1/(1-p)}, \tag{1.24}$$

where p is the temperature power-law index ($T \propto R^{-p}$). Beyond this radius, the disk may no longer be Keplerian and typically tends toward angular momentum conservation (Krtička et al., 2011).

Self-Gravitational Instability and Clump Formation: In highly dense environments, the galactic nuclear gas disk may become self-gravitationally unstable. Such instabilities lead to the fragmentation of the disk into massive gas clumps with masses of approximately $10^4 - 10^5\,M_\odot$. These processes are probably behind the formation of star clusters in the CMZ (e.g., Arches or Quintuplet) (Morris and Serabyn, 1996; Genzel et al., 2010). The clumps can interact gravitationally, exchange angular momentum, and migrate towards the galactic center without being destroyed by the tidal forces of the SMBH.

1.2 Supernova Explosions

SNe are the primary drivers of mechanical and thermal energy injection into the ISM, fundamentally shaping the dynamics of galactic centers. In the extreme environment of the CMZ and NSC, these events do not merely signal the end of stellar evolution but play a crucial role in regulating gas flows, star formation, and feedback near the SMBH.

1.2.1 Classification and Physical Mechanisms

The theoretical classification of SNe is based on both their spectroscopic features and the underlying physical process of the explosion (Branch and Wheeler, 2017).

- **Thermonuclear SNe (Type Ia):** These originate from explosive carbon ignition in a degenerate carbon-oxygen white dwarf that has reached the Chandrasekhar limit ($M \approx 1.4\,M_\odot$). The entire star is disrupted by a thermonuclear flame, producing significant amounts of ^{56}Ni.
- **Core-Collapse SNe (Types II, Ib/c):** These result from massive stars ($M \gtrsim 8-10\,M_\odot$). While stars at the lower end of this mass range may undergo electron-capture SNe (originating from degenerate magnesium or silicon cores), more massive progenitors develop a standard iron core. Once the core surpasses the stability limit, it collapses into a neutron star or black hole. The "bounce" of the outer layers against the collapsed core, mediated by neutrino heating, generates a supersonic shock wave that ejects the stellar mantle (Wheeler, 2017).

The fundamental differences in the explosion mechanisms and progenitors lead to distinct observational morphologies in SNRs. These differences are visually demonstrated in Figure 1.6, which compares a highly symmetric Type Ia shell (left panel) with the complex pulsar-driven structure of a core-collapse SNR (right panel). While the former is characterized by a nearly perfect spherical shock wave, the latter exhibits a chaotic environment powered by continuous energy injection from the central compact object.

Energetics and Initial Expansion

The canonical energy released in an SN event is $E_{\mathrm{SN}} \approx 10^{51}\,\mathrm{erg}$. While the total gravitational energy released in a core-collapse event is $\sim 10^{53}\,\mathrm{erg}$ (mostly in neutrinos), only approximately 1% is converted into the kinetic energy of the SN ejecta.

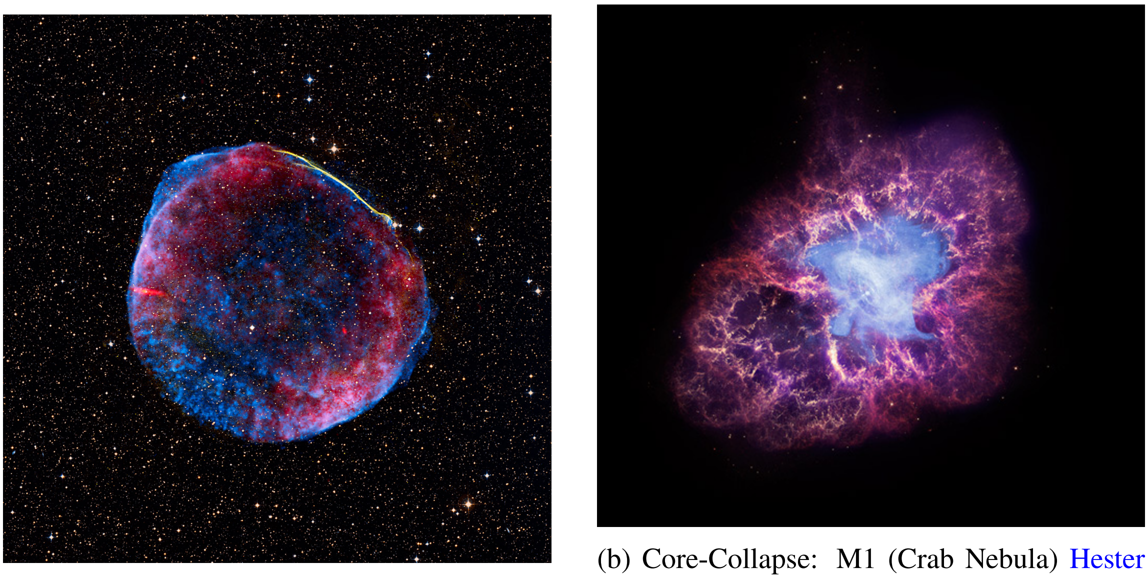

(a) Type Ia: SN 1006 ESO/NASA/ESA (2013)

(b) Core-Collapse: M1 (Crab Nebula) Hester (2008)

Figure 1.6: Comparison of SNR morphologies. The left image shows the characteristic spherical symmetry of a thermonuclear Type Ia explosion, while the right image illustrates the complex environment of a core-collapse remnant powered by a central pulsar.

In the initial free expansion phase, the ejecta mass M_{ej} is significantly larger than the swept-up mass of the ISM (M_{sw}). The expansion velocity v_{exp} remains nearly constant, and the radius R evolves linearly with time as

$$R(t) = v_{\mathrm{exp}}\, t = \sqrt{\frac{2E_{\mathrm{SN}}}{M_{\mathrm{ej}}}}\, t. \tag{1.25}$$

The Sedov–Taylor (Adiabatic) Phase

As the shock wave sweeps up more material, the SNR enters the Sedov–Taylor phase once $M_{\mathrm{sw}} \approx M_{\mathrm{ej}}$. During this stage, the total mechanical energy is conserved and the cooling of the gas is negligible. The evolution of the shock radius is governed by the self-similar solution derived for a point-source explosion in a medium with density ρ_0 (Binney and Tremaine, 2008),

$$R(t) = \xi \left(\frac{E_{\mathrm{SN}}}{\rho_0} \right)^{1/5} t^{2/5}, \tag{1.26}$$

where $\xi \approx 1.15$ for a monoatomic gas. The internal pressure p of the hot bubble scales as $p \propto R^{-3}$, driving the shock front outward. In the high-pressure environment of the galactic center, this phase is shorter than in the solar neighborhood due to the higher ambient density ρ_0.

Radiative Transition and the Radiative Phase

Once the temperature of the shocked gas drops below $\sim 10^6\,\mathrm{K}$, radiative cooling becomes the dominant energy loss mechanism. The cooling rate Λ is proportional to the square of the particle number density (n^2), meaning that in the dense nuclear disk ($n > 10^4\,\mathrm{cm}^{-3}$), the SNR transitions to the radiative phase (or "snowplow" phase) very rapidly.

In this stage, a thin and dense shell forms behind the shock front. The shell's expansion is no longer driven by total energy conservation, but by the conservation of momentum:

$$M(t)\,\boldsymbol{v}_{\mathrm{exp}}(t) = \mathrm{const.}, \tag{1.27}$$

where $M(t)$ represents the total mass of the expanding shell, which includes both the initial SN ejecta and the swept-up circumstellar material, and $\boldsymbol{v}_{\mathrm{exp}}(t)$ is its expansion velocity. This leads to a slower expansion rate, $R(t) \propto t^{1/4}$. In the galactic center, the intense tidal forces and high ambient pressure often cause the shell to fragment or dissipate before it can reach large radii, a process that is key to the local processing of molecular clouds (Morris and Serabyn, 1996).

Dynamical and Thermal Impact on Galactic Nuclear Regions

SNe are the dominant source of energy injection in the central regions of galaxies. Their impact is primarily two-fold: they provide mechanical support for the disk's structure and govern the thermal state of the molecular gas.

Mechanical Support and Turbulence: The central regions of galaxies possess deep gravitational potential wells (Binney and Tremaine, 2008). To maintain a finite vertical scale height H, the disk requires internal pressure to counteract the vertical component of gravitational acceleration g_z. While thermal pressure is present, it is often insufficient. SN explosions inject energy ($E_{\mathrm{SN}} \approx 10^{51}$ erg, typically) that drives macroscopic supersonic turbulent motions (Branch and Wheeler, 2017). This turbulent pressure acts as an additional supporting force, preventing the disk from collapsing into an infinitely thin layer and maintaining the observed dynamical equilibrium of the nuclear gas.

Thermal Discrepancy and Heating: In environments like the CMZ, there is a notable thermal discrepancy exists, where the gas temperature ($T_{\mathrm{gas}} \approx 30 - 200\,\mathrm{K}$) significantly exceeds the dust temperature ($T_{\mathrm{dust}} \approx 20\,\mathrm{K}$) (Morris and Serabyn, 1996). This decoupling indicates a heating mechanism that acts directly on the gas. The primary candidate is the dissipation of SNR-driven turbulence. As the kinetic energy from SN blast waves cascades to smaller scales, it is converted into thermal energy through viscous dissipation, effectively heating the molecular gas throughout the disk volume (Morris and Serabyn, 1996).

1.2.2 Physics of Supernova Remnants

SNRs are characterized by distinct morphologies tied to their progenitor type, as illustrated in Figure 1.6. Type Ia SNRs typically exhibit thin, symmetrical shells dominated by X-ray bremsstrahlung from swept-up ISM, reflecting a uniform ejecta distribution. Core-collapse SNRs, on the contrary, often display asymmetric composite structures with bright central regions powered by pulsars, producing a non-thermal synchrotron glow from ultra-relativistic electrons (Vink, 2012).

SNR shocks accelerate cosmic rays through diffusive shock acceleration, converting $\sim 10\%$ of kinetic energy into relativistic particles up to PeV energies. In dense CMZ ($n > 10^4\,\mathrm{cm}^{-3}$), these SNRs interact strongly with molecular clouds, boosting gamma-ray emission and fragmenting gas into turbulent clumps (Crocker et al., 2020).

This feedback from SNRs sustains supersonic turbulence in nuclear regions, providing mechanical support against gravity, heating molecular gas, and dispersing metals to regulate star formation near the SMBH. Together with SN explosions, SNRs thus dominate the dynamical and thermal evolution of galactic centers.

1.3 Mechanisms of Anisotropy in AGN Disks

The evolution of core-collapse SNe (CCSNe) within the gaseous environment of an AGN deviates significantly from standard vacuum or low-density ISM models. The presence of a geometrically thin, optically thick accretion disk introduces external forces and pressure gradients that break the spherical symmetry of the explosion and its preceding stellar wind. This anisotropy can strongly influence the observed light curves, spectra, and the final morphology of the SNR.

1.3.1 Progenitor Environment and Forced Symmetry Breaking

Massive stars such as red supergiants (RSGs), blue supergiants (BSGs), and Wolf–Rayet (WR) stars embedded in AGN disks are subject to intense environmental interactions before they explode.

Migration Acceleration (a_m)

Stars in AGN disks experience radial migration as a result of disk torques, similar to planetary migration. In a non-inertial frame centered on the migrating progenitor, this acceleration creates a preferred direction for gas expansion.

Ambient Pressure Gradients

The significant spatial extent of massive progenitors, particularly RSGs, which can reach radii up to $10^3\,R_\odot$, allows them to span regions of the disk characterized by substantial pressure gradients. The pressure difference between the side facing the SMBH ($p_{\mathrm{d,\,inner}}$) and the side facing the outer disk ($p_{\mathrm{d,\,outer}}$) acts as a non-uniform confining boundary.

Dominance of Acceleration

Analytical models, such as those presented by She et al. (2025), indicate that migration acceleration (a_m) exerts a more profound influence on environmental anisotropy than the local pressure gradients of the disk itself. This asymmetry is first established in the progenitor's stellar wind and is later imprinted onto the SN ejecta as it sweeps through the CSM.

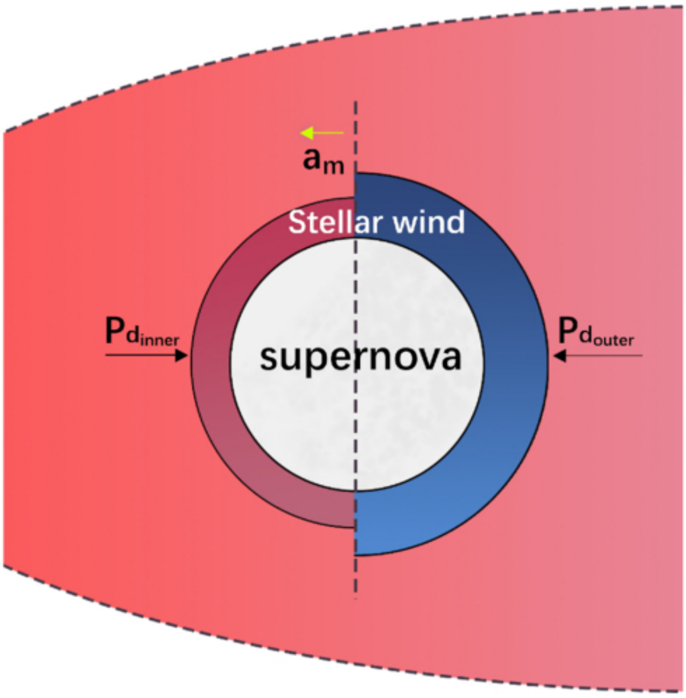

Figure 1.7: Schematic representation of an asymmetric stellar wind resulting from the combined effects of the radial pressure gradient within the AGN disk ($p_{\mathrm{d,\,inner}}$ and $p_{\mathrm{d,\,outer}}$) and the non-inertial acceleration of migration (a_{m}). Based on She et al. (2025).

1.3.2 Dynamics of Anisotropic Stellar Winds

Before the CCSN occurs, the progenitor's stellar wind carves out a cavity (or a ”wind-blown bubble”) within the disk. The extent of this cavity is defined by the balance radius r_{b}, which represents the point where the wind's momentum flux is equilibrated by the confining pressure of the disk. In the presence of migration acceleration and disk pressure gradients, this equilibrium must be calculated independently for the inner and outer regions (She et al., 2025):

$$-p_{\mathrm{f}} 4\pi r_{\mathrm{p}}^2 + p_{\mathrm{d,\,inner}} 4\pi r_{\mathrm{b,\,inner}}^2 + (-m a_{\mathrm{m}}) = 0, \tag{1.28}$$

$$p_{\mathrm{f}} 4\pi r_{\mathrm{p}}^2 - p_{\mathrm{d,\,outer}} 4\pi r_{\mathrm{b,\,outer}}^2 + (-m a_{\mathrm{m}}) = 0, \tag{1.29}$$

where p_{f} is the radiation pressure of the star, r_{p} is the progenitor radius, and m represents the coupled mass of the progenitor and its wind. Analytical results show that migration acceleration a_{m} is the more dominant factor in creating anisotropy compared to the disk pressure gradient. Consequently, the balance radius on the outer side ($r_{\mathrm{b,\,outer}}$) is consistently larger than that on the inner side ($r_{\mathrm{b,\,inner}}$), leading to an elongated circumstellar shell. The resulting geometry of the wind-blown bubble is shown in Figure 1.7. While the initial SN ejecta is considered isotropic (black circle), it expands into a pre-existing anisotropic environment. As a consequence of the different balance radii, the stellar wind forms an elliptical cavity (gray area). This shape is critical for the subsequent evolution, as the shock wave reaches the inner edge of the disk significantly earlier than the outer edge, leading to timing differences in energy dissipation.

Density Distribution Within the Wind Bubble

The spatial distribution of the stellar wind density ρ_{w} is a critical parameter for determining the momentum transfer during the subsequent SN explosion. Following the steady-state wind model (Vink, 2012; Li et al., 2023), the density profile of a spherically symmetric wind is typically expressed as:

$$\rho_{\mathrm{w}}(r) = \frac{\dot{M}}{4\pi r^2 v_{\mathrm{w}}}, \tag{1.30}$$

where $\dot{M}$ is the mass-loss rate and v_{w} is the terminal wind velocity. However, in the anisotropic environment of an AGN disk, the confining effect of external pressure p_{d} and migration acceleration a_{m} modifies the effective volume of the wind shell.

In the models presented by She et al. (2025), the density within the balance radius is often treated as a uniform or power-law distribution that terminates abruptly at r_{b}. The asymmetry in r_{b} implies that for a given mass-loss rate, the total swept-up mass M_{sw} by the shock differs between the inner and outer hemispheres:

$$M_{\mathrm{sw}}(\theta) = \int_{r_p}^{r_b(\theta)} \rho_{\mathrm{w}}(r,\theta)\, 4\pi r^2 dr. \tag{1.31}$$

Because $r_{\mathrm{b,\,outer}} > r_{\mathrm{b,\,inner}}$, the shock wave on the outer side interacts with a more extended (and potentially more dilute) medium, which delays the shock's emergence from the wind shell compared to the inner side. This discrepancy in mass loading is the fundamental reason for the bifurcated nature of the resulting light curves.

Equation of Motion for the Anisotropic Shock

To unify these effects, the expansion of the shock front r_{sh} can be described by the momentum conservation equation, accounting for the swept-up mass from both the anisotropic wind and the surrounding disk material (Kurfürst et al., 2020; She et al., 2025):

$$\frac{d}{dt}(M_{\mathrm{sh}} v_{\mathrm{sh}}) = 4\pi r_{\mathrm{sh}}^2 (p_{\mathrm{sh}} - p_{\mathrm{d}}) \pm \rho_{\mathrm{w}} a_{\mathrm{m}} \Delta V \tag{1.32}$$

where M_{sh} is the total shocked mass, v_{sh} is the shock velocity, and p_{sh} is the internal pressure behind the shock front. The ambient disk pressure p_{d} is direction-dependent and corresponds to either $p_{\mathrm{d,\,inner}}$ or $p_{\mathrm{d,\,outer}}$, depending on whether the shock is propagating towards the central SMBH or away from it. The term $\rho_{\mathrm{w}} a_{\mathrm{m}} \Delta V$ represents the additional inertial force contribution due to the migration of the progenitor. Here, ΔV denotes the volume of the expanding thin shell of swept-up material ($\Delta V \approx 4\pi r_{\mathrm{sh}}^2 \Delta r$, where Δr is the radial thickness of the shell). Consequently, the product $\rho_{\mathrm{w}} \Delta V$ corresponds to the local mass of the wind experiencing the effective migration acceleration a_{m}, which further drives the expansion asynchrony between the inner and outer hemispheres.

Observable Signatures of Anisotropic Interaction

The geometric asymmetry of the CSM leads to measurable variations in SN emission, as the kinetic energy of the ejecta is converted into radiation at different rates across the SNR. The most significant effects identified in recent models She et al. (2025); Kurfürst et al. (2020) include:

- **Luminosity Discrepancy:** The total shock luminosity depends on the density of the ambient medium and the shock velocity. On the inner side of the disk, the higher gas pressure and density can lead to more rapid energy dissipation, while on the outer side, the peak luminosity may be lower due to the extended balance radius. Analytical estimates suggest that the resulting bolometric luminosity can differ by up to 50% between the two hemispheres (She et al., 2025).

- **Light Curve Duration:** The duration of the shock-powered emission is governed by the time required for the shocks to sweep through the circumstellar material. Because $r_{\mathrm{b,outer}} > r_{\mathrm{b,inner}}$, the interaction timescale in the outer hemisphere is extended, resulting in a broader light curve compared to the inner hemisphere.

- **Spectral Line Profiles:** The non-spherical expansion velocity field and the asymmetric distribution of the shocked material lead to distorted spectral line profiles. These often manifest as shifted peaks or double-peaked structures, depending on the viewing angle of the observer relative to the disk plane. Such spectral features, combined with continuum polarization, provide a diagnostic tool for the orientation of the progenitor within the AGN environment (Kurfürst et al., 2020).

These signatures demonstrate that the observed light curve of an SN in an AGN disk is the integrated signal of two physically distinct interaction regions.

1.3.3 Progenitor on an Elliptical Orbit

The assumption of circular orbits for massive progenitors within the CMZ or an AGN disk represents a simplified scenario. In reality, stars within the NSC frequently follow highly eccentric Keplerian orbits around the SMBH (Genzel et al., 2010). The ellipticity of the orbit introduces a fundamental temporal and spatial variation into the pre-SN environment and the subsequent shock wave evolution. The interaction dynamics become strictly dependent on the exact orbital phase at which the core-collapse occurs, creating two extreme physical regimes: the pericenter and the apocenter.

Orbital Kinematics and the Vis-viva Equation

The geometry of an elliptical orbit is defined by its semi-major axis a and eccentricity e. The distance of the progenitor from the central singularity r varies between the pericenter (the closest approach) r_{p} and the apocenter (the farthest point) r_{a}:

$$r_{\mathrm{p}} = a(1-e), \quad r_{\mathrm{a}} = a(1+e). \tag{1.33}$$

The instantaneous orbital velocity $v_{\rm orb}$ of the star at any radial distance r is governed by the conservation of a specific orbital energy, expressed through the Vis-viva equation (Binney and Tremaine, 2008):

$$v_{\rm orb}^2 = GM_\bullet \left(\frac{2}{r} - \frac{1}{a} \right). \tag{1.34}$$

Consequently, the progenitor reaches its maximum velocity at the pericenter and its minimum velocity at the apocenter. For highly eccentric orbits ($e \gtrsim 0.5$), the velocity discrepancy between the two points is substantial, fundamentally altering the kinematic interaction between the star and the surrounding gaseous disk.

Ambient Density and Ram Pressure

The nuclear gas disk is not uniform; its density profile $\rho_{\rm disk}(r)$ typically exhibits a steep radial decline from the center (F02). A star plunging toward the pericenter thus penetrates increasingly dense and pressurized regions of the accretion flow.

As the progenitor moves through this medium, its stellar wind and the subsequent SN ejecta are subjected to an intense ram pressure $p_{\rm ram}$, defined as the momentum flux of the oncoming ambient gas in the rest frame of the star (Kurfürst et al., 2020; She et al., 2025):

$$p_{\rm ram} \approx \rho_{\rm disk}(r)\, v_{\rm orb}^2(r). \tag{1.35}$$

Ram pressure is the primary driver of environmental anisotropy. In the pericenter, the combination of the maximum ambient density $\rho_{\rm disk}(r_{\rm p})$ and the squared maximum orbital velocity $v_{\rm orb}^2(r_{\rm p})$ results in an extreme peak of $p_{\rm ram}$. This massive external pressure severely restricts the expansion of the pre-SN stellar wind, compressing the balance radius $r_{\rm b}$ (as defined in Equations 1.28 and 1.29) and greatly distorting the wind-blown cavity in the direction of the orbital motion. In contrast, at the apocenter, both the velocity and the ambient density reach their minima, producing a significantly lower $p_{\rm ram}$ and allowing the formation of a more extended quasi-spherical CSM.

Hydrodynamic Consequences for the SNR

The extreme contrast between the pericenter and apocenter environments dictates the entire thermodynamics and morphological evolution of the SNR.

- **Pericenter Explosions:** When the explosion occurs at or near the pericenter, the shock wave immediately impacts a deeply dense and dynamically aggressive medium. The swept-up mass $M_{\rm sw}$ accumulates extremely fast, causing an abrupt deceleration of the ejecta. Crucially, the radiative cooling timescale $t_{\rm cool}$, which scales inversely with the ambient density ($t_{\rm cool} \propto n^{-1}$, see Equation 1.9), is severely shortened (Draine, 2011). The SNR experiences a rapid termination of the adiabatic Sedov–Taylor phase, transitioning almost instantaneously into the momentum-conserving radiative phase (Branch and Wheeler, 2017). The resulting morphology is highly compressed, anisotropic, and subject to rapid thermal dissipation.

- **Apocenter Explosions:** An explosion at the apocenter expands into a more dilute environment with a substantially lower relative velocity of the surrounding gas. The rate of mass accumulation $M_{\rm sw}$ is slower, and the radiative cooling efficiency is reduced. Consequently, the shock wave remains in the energy-conserving adiabatic phase for a significantly longer duration. The blast wave retains a more spherical symmetry and expands to a larger physical volume before the ambient pressure stops its propagation.

By modeling these two disparate orbital extremes, one can quantify the full spectrum of environmental feedback mechanisms, from rapid radiative quenching deep in the gravitational well to prolonged adiabatic expansion at the periphery of the nuclear disk.

Chapter 2

Numerical Modeling

2.1 Hydrodynamic Code *Castro*

The numerical modeling of SNRs within a nuclear gas disk requires a computational framework capable of resolving high-energy shocks and extreme density gradients across multiple scales. Simulations are conducted using *Castro* (Almgren et al., 2010), a compressible adaptive-mesh hydrodynamic code specifically designed for high-energy astrophysical flows. *Castro* solves the multicomponent compressible Euler equations, which describe the conservation of mass, momentum, and total energy in a fluid system (the underlying mathematical framework and its derivation in cylindrical coordinates are detailed in the Appendix A). Spatial discretization in the code relies on a higher-order Godunov method, specifically the unsplit Piecewise Parabolic Method (PPM) (Colella and Woodward, 1984).

Piecewise Parabolic Method

To achieve high-order spatial accuracy, *Castro* utilizes the PPM for the reconstruction of states at cell interfaces. This method is essential to capture the sharp discontinuities and high-pressure gradients associated with SN-induced shock waves (Miller and Colella, 2002). The azimuthal momentum transport within the disk is handled by integrating the full second-order Navier-Stokes viscosity term $f_{\mathrm{visc}}^{(2)}$ in Equation (1.18), which prevents physically implausible backward rotational motion in the outer regions (Kurfürst et al., 2018). By reconstructing state variables at cell interfaces using parabolic interpolation, the Riemann solver achieves high fidelity, ensuring accurate flux calculations even in the presence of supersonic ejecta.

Riemann Solver

The heart of the hydrodynamic update in *Castro* is the Riemann solver, which is responsible for calculating the numerical fluxes of mass, momentum, and energy across all interfaces. Once the PPM reconstruction provides the left and right states at each interface, the Riemann solver resolves the resulting nonlinear evolution of the fluid, effectively modeling the propagation of shocks, contact discontinuities, and rarefaction waves (Toro et al., 1994).

In the context of highly supersonic ejecta, *Castro* typically utilizes an approximate Riemann solver, such as the HLLC (Harten-Lax-van Leer-Contact) solver. This specific solver is favored for its robustness and ability to accurately capture contact discontinuities, which are essential for resolving the interface between the hot SN bubble and the ambient molecular gas. By solving the Riemann problem at each cell face, the code ensures that the global conservation laws for the Euler equations are strictly satisfied, preventing the accumulation of numerical errors even in the presence of extreme Mach numbers.

2.1.1 Adaptive Mesh Refinement

Castro utilizes block-structured Adaptive Mesh Refinement (AMR) to deliver the dynamic spatial resolution required for accurately simulating SNRs in the complex, multi-scale environment of galactic centers. This approach, based on the AMReX framework (Zhang et al., 2019), divides the computational domain into fixed size adaptive rectangular blocks (typically 8^3 or 16^3 cells), arranged in a hierarchical tree structure. Starting from a coarse base level, the code identifies regions requiring higher precision, such as the high-velocity shock front of an SN or areas with steep density gradients within the nuclear disk, and dynamically overlays finer grid levels. Each level of refinement is characterized by a refinement ratio, typically 2 or 4, which increases the local resolution by decreasing the cell width Δx. This ensures that the intricate interaction between the blast wave and the dense filaments of the ISM is resolved at the sub-parsec scale without the prohibitive computational cost of a globally uniform high-resolution grid. The efficiency of this hierarchical structure is further enhanced by temporal sub-cycling, a process in which each AMR level evolves with its own time step (Almgren et al., 1998). This temporal flexibility is fundamentally dictated by the numerical stability of the system, which is governed by the CFL condition.

CFL Number

The numerical stability and consistency of the time-integration scheme are governed by the Courant-Friedrichs-Lewy (CFL) condition (Courant et al., 1928). The CFL condition ensures that the time step Δt is small enough so that physical information propagating by fluid velocity or sound waves does not travel across more than one grid cell in a single step. The time step is dynamically calculated as

$$\Delta t \leq \mathrm{CFL} \cdot \min\left(\frac{\Delta x}{|v| + a}\right), \tag{2.1}$$

where the CFL number is typically ≤ 0.9, Δx is the cell size, v is the fluid velocity, and a represents the speed of sound. In the context of an SN explosion, where velocities can reach $10^4\,\mathrm{km\,s^{-1}}$, the CFL condition significantly reduces the time step during the initial expansion phase to resolve the propagation of the high-velocity shock.

2.2 Simulation Setup

This section describes the practical implementation of the physical models within the *Castro* framework. The setup is designed to capture the high-speed expansion of the ejecta into a stratified rotating medium, requiring a balance between high-resolution localized features and a large-scale computational volume. By utilizing dynamic grid techniques and conservative stability limits, the simulation ensures the numerical accuracy of the shock propagation across the nuclear disk.

2.2.1 Computational Domain and Dynamic Scaling

The simulation is performed on a 2D Cartesian grid centered at the origin. To optimize computational efficiency without sacrificing the physical integrity of the long-term expansion, we employ a dynamic domain expansion technique known as *Embiggening*.

The simulation begins within a restricted coordinate range to focus computational resources on the progenitor star. As the high-velocity blast wave approaches the grid edges, the domain is expanded by appending cells to the boundaries. This expansion is triggered by a pressure-based threshold, which ensures that the outflow boundaries remain at a sufficient distance from the shock front to prevent numerical interference.

The spatial resolution is defined by the cell size Δx, which is determined by the total domain width L and the number of cells N_x:

$$\Delta x = \frac{x_{\mathrm{hi}} - x_{\mathrm{lo}}}{N_x}, \tag{2.2}$$

where x_{hi} and x_{lo} represent the domain boundaries.

2.2.2 Reconstruction and Numerical Stability

The spatial resolution is dynamically enhanced using block-structured AMR. Following the criteria defined in the previous chapters, the refinement is triggered by steep pressure gradients and relative pressure errors, ensuring that the highest resolution is always localized at the shock front.

To resolve the extreme Mach numbers associated with the SN ejecta, we utilize the PPM for higher-order spatial reconstruction. Numerical stability is strictly maintained through the CFL condition, using a conservative safety factor of 0.6. This is critical for preventing oscillations in the high-energy flow, where fluid velocities are capped at a significant fraction of the speed of light to maintain physical consistency within the relativistic limit.

2.2.3 Boundary Interaction and Radiation

The boundaries of the computational domain are configured to simulate an open galactic environment. For the hydrodynamic variables, we employ outflow boundary conditions, which utilize zero-gradient extrapolation to allow the blast wave and gas to leave the domain without non-physical reflections.

For the radiation transport, Neumann boundary conditions (defined by the first derivatives of the particular physical quantities) are implemented with a zero inward flux value. This ensures that the thermal luminosity generated by the SN event can exit the system freely, effectively modeling the radiative losses into the larger ISM.

2.2.4 Initial Conditions

Accurate initialization of the fluid state at $t = 0$ is critical to capture the subsequent interaction between the SN ejecta and the surrounding medium. The computational domain is functionally divided into two distinct regions: the interior of the SN progenitor and the complex external environment, comprising the CSM and the dense nuclear disk.

Supernova Progenitor

The SN progenitor is modeled as a spherical structure with an initial radius $R_{\rm star}$. Inside this region ($r \leq R_{\rm star}$), the fluid state is not analytically prescribed but is instead read and mapped from a one-dimensional, pre-computed stellar evolution profile. The density (ρ), temperature (T) and radial velocity (v_r) of the ejecta are interpolated from the input data onto the computational grid. The Cartesian velocity components v_x and v_y are then determined using geometric projection:

$$v_x = v_r \sin\theta, \quad v_y = v_r \cos\theta, \tag{2.3}$$

where θ is the polar angle relative to the center of the progenitor.

Ambient Medium and Nuclear Disk

Outside the progenitor ($r > R_{\rm star}$), the background medium is initialized as a superposition of three components: a stellar wind, a spherically symmetric CSM, and a rotationally supported nuclear disk (Kurfürst, 2017).

The density of the central disk, $\rho_{\rm disk}$, is initialized to approximate a vertical hydrostatic structure modulated by the radial distance from the supermassive black hole (SMBH). The exact formulation incorporates the characteristic disk temperature $T_{\rm disk}$ and the corresponding sound speed a:

$$\rho_{\rm disk}(x, y) = \rho_{0,\rm disk} \exp\left(-\frac{GM_\bullet (y-q)^2}{2a^2|x+p+\epsilon|^3}\right), \tag{2.4}$$

where $M_\bullet$ is the mass of the central SMBH. Note that the standard cylindrical coordinates (r, z) are replaced here by (x, y), where y represents the vertical distance from the midplane and x corresponds to the radial distance. This renaming convention is dictated by the specific coordinate implementation requirements of the numerical code. The constants p, q, and ϵ are coordinate offsets introduced to intentionally displace the geometric center of the disk from the center of the computational domain. This displacement is a technical requirement necessitated by the domain expansion technique (*Embiggening*), which dynamically adds grid cells to track the fastest-moving ejecta, forcing the initial setup to be strategically off-centered to optimize computational resources.

The density of the disk midplane $\rho_{0,\rm disk}$ is not an arbitrary constant but is strictly coupled to the radial distance and the established accretion profile. To maintain physical consistency with a thin Keplerian disk model (F02), the midplane density is calculated analytically within the initialization routine as:

$$\rho_{0,\mathrm{disk}}(x) = \frac{\Sigma_0 R_\bullet^2 \sqrt{GM_\bullet}}{\sqrt{2\pi} a |x + p + \epsilon|^{7/2}}. \tag{2.5}$$

In this expression, Σ_0 represents the reference surface density at the inner boundary, and $R_\bullet$ is the gravitational radius of the SMBH. The power-law dependence of $|x+p+\epsilon|^{-7/2}$ in the denominator is a direct consequence of combining the geometrically determined scale height $H = a/\Omega \propto R^{3/2}$ with an assumed radial surface density profile $\Sigma(R) \propto R^{-2}$, which is characteristic of the modeled accretion flows (Kurfürst et al., 2014). This dynamic computation ensures that the nuclear gas disk maintains proper hydrostatic and rotational equilibrium across the entire simulated domain prior to the SN shock wave injection.

The total ambient density ρ is then calculated as the sum of the disk, wind, and CSM densities:

$$\rho = \rho_{\mathrm{disk}} + \rho_{\mathrm{wind}} + \rho_{\mathrm{CSM}}. \tag{2.6}$$

Although the latter equation may not be regarded as a physically correct summing relationship, given the many orders-of-magnitude differences in the densities of the disk and the wind—and consequently between the wind and the surrounding medium—in key regions near the SN progenitor, this simplified approach is commonly used in similar configurations.

Equation of State Closure

Once the macroscopic fluid variables (ρ, T, and $\boldsymbol{v}$) are assigned to each cell, the internal energy density e and the total energy density E are computed using the integrated equation of state (EoS) module. Following the assumption of a multi-species calorically perfect gas described in Section A.5, the EoS routine derives the internal energy based on the local temperature and specified mass fractions, completing the thermodynamic initialization of the state vector prior to the first hydrodynamic time step.

2.3 Physical Modules and Equations

Building upon the mathematical foundations established in the Appendix A, this section details how the conservation laws and the Cauchy stress tensor are translated into the numerical environment. While the theoretical framework accounts for the full Navier-Stokes equations, the *Castro* code is primarily configured to solve the compressible Euler equations with the additional source terms for gravitation and radiation.

2.3.1 Hydrodynamics and Momentum Transport

The core of the simulation is the integration of the conservation of mass Equation (A.26) and momentum Equation (A.30). In our setup, the code solves the non-viscous limit of the Navier-Stokes equations, focusing on the high-Mach number regime of the SNR where numerical dissipation typically dominates over physical viscosity.

The momentum (A.30) is solved in its conservation form to ensure the accurate capture of shocks. The velocity field $\boldsymbol{v}$, as derived in cylindrical coordinates in Equation (A.9), is mapped to the 2D Cartesian grid, with the azimuthal component v_ϕ providing rotational support for the nuclear disk. To ensure stability, the fluid velocities are capped by the numerical speed limit, preventing non-physical artifacts near the SMBH.

2.3.2 Gravitation and Central Potential

As established in Section A.6, the gravitational field in our model is governed by the superposition of the central SMBH and the self-gravitation of the surrounding gas. In the *Castro* code, these two components are evaluated using distinct numerical approaches, and their resulting accelerations are added as explicit source terms to the momentum and energy conservation equations at each time step.

Gas Self-Gravitation

To determine the gravitational potential of the continuous fluid Φ_{gas}, *Castro* solves Poisson's Equation (A.58) (Almgren et al., 2010). Because the simulation domain represents an isolated astrophysical system, standard periodic boundary conditions are not applicable. Instead, the code employs a multipole expansion method to compute the isolated Dirichlet boundary conditions at the edges of the computational grid. In our setup, the multipole expansion is evaluated up to the order of $l_{\text{max}} = 6$. This provides a highly accurate and computationally efficient approximation of the global gravitational field generated by the complex density distribution of the perturbed disk and the expanding SN shell.

Point Mass Potential

The SMBH is treated as a discrete point mass $M_\bullet$, which generates the potential described by Equation (A.59). While the theoretical framework allows for an arbitrary position vector of the singularity, the specific implementation of the multipole expansion for self-gravitation in *Castro* requires the point mass to be located exactly at the origin of the coordinate system. The total gravitational acceleration $\boldsymbol{g}$ is then calculated as the negative gradient of the combined potential and is coupled directly to the hydrodynamic Riemann solver.

2.3.3 Radiation and Energy Balance

The conservation of total energy (A.47) is modified to include the effects of radiative cooling and transport, which are critical in the dense environment of the galactic center. The heat flux term $\mathbf{q}$ from the mathematical derivation is implemented via the Flux-Limited Diffusion (FLD) module.

This module couples the gas temperature T to the radiation field through frequency-averaged opacities. The energy balance is further governed by the Planck and Rosseland mean opacities, which determine the efficiency of energy exchange between the SN ejecta and the ISM.

2.3.4 Caloric Equation of State

The closure of the system (A.55) is provided by the gamma-law EoS. In the input configuration, the adiabatic index is set to $\gamma = 5/3$, representing a monatomic ideal gas. This is consistent with the adiabatic expansion phase of the SNR described in Chapter 1. Equation (A.55) allows the code to derive the gas pressure p and temperature T from the conserved total energy E and mass density ρ at each time step.

Chapter 3

Numerical Simulations of SN Explosions

3.1 The Galactic Center Case: Midplane and Offset Explosions

This section examines the initial simulation cases in which the SN progenitor is located at a distance of 1.8×10^{15} cm (approximately 120 AU) from the SMBH with a mass of $4 \times 10^6 \, M_\odot$. This mass scale was specifically chosen to remain consistent with that of Sagittarius A*, the SMBH at the Galactic Center, thus providing a direct astrophysical baseline for our models. These simulations focus on how the placement of the explosion relative to the disk midplane affects the resulting shock wave morphology in such a galactic environment. The general geometric configuration and the spatial relationship between the SMBH and the SN progenitor are illustrated in Figure 3.1.

3.1.1 Case A: Explosion Within the Disk Midplane

In this scenario, the SN propagation is situated directly in the dense midplane of the accretion disk ($z = 0$ AU). The evolution is characterized by the interaction with the vertical density gradient of the disk, which significantly shapes the resulting remnant.

Morphological Evolution

At the early stage, the shock wave maintains a relatively spherical symmetry. However, as the expansion progresses, the remnant develops a distinct bi-lobed shape. This is caused by the shock front expanding rapidly into the lower-density regions above and below the disk while being decelerated by the high ram pressure within the disk plane.

Physical Quantities

The temperature maps reveal high-energy zones ($T \approx 10^8 - 10^9$ K) in the shock front. The pressure distribution shows intense heating at the contact discontinuity where the SN material impacts the disk.

Numerical Boundary Interaction

In the final frame, a visible distortion appears at the left boundary of the domain. This artifact is caused by the lack of orbital equilibrium at the boundary. Although the accretion disk is modeled with a specific rotational velocity, the current version of the code does not allow for a point-mass gravitational source to be defined outside the active computational domain. Without this central gravitational pull to balance the centrifugal force, the rotating disk material near the boundary lacks stability, leading to numerical artifacts where the SN shock meets the edge of the grid.

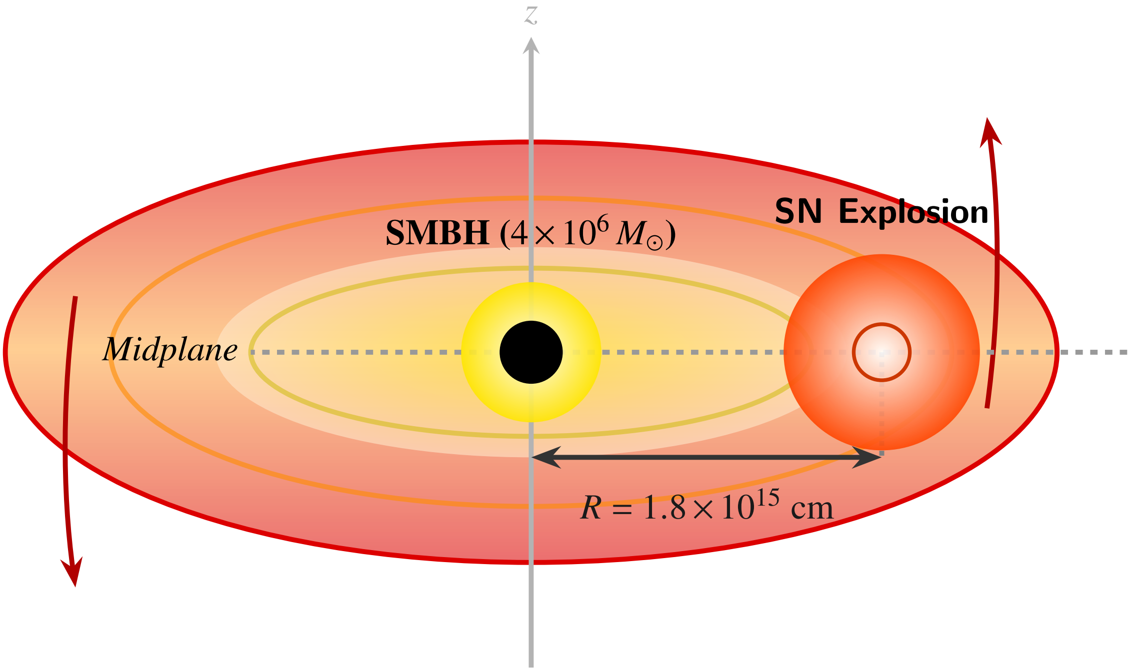

Figure 3.1: Geometric setup for the explosion within the disk midplane model. The SN is positioned in the midplane at a radial distance $R = 1.8 \times 10^{15}$ cm from the central $4 \times 10^6\, M_\odot$ SMBH.

3.1.2 Case B: Explosion Offset Below the Disk Plane

This model explores the impact of broken symmetry, where the progenitor is located at a vertical offset below the midplane of the disk ($z = -4.5 \times 10^{14}$ cm). This configuration leads to a highly non-uniform expansion of the SNR. The geometric setup for this case is illustrated in Figure 3.2.

Morphological Evolution

From the onset, the SNR expands faster into the diluted halo below the disk. After that, the remnant exhibits a pronounced asymmetry; the upper hemisphere is significantly ”flattened” as it collides with the dense midplane, whereas the lower hemisphere continues to expand more freely.

Physical Quantities

The speed maps at late stages show that the lower part of the SNR reaches higher radial velocities than the part that interacts with the disk. The density maps clearly illustrate the compression of the disk material as the shock wave sweeps through the midplane.

Numerical Boundary Interaction

Similarly to Case A, the interaction at the left boundary ($R \approx -200\,\mathrm{AU}$) is evident in the late-stage plots. The visible "impact" is not purely an interaction with the SMBH itself but rather a numerical consequence of the imbalance between centrifugal and gravitational forces. Because the stabilizing point-mass gravity cannot be placed outside the domain to counteract the rotation of the disk material, the boundary cannot maintain the physical equilibrium of the rotating fluid, resulting in the distortion of the expanding shock wave at the domain edge.

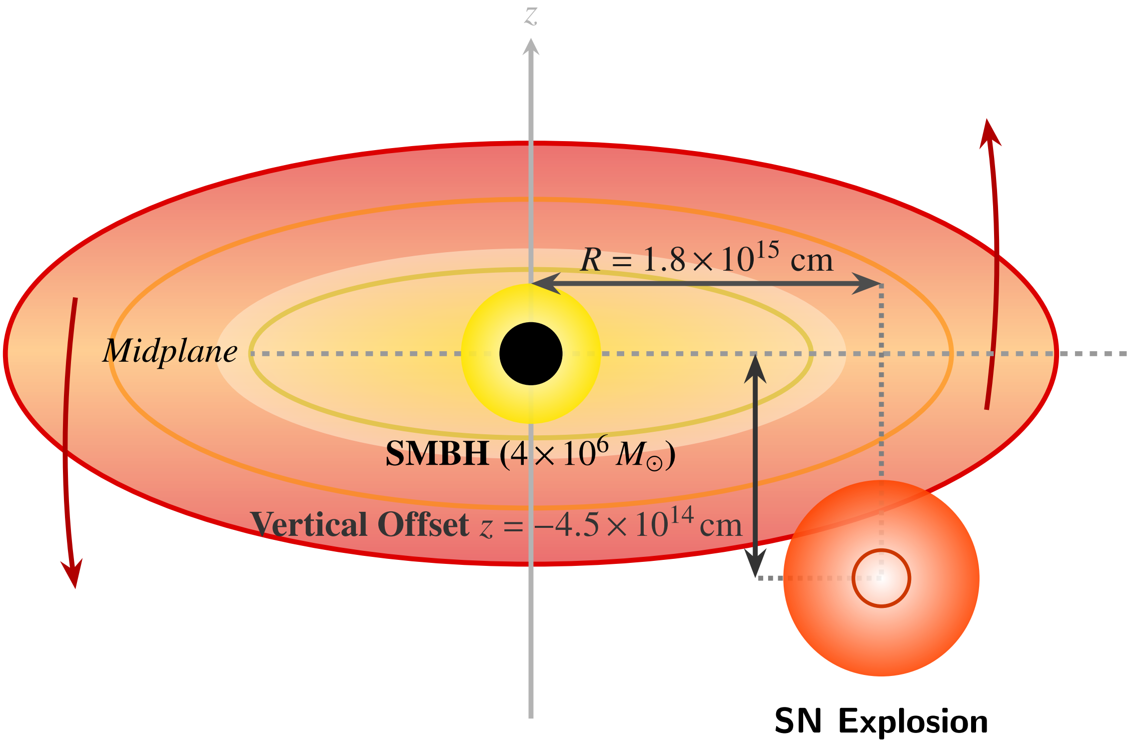

Figure 3.2: Initial configuration for the explosion offset below the disk plane model. The SN is vertically displaced at $z = -4.5 \times 10^{14}$ cm with a radial distance $R = 1.8 \times 10^{15}$ cm from the central $4 \times 10^6\, M_\odot$ SMBH.

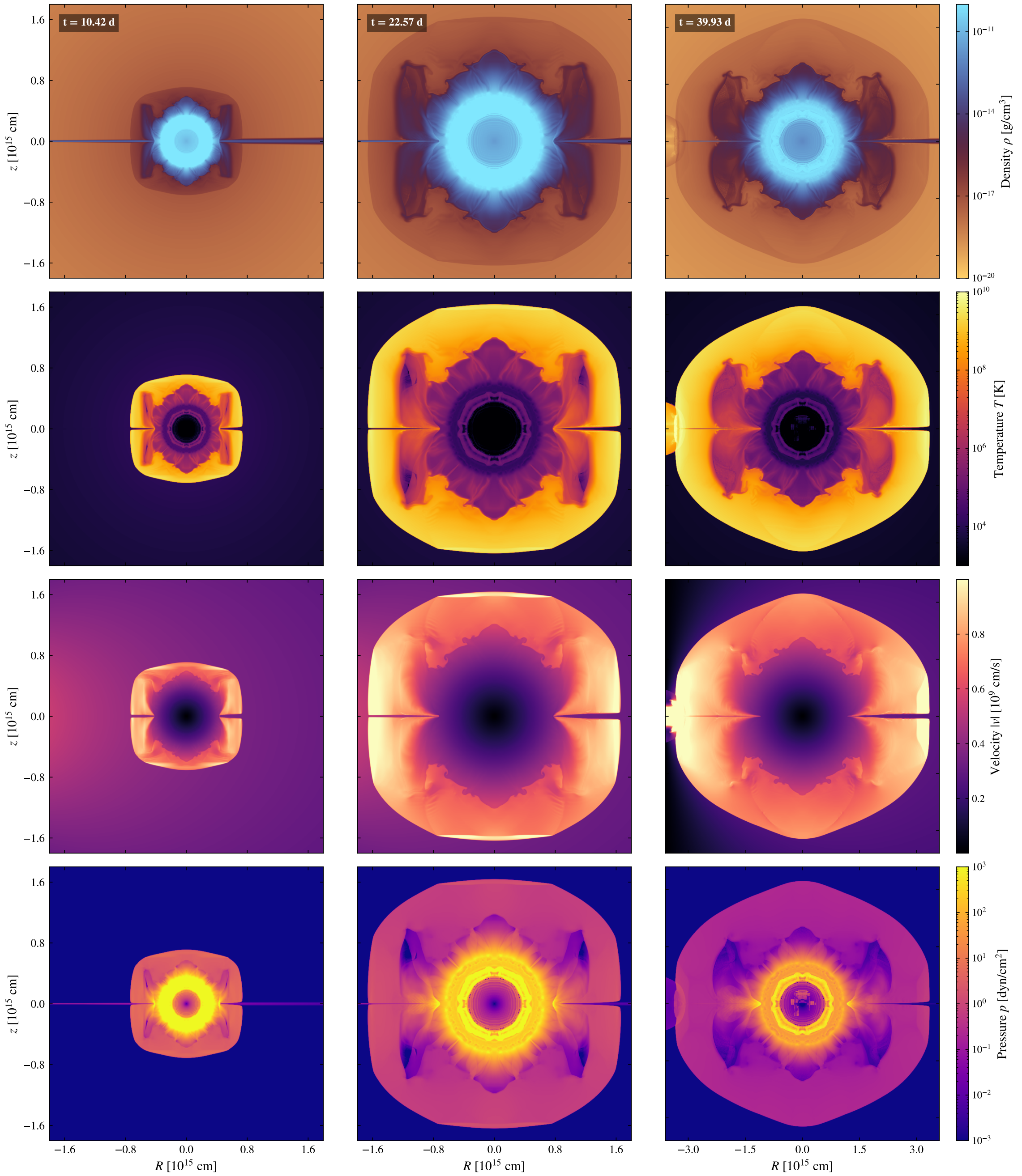

Figure 3.3: Evolution of an SNR exploding in the disk midplane ($z = 0\,\mathrm{AU}$) near a $4 \times 10^6\,M_\odot$ SMBH. Rows show ρ, T, $|v|$, and p; columns show snapshots at $t = 10.42, 22.57, 39.93$ days.

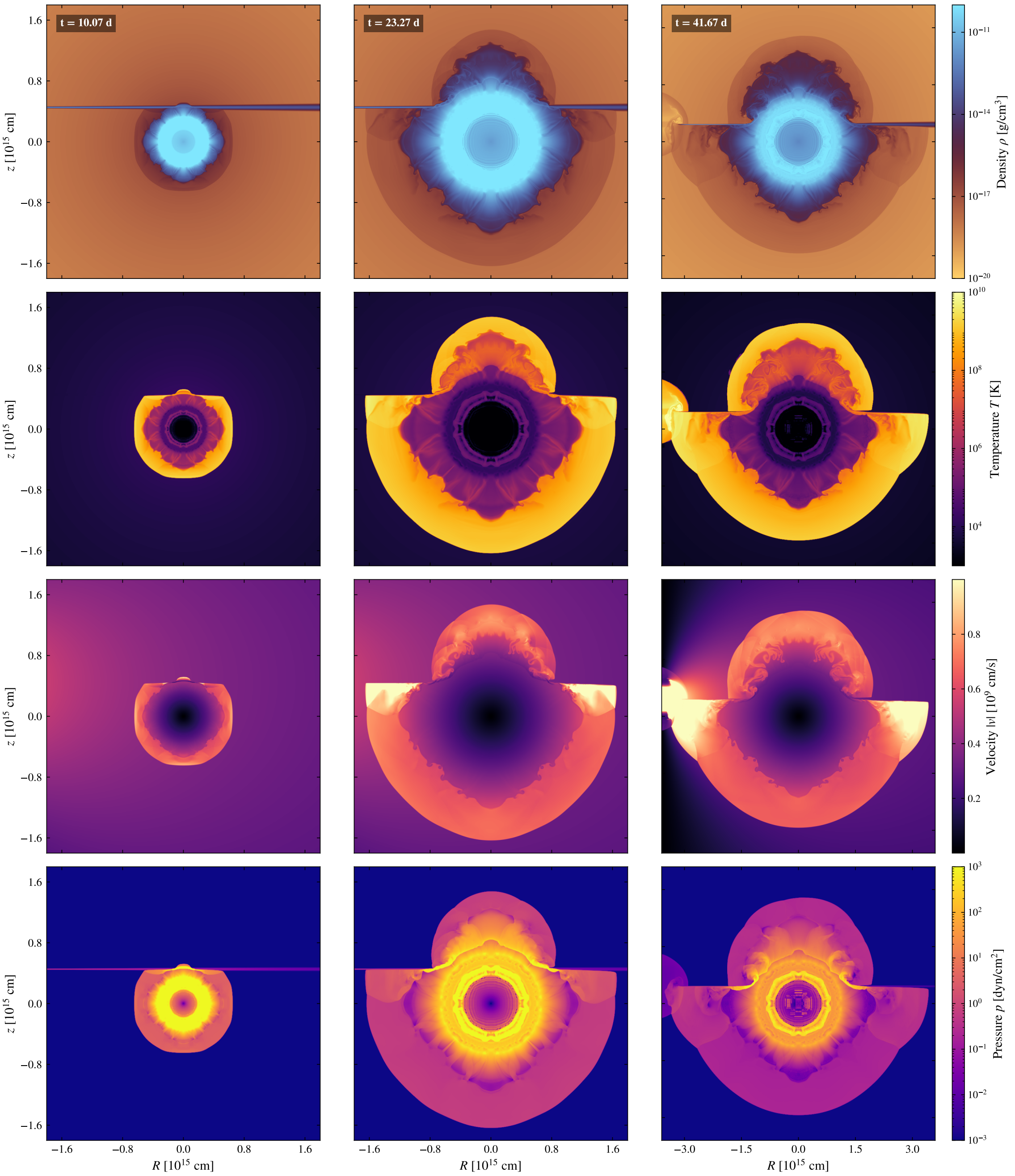

Figure 3.4: Evolution of an SNR offset below the disk midplane ($z = -4.5 \times 10^{14}$ cm). Rows show ρ, T, $|v|$, and p; columns show snapshots at $t = 10.07, 23.27, 41.67$ days.

3.2 Analysis of Stationary SNRs at Varying Radial Distances

In these scenarios, the SN progenitor is considered to be ”stationary” relative to the disk material at the moment of the explosion. This baseline is essential for understanding how the background density gradient and the SMBH mass scale influence the morphology of the shock waves independently of orbital shear. The multiscale nature of this setup, bridging the global AGN environment and the local 2D computational domain, is schematically depicted in Figure 3.5. The parameters of these models are defined by the radial distance (R) in terms of gravitational radii ($R_{\rm g}$), where $R_{\rm g} = GM_\bullet/c^2$, and the mass of SMBH ($M_\bullet$).

3.2.1 Influence of Radial Distance ($10^3\,R_{\rm g}$ to $10^5\,R_{\rm g}$)

The distance from the SMBH plays a critical role in the symmetry of the expansion.

Case $10^3\,R_{\rm g}$ (Strong Interaction)

At the closest simulated distance ($10^3\,R_{\rm g}$), the SNR is significantly constrained by the dense midplane of the accretion disk. The remnant exhibits a highly ”pinched” morphology, where expansion is funneled toward the vertical z-axis. For the $10^8\,M_\odot$ case, the expansion reaches approximately 200 AU in 30.91 days.

Case $10^4\,R_{\rm g}$ (Intermediate Interaction)

At $10^4\,R_{\rm g}$, the density gradient is still pronounced, but the SNR begins to occupy a larger volume before gaining significant resistance from the disk. In the $10^9\,M_\odot$ model, the SNR remains relatively contained within the disk for more than 138 days, maintaining a distinct bipolar shape.

Case $10^5\,R_{\rm g}$ (Weak Interaction/Spherical Expansion)

At the farthest distance of $10^5\,R_{\rm g}$, the influence of the density stratification of the disk is the weakest. The remnant appears much more isotropic and spherical compared to the $10^3\,R_{\rm g}$ cases. The expansion velocity is also lower, with maximum values around 5×10^8 cm/s compared to over 1×10^9 cm/s in models that are closer.

3.2.2 Influence of SMBH Mass (10^8 vs. $10^9\,M_\odot$)

The mass of the SMBH determines the physical scale of the gravitational radius ($R_{\rm g}$), which in turn affects the physical dimensions of the interaction zone.

Mass $10^8\,M_\odot$

These models evolve on shorter physical timescales. For example, at $10^4\,R_{\rm g}$, the simulation captures the evolution of the SNR up to 67.02 days. The velocity maps show a maximum magnitude of approximately 1.0×10^9 cm/s.

Mass $10^9\,M_\odot$

Due to the larger physical distances associated with R_g for a more massive black hole, these models involve larger spatial domains, reaching up to ±400 AU. The physical time captured is also longer, extending up to 138.42 days for the $10^4\,R_g$ case. The density maps show a more massive and vertically extended disk structure that interacts with the shock.

3.2.3 Summary of Physical Quantities

Density

The SNRs expand from a central high-density core to a stratified medium, with ambient disk densities ranging from 10^{-14} to 10^{-20} g/cm^3.

Temperature

The maximum temperatures on the shock front remain between 10^8 and 10^9 K in most models, with a rapid drop to $10^3 - 10^4$ K in the expanding interior. Additionally, the purely adiabatic solutions were post-processed semi-analytically using the radiative cooling prescriptions detailed in 3.5.4 to provide a more realistic estimate of the thermal evolution.

Pressure

Intense pressure peaks (up to 10^2 dyn/cm^2) are located on the interface front between the SNR and the disk midplane.

Note on Model Selection

It should be noted that the $10^5\,R_g$ case for $10^9\,M_\odot$ SMBH was intentionally omitted from this comparative study. Preliminary results indicated that at such large radial distances, the differences in the morphological evolution of the SNR between the $10^8\,M_\odot$ and $10^9\,M_\odot$ mass scales are negligible. The gravitational and density environments at $10^5\,R_g$ are sufficiently similar in both cases so that the $10^9\,M_\odot$ model yielded nearly identical results to the $10^8\,M_\odot$ counterpart. Therefore, simulation $M_\bullet = 10^8\,M_\odot$ is presented as a singular representative case for this low-interaction regime to avoid redundancy.

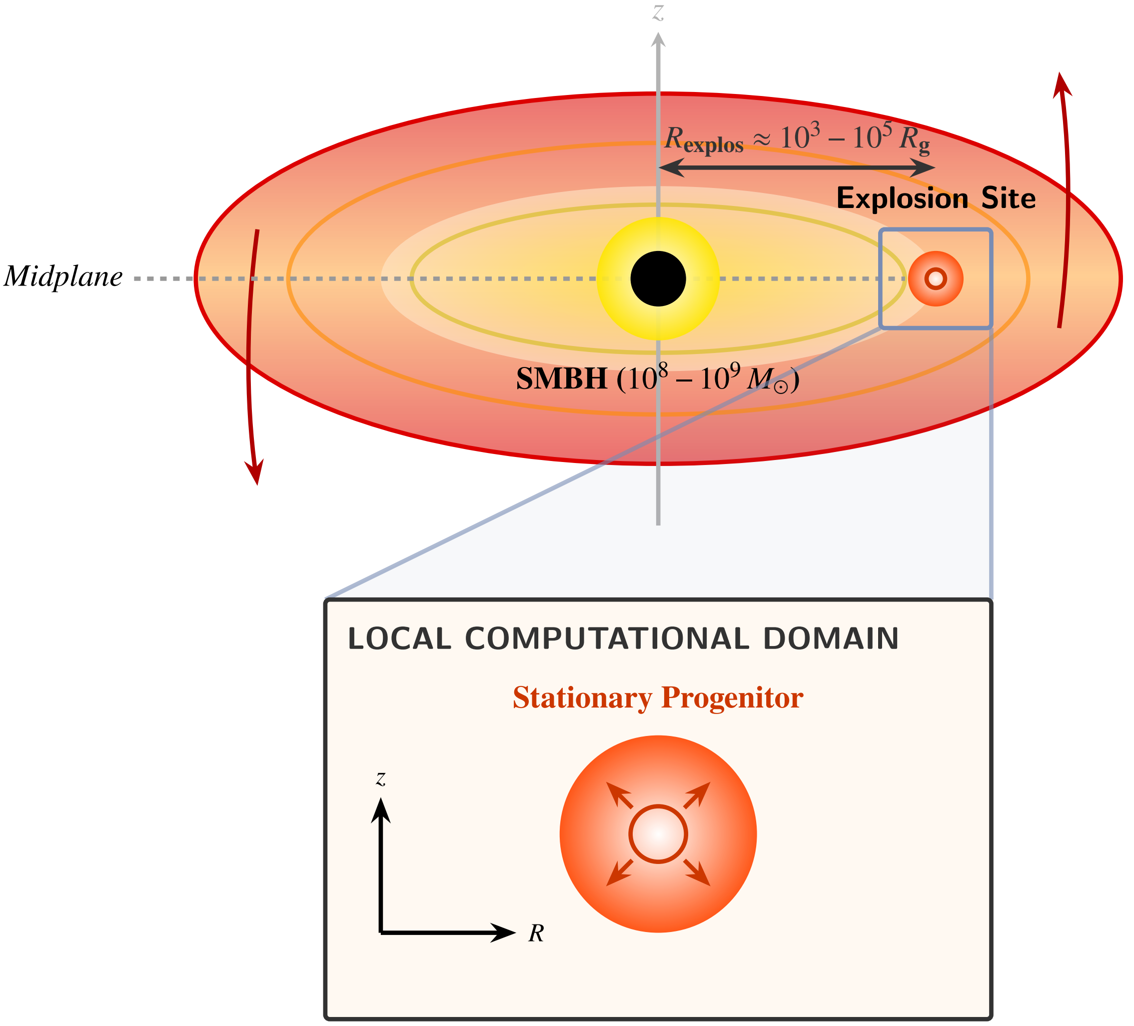

Figure 3.5: Schematic representation bridging the global AGN geometry and the local simulation framework detailed in Chapter 4.2. **Top:** The global edge-on view indicates the explosion site at $R_{\mathrm{explos}} \approx 10^3 - 10^5\, R_{\mathrm{g}}$. The framed technical callout highlights the specific region of interest, and the observer's line of sight maps to the 2D vertical cross-section modeled in *Castro*. **Bottom:** The zoomed-in local computational domain (R, z). By establishing a co-moving reference frame and assuming a stationary progenitor relative to the local gas ($v_{\mathrm{rel}} = 0$), the initial evolutionary phase behaves as a symmetric free expansion before shear forces dominate.

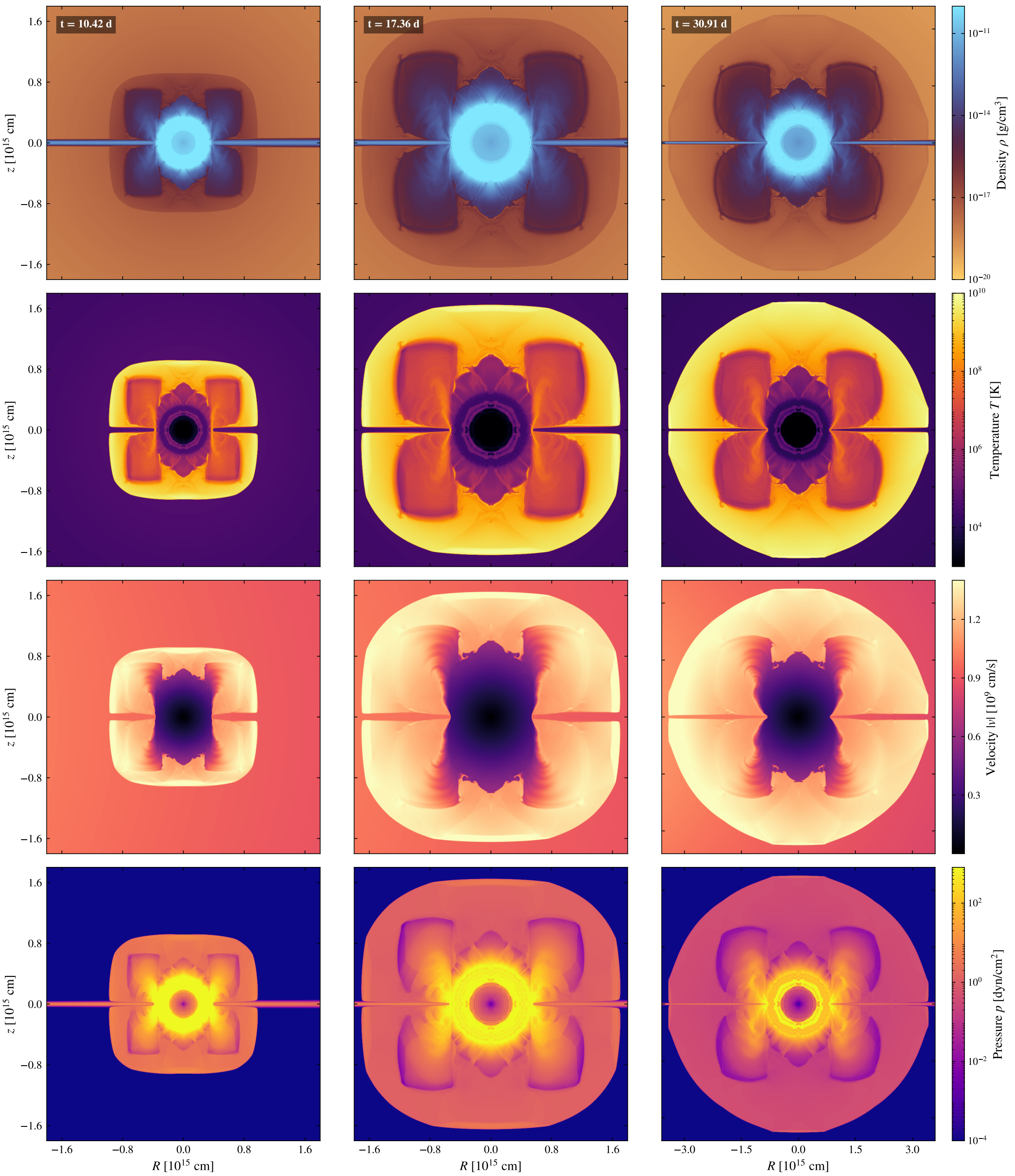

Figure 3.6: Evolution of a stationary SNR at $10^3\,R_\mathrm{g}$ from a $10^8\,M_\odot$ SMBH. Rows show ρ, T, $|v|$, and p; columns show snapshots at $t = 10.42, 17.36$, and 30.91 days.

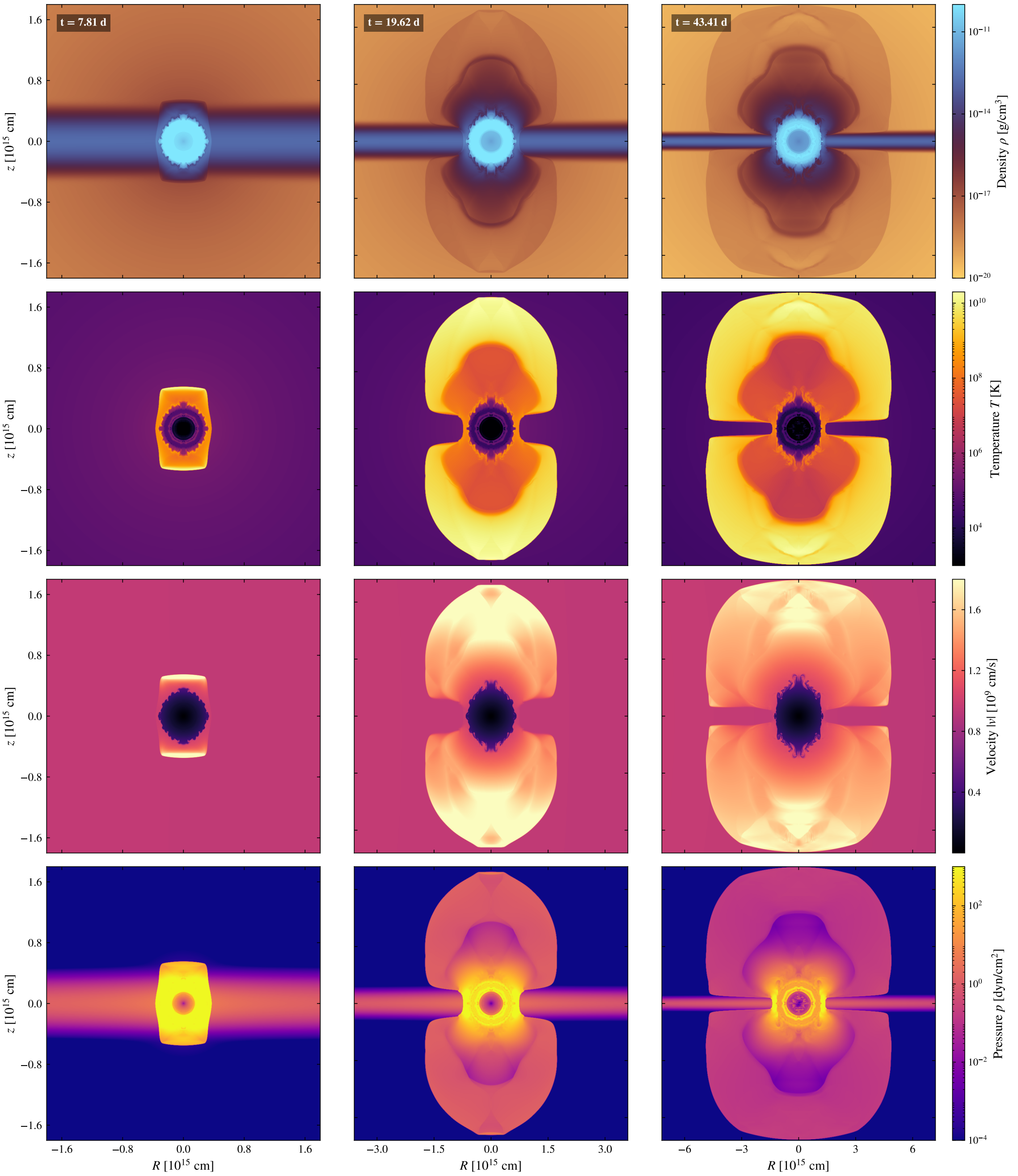

Figure 3.7: Evolution of a stationary SNR at $10^3\,R_{\rm g}$ from a $10^9\,M_\odot$ SMBH. Rows show ρ, T, $|v|$, and p; columns show snapshots at $t = 7.81, 19.62$, and 43.41 days.

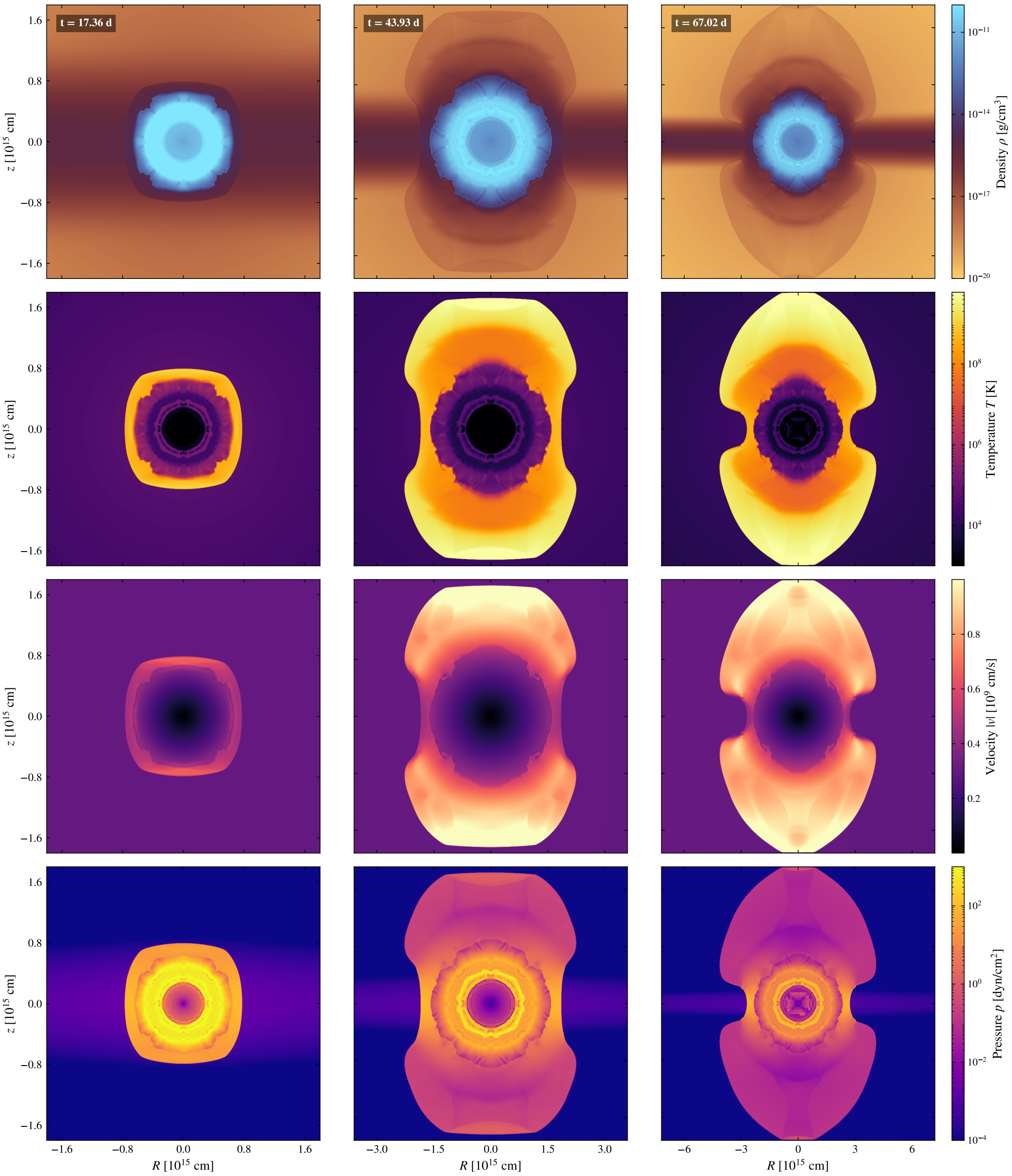

Figure 3.8: Stationary SNR evolution at $10^4\,R_{\rm g}$ ($10^8\,M_\odot$ SMBH). Rows show ρ, T, $|v|$, and p; columns show snapshots at $t = 17.36, 43.93$, and 67.02 days.

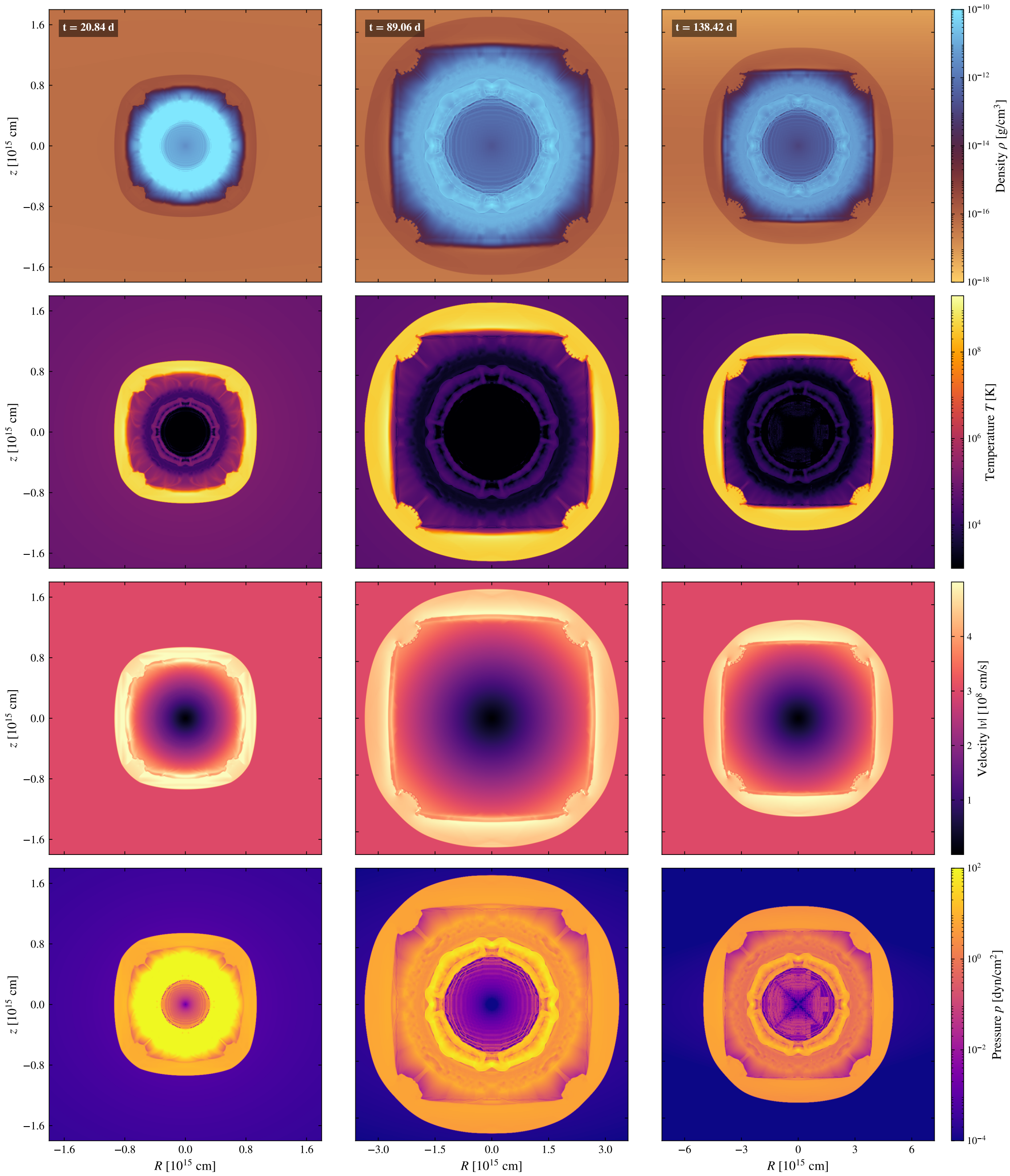

Figure 3.9: Stationary SNR evolution at $10^4\, R_g$ ($10^9\, M_\odot$ SMBH). Rows show ρ, T, $|v|$, and p; columns show snapshots at $t = 20.84, 89.06$, and 138.42 days.

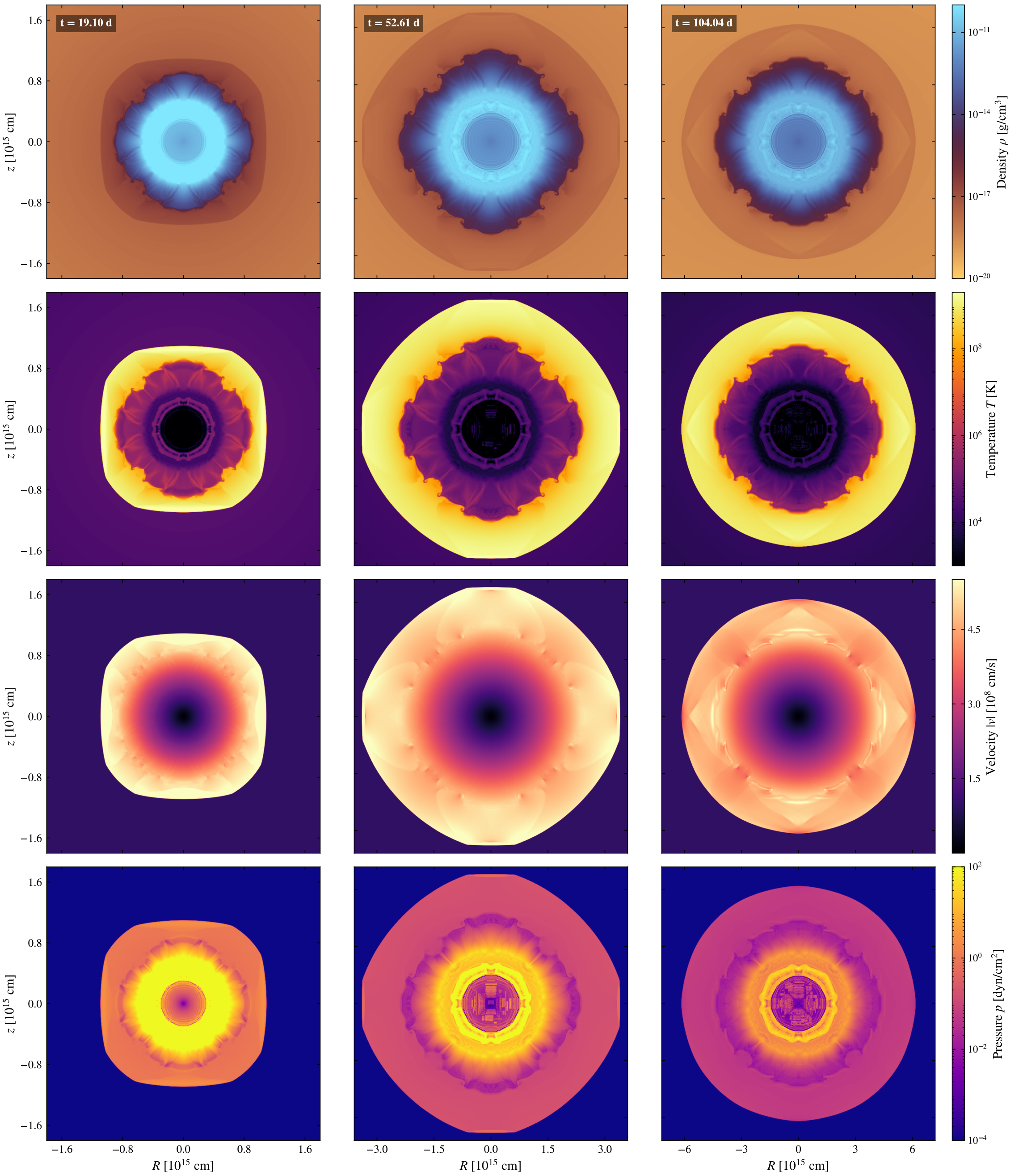

Figure 3.10: Stationary SNR evolution at the farthest simulated distance of $10^5\,R_\mathrm{g}$ ($10^8\,M_\odot$ SMBH). Rows show ρ, T, $|v|$, and p; columns show snapshots at $t = 19.10, 52.61$, and 104.04 days.

3.3 SN Evolution in Elliptical Orbits: Comparison of Apocenter and Pericenter Dynamics

This section examines the most complex scenarios in which the SN progenitor follows an elliptical orbit around the SMBH. Unlike stationary cases, these models account for the progenitor's orbital velocity (v_{orb}) at the moment of explosion, leading to significant morphological distortions due to the conservation of momentum and interaction with the rotating disk.

3.3.1 Comparative Analysis of Orbital Positions

The evolution of the SNR is mainly dictated by the magnitude of v_{orb}, which varies significantly between the apocenter and the pericenter.

Pericenter (R_{p})

At the closest point approach, the orbital velocity reaches its maximum value. The specific kinematic configuration, where the high orbital velocity creates a significant headwind drag ($\boldsymbol{v}_{\mathrm{rel}}$), is illustrated in Figure 3.12. For a $10^3\,R_{\mathrm{g}}$ distance near a $10^8\,M_{\odot}$ SMBH, the SNR exhibits extreme shear and reaches the domain boundaries in approximately 26.74 days. In the $10^9\,M_{\odot}$ case, the higher gravitational potential accelerates the progenitor to even greater velocities, causing the remnant to deform into a comet-like structure within only 11.98 days.

Apocenter (R_{a})

At the farthest point of the orbit, v_{orb} is at its minimum. In this regime, the Keplerian gas velocity dominates, overtaking the progenitor and creating a relative wind in the direction of orbital motion, as shown in Figure 3.11. The resulting morphology at $10^3\,R_{\mathrm{g}}$ ($10^8\,M_{\odot}$) is more symmetric than the pericenter counterpart, although a distinct "drift" relative to the SMBH is observed. The physical duration of the expansion within the computational grid is significantly longer.

Velocity Fields

Linear velocity maps indicate that the expansion is heavily biased in the direction of orbital motion. In pericenter models, velocity magnitudes exceed 4.5×10^9 cm/s for $10^8\,M_{\odot}$ and reach 6.0×10^9 cm/s for $10^9\,M_{\odot}$.

3.3.2 Radial Scaling and Mass Influence

The impact of orbital dynamics is highly sensitive to the radial distance (R_{g}) from the SMBH and the mass of the central object.

Scaling with SMBH Mass

The $10^9\,M_\odot$ models involve larger spatial domains. These systems exhibit higher absolute orbital velocities, leading to more rapid shock deformation even at larger radii compared to the $10^8\,M_\odot$ models.

Distance Influence (10^3 to $10^5\,R_\mathrm{g}$)

At $10^4\,R_\mathrm{g}$, the SNR remains contained within the disk structure for longer periods, showing a transition from extreme shear to a constrained bipolar expansion. At the maximum distance of $10^5\,R_\mathrm{g}$, the orbital velocity becomes almost negligible relative to the SN expansion speed; consequently, both the apocenter and pericenter models result in nearly isotropic spherical remnants.

3.3.3 Thermodynamic Implications

The interaction between the SN shock and the stratified disk medium produces intense thermal and pressure responses.

Thermal Response

Temperature maps consistently show shock-heated regions exceeding 10^9 K at the interface between the SNR and the dense midplane.

Pressure Peaks

Logarithmic pressure distributions reveal peak values between 10^2 and 10^4 dyn/cm^2 on the interaction front.

3.4 Comparative Analysis: Stationary vs. Apocenter Evolution at Equivalent Radii

A key focus of this study is the comparison between the ”stationary” models ($v_\mathrm{orb} = 0$) and the elliptical models at the apocenter (R_a), as both scenarios initiate the explosion at the same radial distance from the SMBH. Since the local density of the accretion disk and the gravitational potential are identical in both cases, any observed differences in the SNR evolution are strictly attributable to the inherited orbital momentum of the progenitor.

3.4.1 Center of Expansion and Orbital Drift

In stationary cases, the center of the supernova remains fixed relative to the SMBH, allowing the shock wave to interact symmetrically with the local disk environment. Conversely, in the apocenter models, the entire SNR inherits a non-zero velocity vector. This leads to a measurable orbital drift, where the geometric center of the remnant shifts along the orbital path during its expansion.

3.4.2 Morphological Asymmetry

Although both models exhibit the characteristic ”hour-glass” shape as a result of the vertical density gradient of the disk, the apocenter cases show a slight ”tilting” or shearing of the lobes. This is a result of the expansion velocity vector shifting against the Keplerian rotation of the disk material, a phenomenon entirely absent in the stationary configurations.

3.4.3 Computational Domain Interaction

Despite the relatively low velocity at the apocenter, the inherited momentum causes the SNR to reach the outer boundaries of the computational domain earlier than in the stationary case. This comparison demonstrates that even at the farthest point of an orbit, where the orbital velocity is at its minimum, the dynamic state of the progenitor significantly alters the late-stage symmetry of the remnant compared to a stationary explosion.

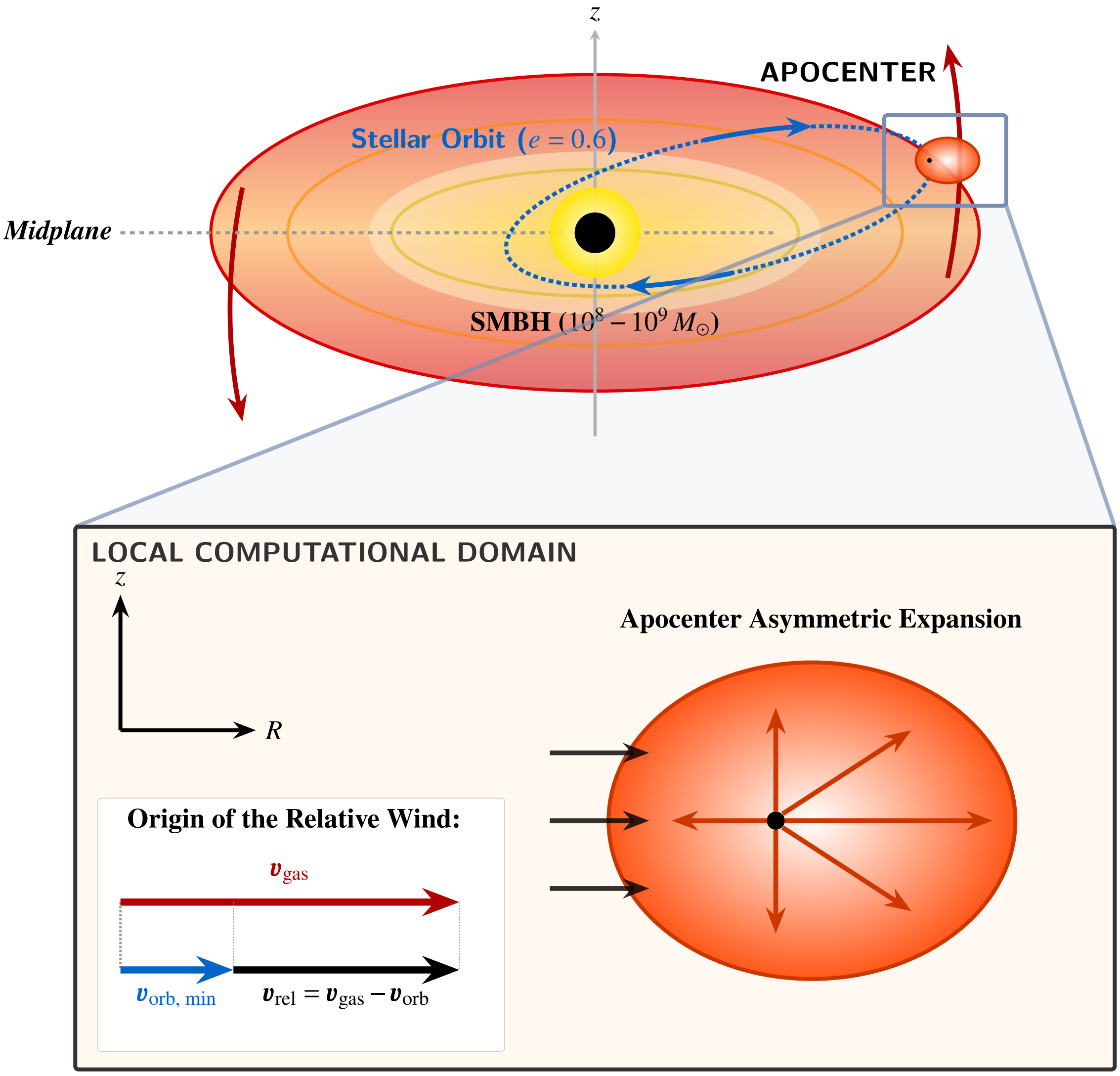

Figure 3.11: Configuration of the apocenter explosion ($e = 0.6$). **Top:** Global view of the stellar orbit within the AGN disk. **Bottom:** The local computational domain. The diagram illustrates how the faster Keplerian gas ($\boldsymbol{v}_{\rm gas}$) overtakes the slower progenitor ($\boldsymbol{v}_{\rm orb,min}$), creating a distinct relative wind ($\boldsymbol{v}_{\rm rel}$). This kinetic shear drives the asymmetric, bow-shock expansion of the SN observed in the hydrodynamic models.

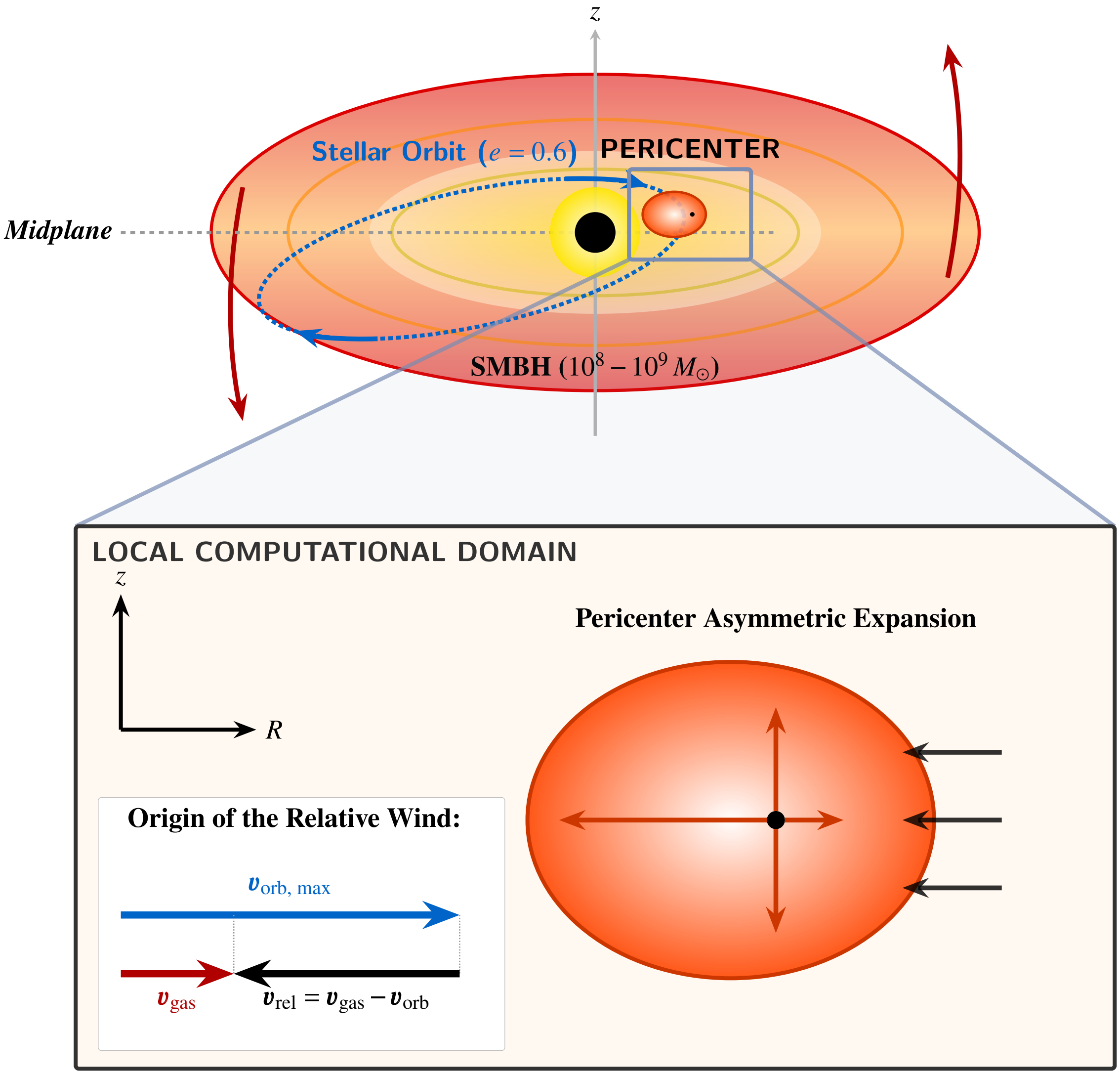

Figure 3.12: Configuration of the pericenter explosion ($e = 0.6$). **Top:** Global view with mirrored stellar orbit. **Bottom:** The local computational domain. Due to the high orbital velocity ($v_{\mathrm{orb,max}}$), the star encounters significant headwind drag (v_{rel}), compressing the leading edge (upstream) and elongating the SN in the downstream direction.

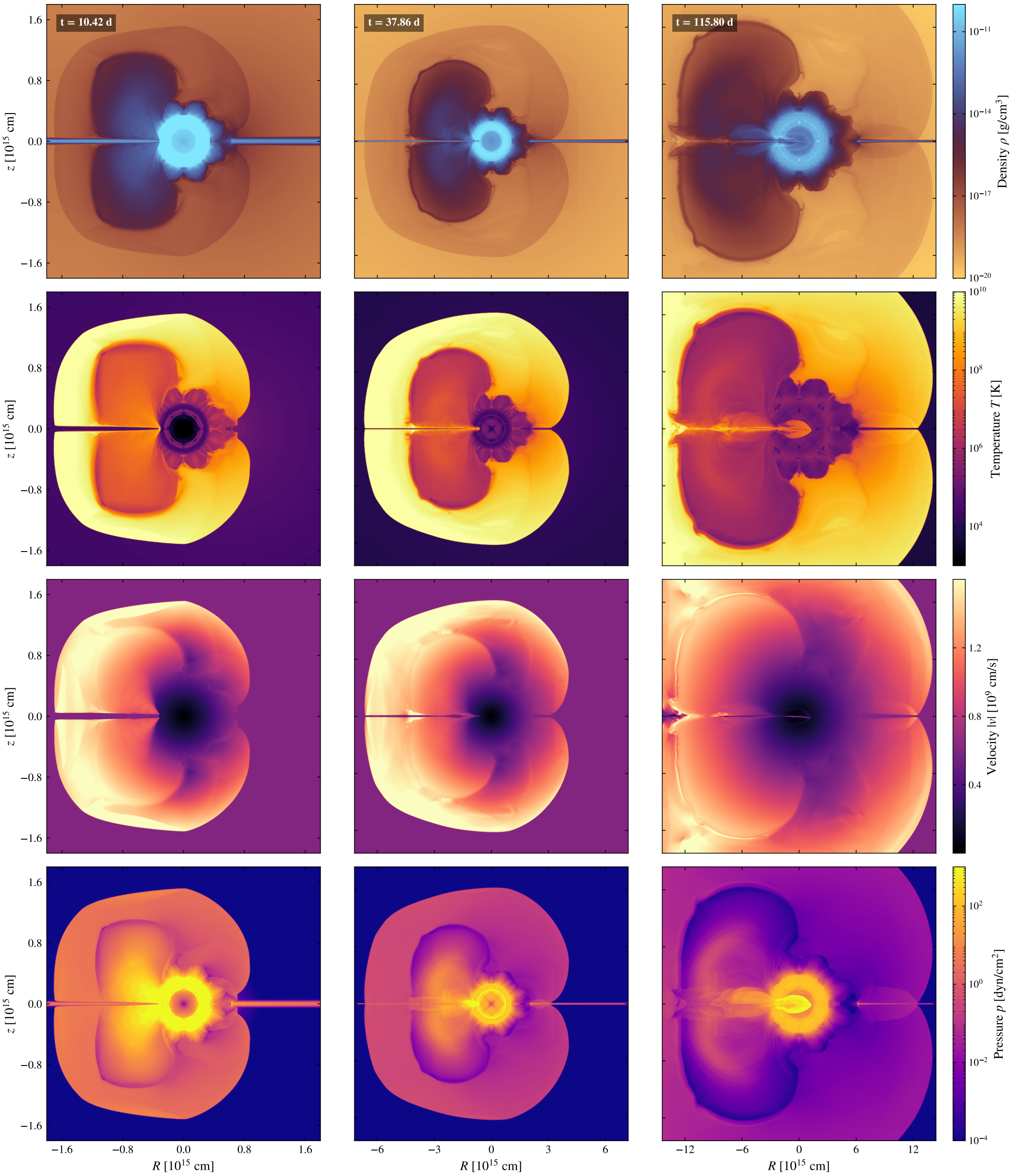

Figure 3.13: Evolution of an SNR at the apocenter of an elliptical orbit ($10^3\,R_\mathrm{g}$, $10^8\,M_\odot$ SMBH). Rows show ρ, T, $|v|$, and p; columns show snapshots at $t = 10.42, 37.86$, and 115.80 days. At minimum orbital velocity, the remnant maintains a relatively symmetric ”hour-glass” shape with a slight lateral drift.

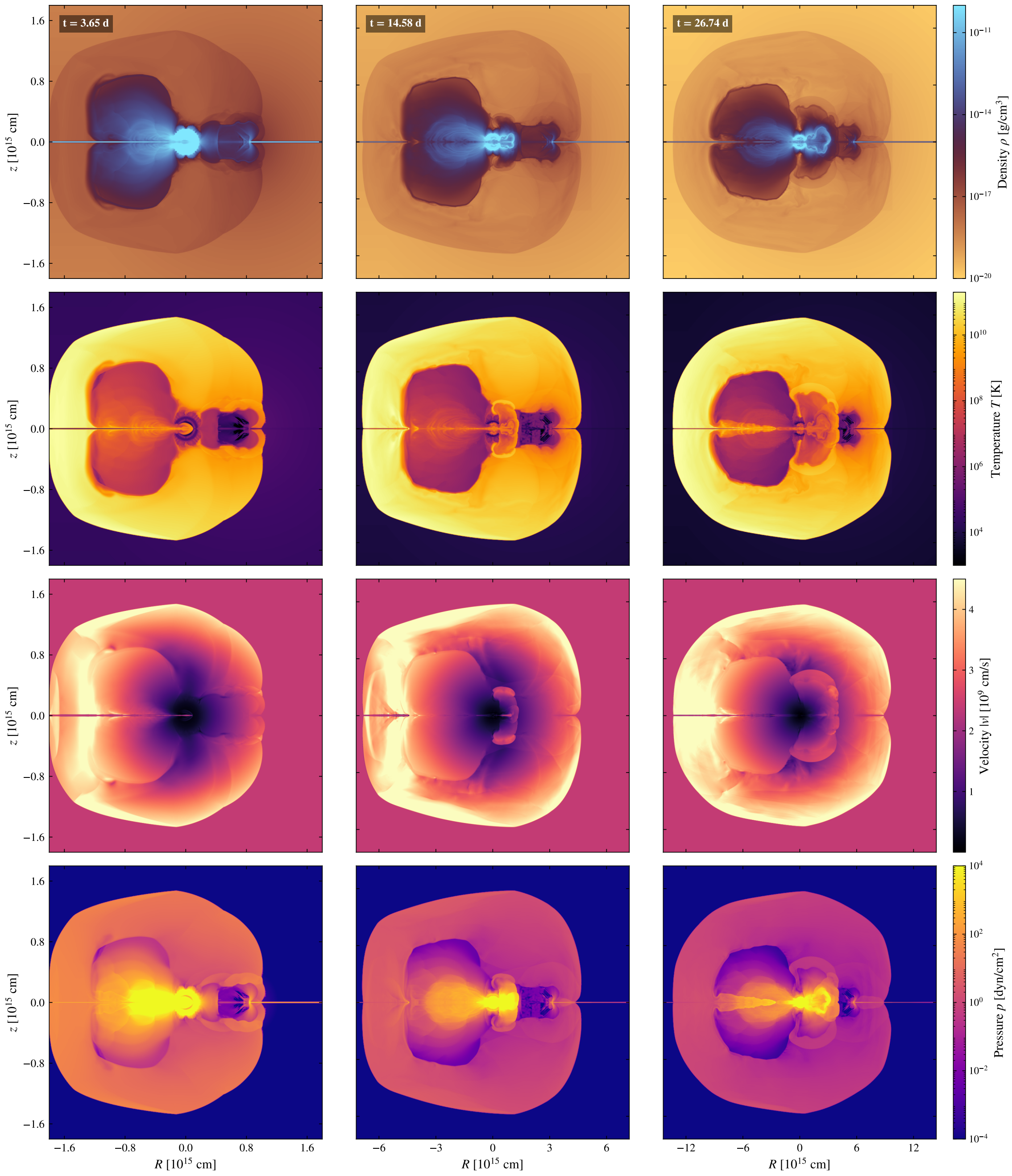

Figure 3.14: Evolution of an SNR at the pericenter ($250\,R_\mathrm{g}$, $10^8\,M_\odot$ SMBH). Rows show ρ, T, $|v|$, and p; columns show snapshots at $t = 3.65, 14.58$, and 26.74 days. The maximum orbital velocity leads to severe shearing, stretching the remnant along the orbital path and significantly shortening its interaction time within the domain.

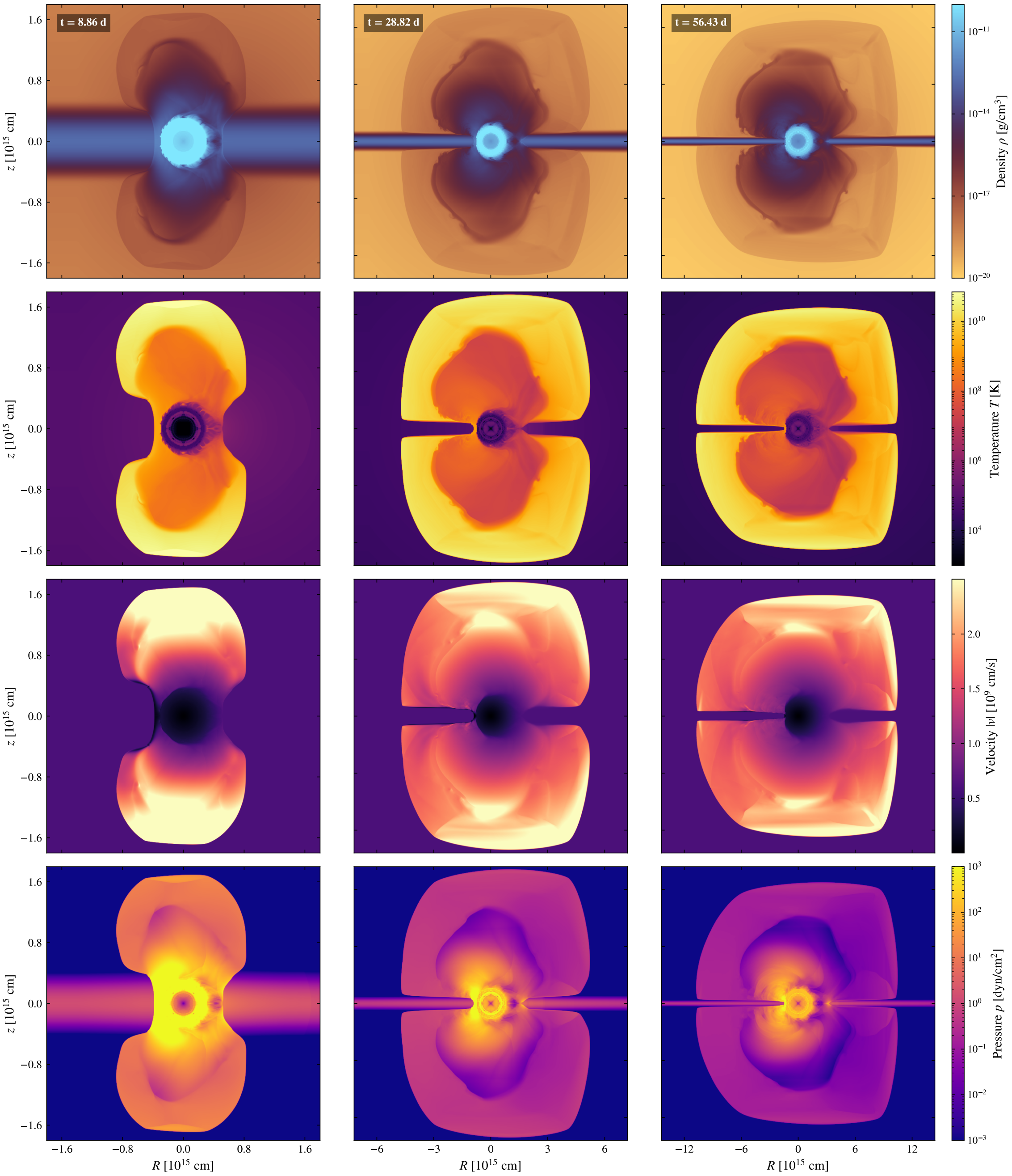

Figure 3.15: SNR evolution at the apocenter for a $10^9\,M_\odot$ SMBH ($10^3\,R_\mathrm{g}$). Rows show ρ, T, $|v|$, and p; columns show snapshots at $t = 8.86, 28.82$, and 56.43 days. Despite the higher mass, the lower velocity at the apocenter allows for a more sustained expansion compared to the pericenter counterpart.

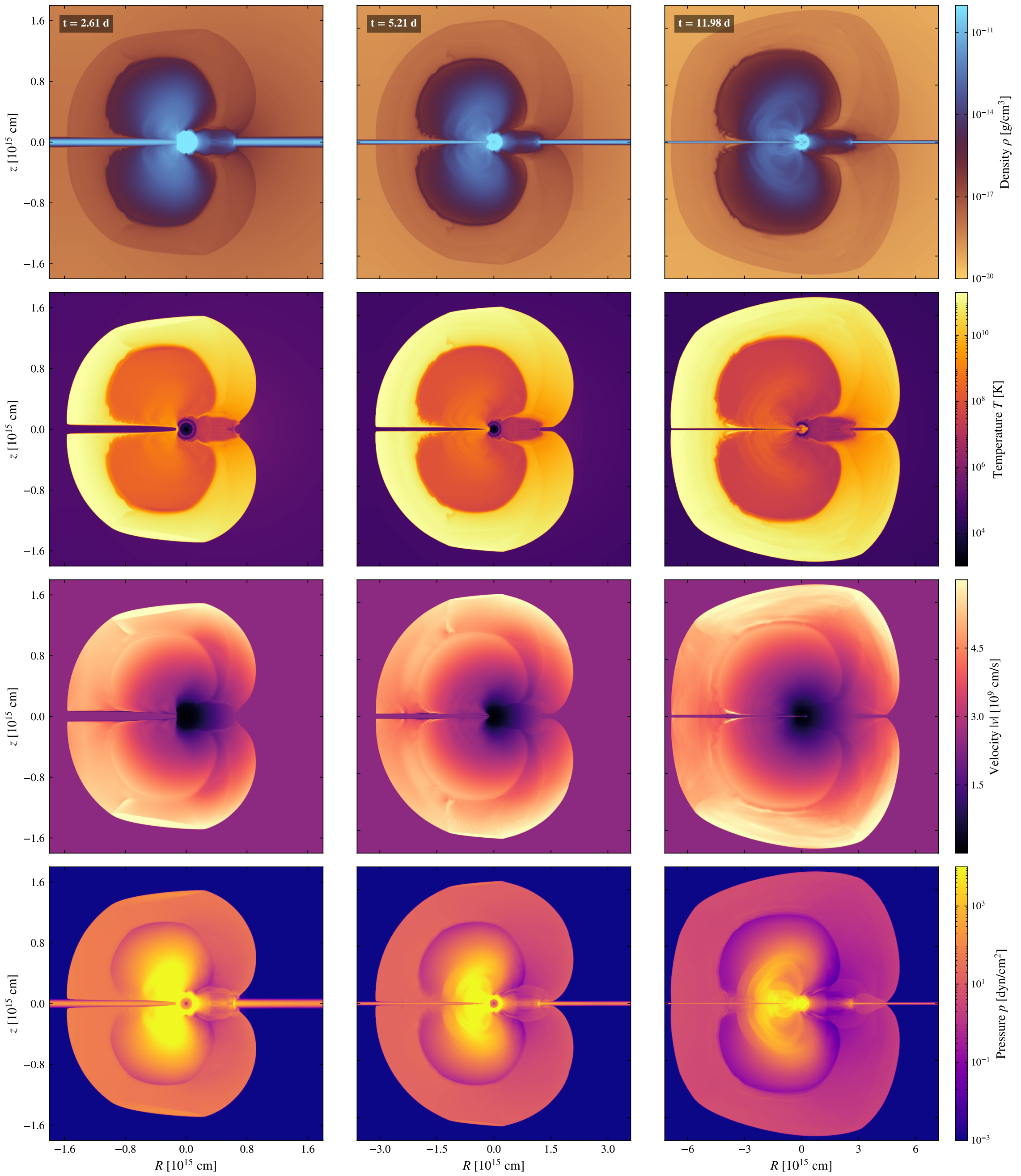

Figure 3.16: SNR evolution at the pericenter for a $10^9\,M_\odot$ SMBH ($250\,R_\mathrm{g}$). Rows show ρ, T, $|v|$, and p; columns show snapshots at $t = 2.61, 5.21$, and 11.98 days. Extreme orbital shearing is evident, with the remnant being rapidly distorted into a comet-like structure due to the intense gravitational acceleration.

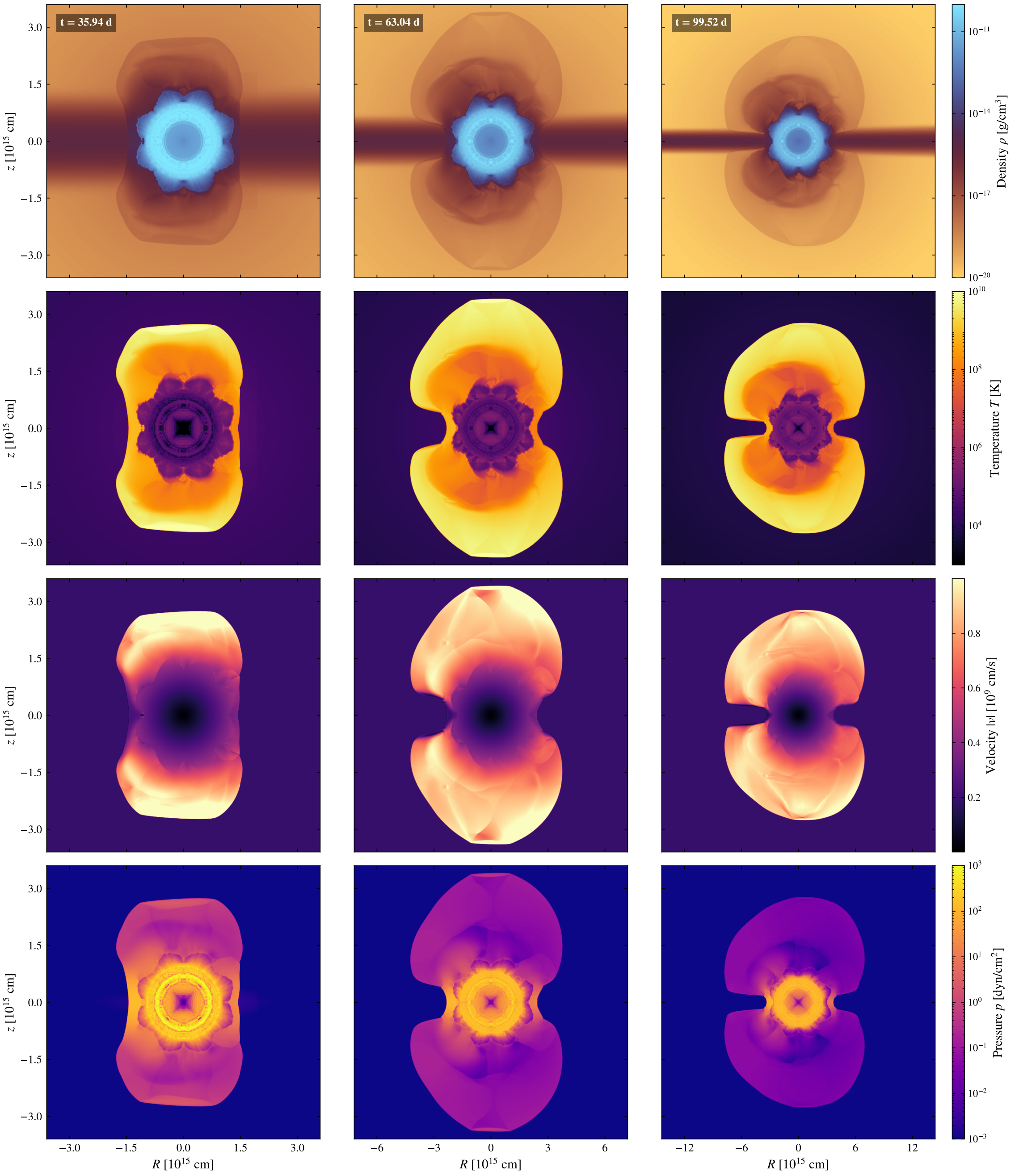

Figure 3.17: SNR at the apocenter ($10^4\,R_g$, $10^8\,M_\odot$ SMBH). Rows show ρ, T, $|v|$, and p; columns show snapshots at $t = 35.94, 63.04$, and 99.52 days. The reduced influence of the disk's density gradient at this distance results in a more expanded and less "pinched" morphology.

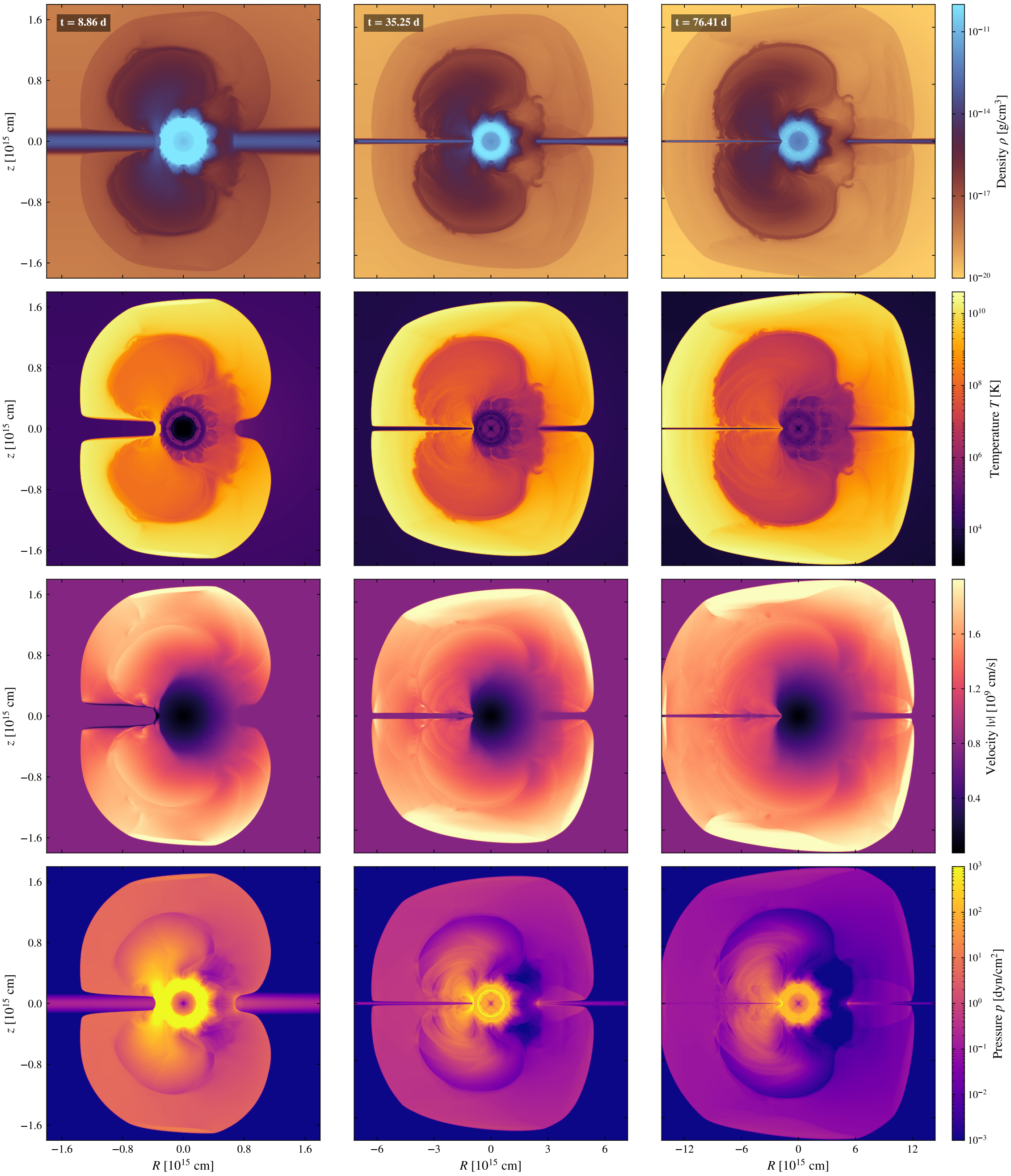

Figure 3.18: SNR at the pericenter ($2500\,R_{\rm g}$, $10^8\,M_\odot$ SMBH). Rows show ρ, T, $|v|$, and p; columns show snapshots at $t = 8.86, 35.25$, and 76.41 days. While shearing is still present, the remnant's expansion is more isotropic than in the $10^3\,R_{\rm g}$ case, though it remains biased by the orbital momentum.

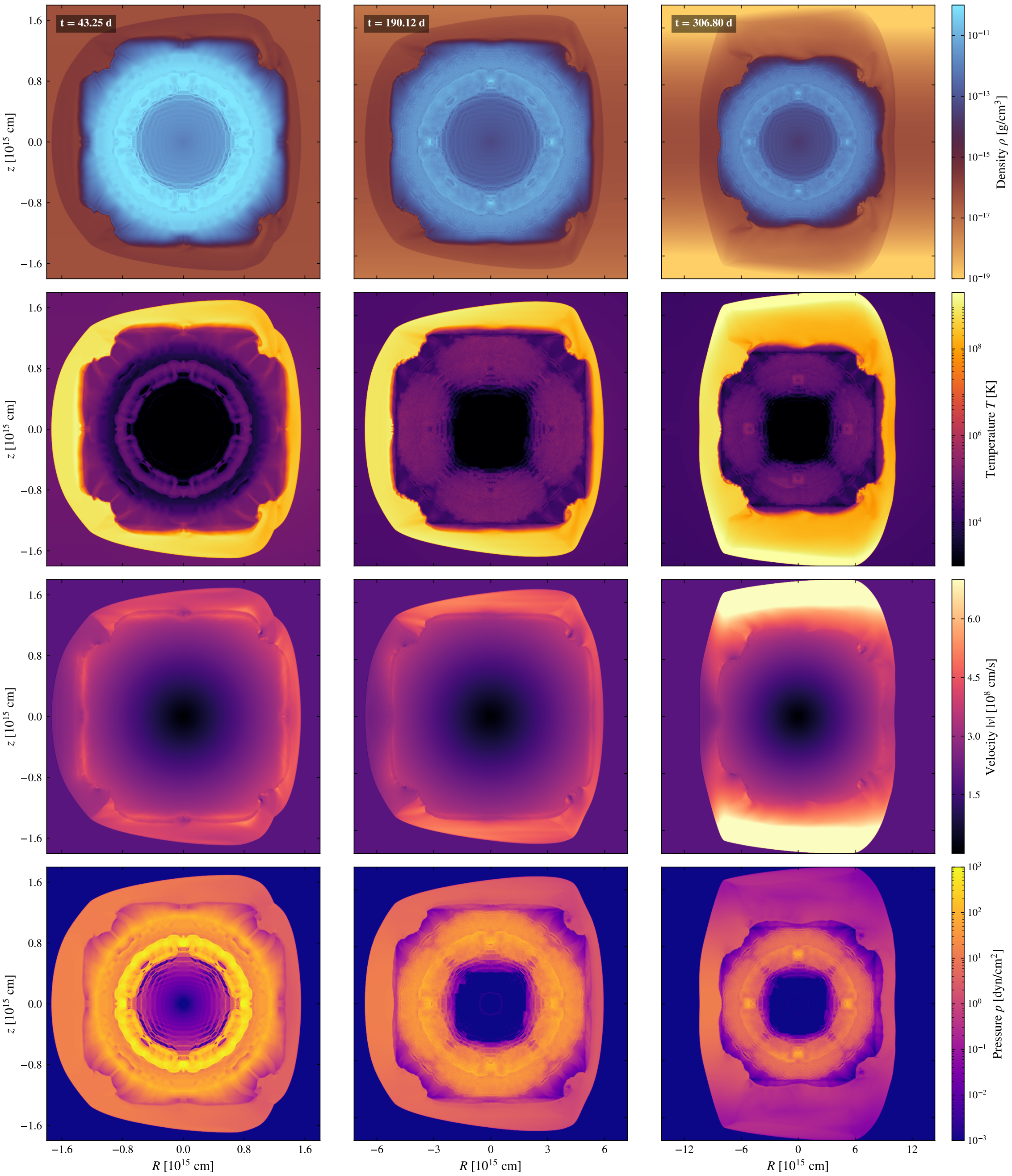

Figure 3.19: SNR evolution at the apocenter ($10^4\,R_g$, $10^9\,M_\odot$ SMBH). Rows show ρ, T, $|v|$, and p; columns show snapshots at $t = 43.25, 190.12$, and 306.80 days. The larger physical scale of the $10^9\,M_\odot$ system allows for long-term monitoring of the remnant's cooling phase.

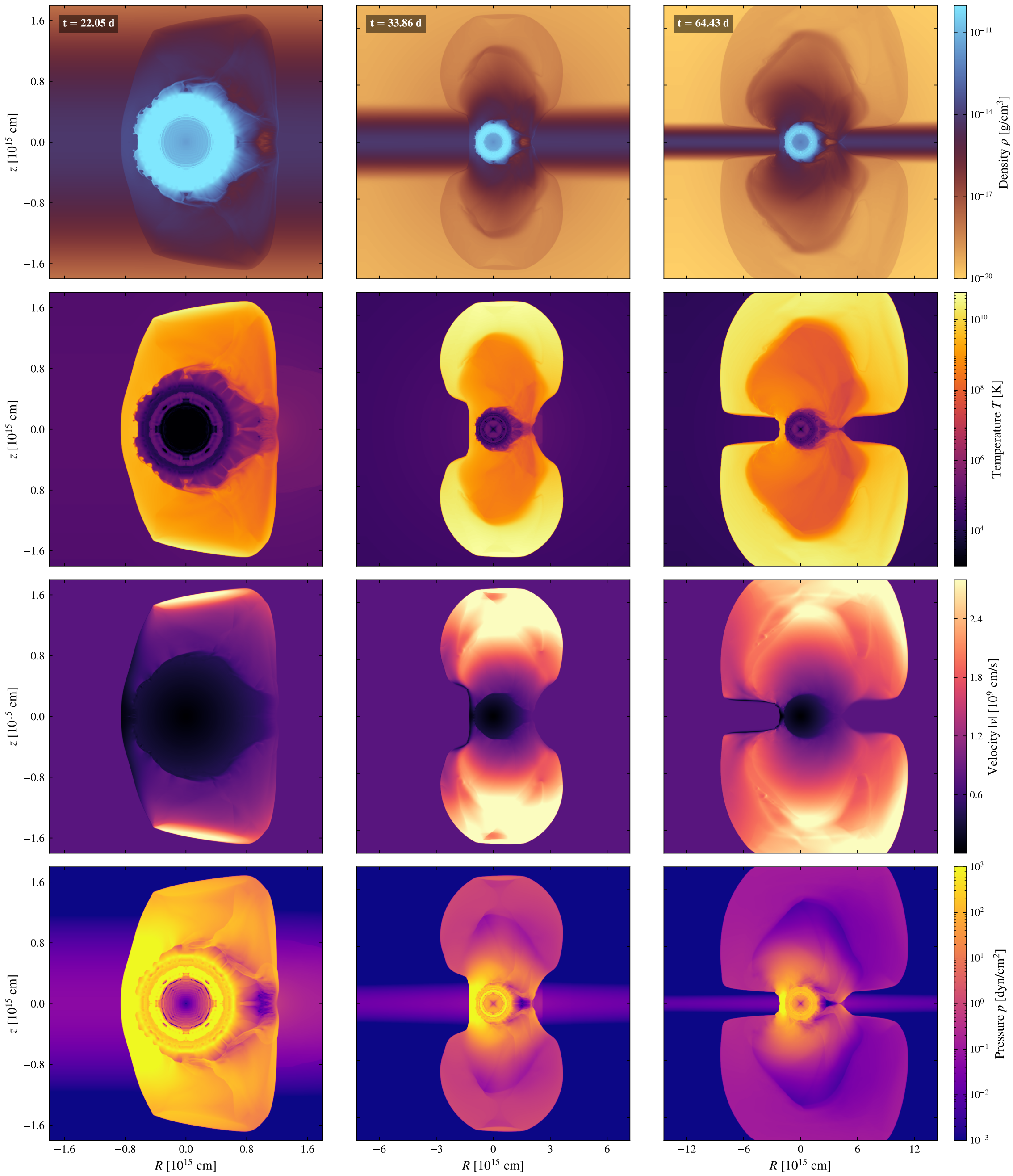

Figure 3.20: SNR evolution at the pericenter ($2500\,R_\mathrm{g}$, $10^9\,M_\odot$ SMBH). Rows show ρ, T, $|v|$, and p; columns show snapshots at $t = 22.05, 33.86,$ and 64.43 days. Significant deformation is observed, illustrating the persistent impact of the orbital velocity even at intermediate radial distances.

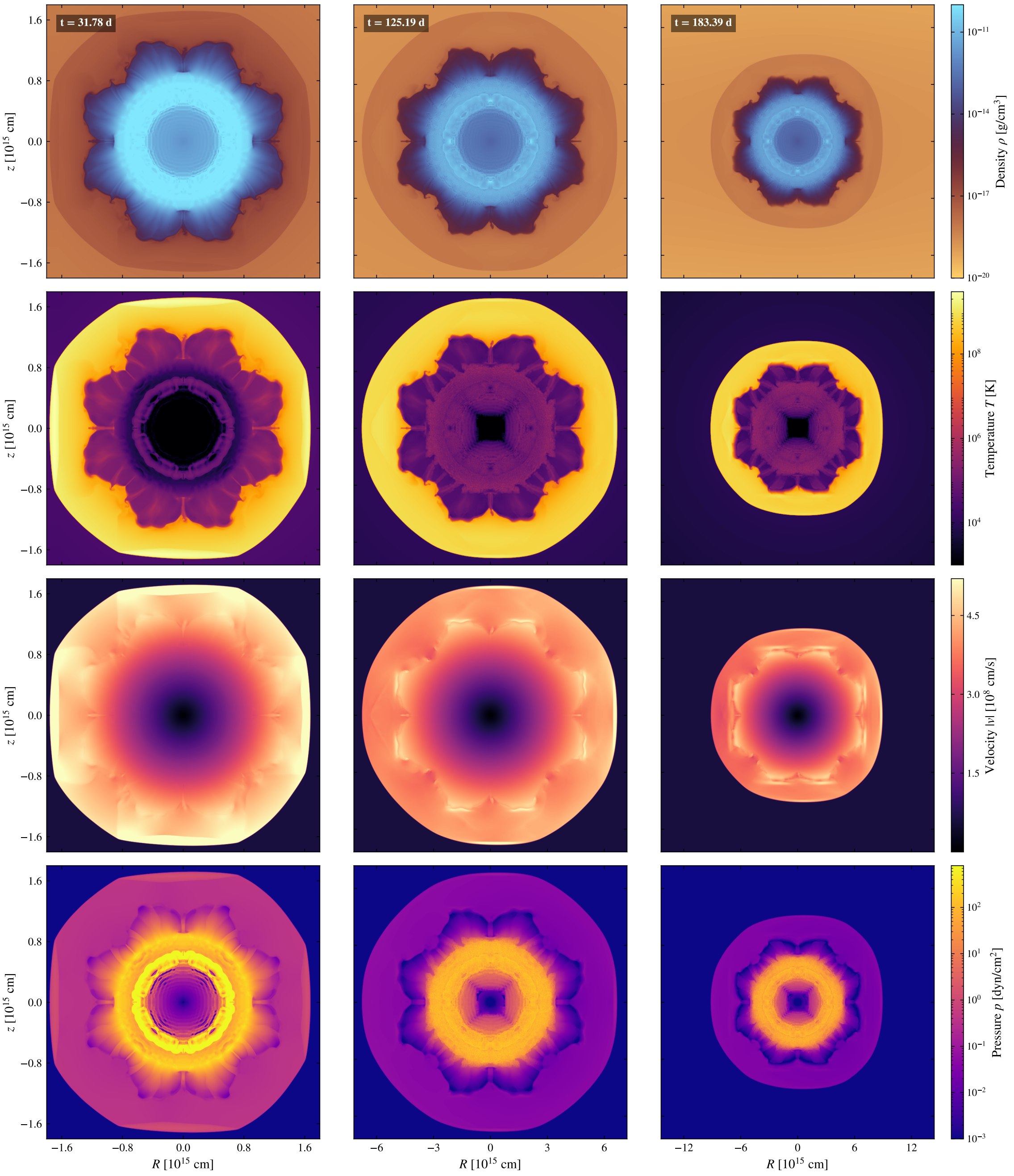

Figure 3.21: SNR evolution at the apocenter for the farthest simulated distance ($10^5\,R_g$, $10^8\,M_\odot$ SMBH). Rows show ρ, T, $|v|$, and p; columns show snapshots at $t = 31.78, 125.19$, and 183.39 days. The expansion is nearly spherical, as the orbital velocity is negligible compared to the expansion speed.

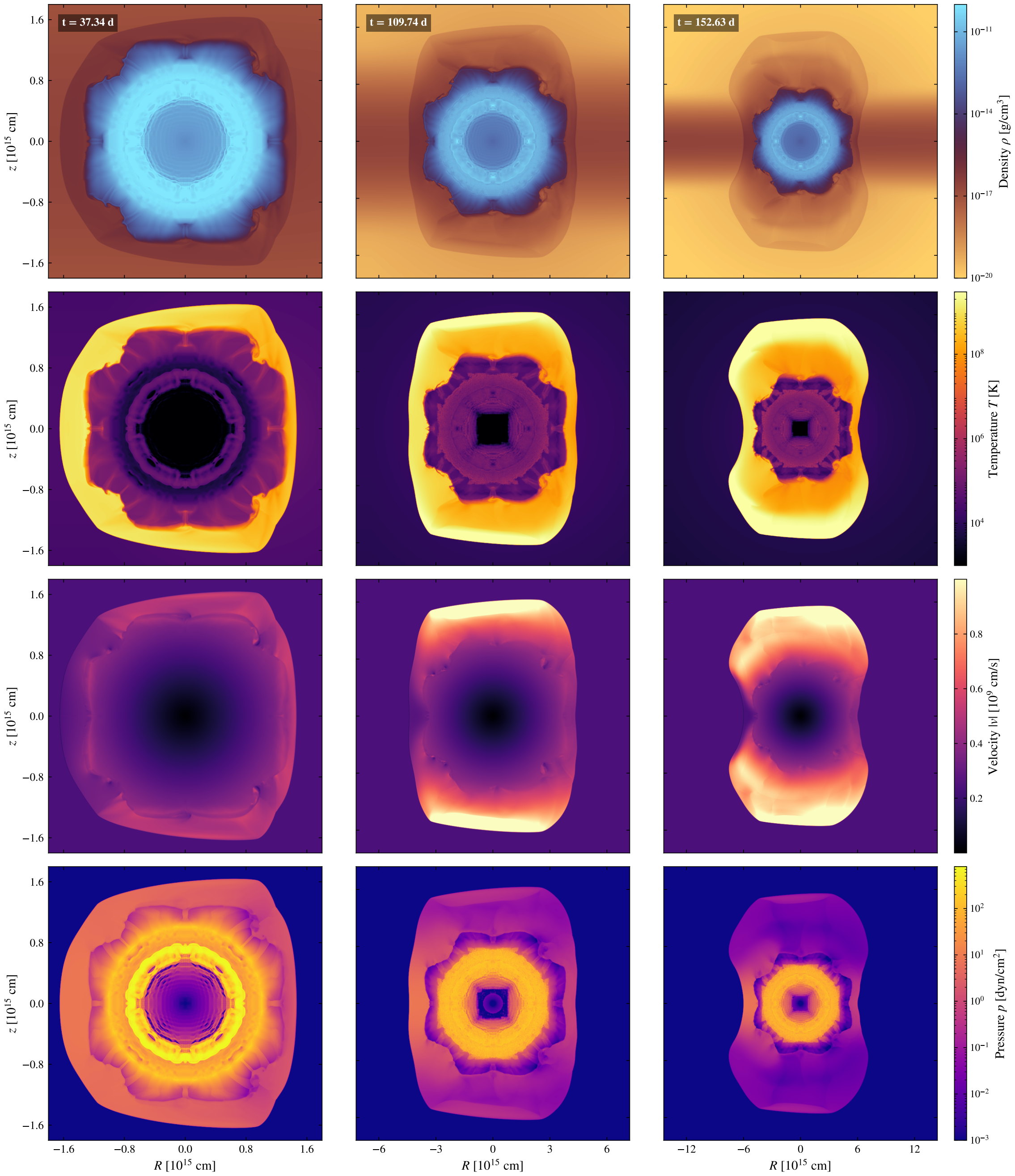

Figure 3.22: SNR evolution at the pericenter (25000 R_g, $10^8\,M_\odot$ SMBH). Rows show ρ, T, $|v|$, and p; columns show snapshots at $t = 37.34, 109.74$, and 152.63 days. Similar to the apocenter case, the morphology is isotropic, confirming that the influence of the SMBH environment diminishes at large radii.

3.5 Post-processing Reconstruction of Light Curves

To bridge the gap between our hydrodynamic simulations and observable astrophysical signatures, we performed an analytical reconstruction of the light curves. Since the *Castro* simulations were conducted in the adiabatic regime to prioritize the capture of large-scale shock morphology, the radiative losses must be estimated through post-processing.

3.5.1 The Optically Thin Approximation

The primary assumption underlying our luminosity calculation is the optically thin approximation. In the context of SNRs expanding into the dilute environment of an AGN accretion disk, we assume that the gas density is sufficiently low such that any photon emitted via radiative processes can escape the computational domain without being re-absorbed by the surrounding medium (van Marle and Keppens, 2011).

This approach is physically justified for several reasons

- **Local nature of energy loss:** Under this approximation, radiative cooling becomes a purely local phenomenon. The energy loss of a gas parcel depends solely on its local density, temperature, and ionization state, rather than on the global radiation field.

- **Physical regime:** Astrophysical phenomena in galactic nuclei, despite the presence of accretion disks, often operate in density regimes where the mean free path of a photon is large compared to the scale of the shock front.

3.5.2 Relativistic Doppler Beaming

Since the progenitor and the subsequent SNR ejecta travel at significant fractions of the speed of light in close proximity to the SMBH, the emitted radiation is subject to relativistic Doppler beaming. The observed luminosity is highly sensitive to the orientation of the velocity vector relative to the line of sight of the observer (Urry and Padovani, 1995).

The relativistic aberration and the Doppler shift are encapsulated by the Doppler factor D as

$$D = \frac{1}{\gamma\,(1-\beta\cos\theta)}, \tag{3.1}$$

where $\beta = v/c$ is the velocity of the ejecta relative to the speed of light, θ is the angle between the velocity vector of the source and the line of sight to the observer, and γ is the Lorentz factor defined as:

$$\gamma = \frac{1}{\sqrt{1-\beta^2}}. \tag{3.2}$$

For a continuously emitting source or an expanding shell, the observed bolometric luminosity L_{obs} scales with the emitted rest-frame luminosity L_{emit} according to:

$$L_{\text{obs}} = D^4 L_{\text{emit}}. \tag{3.3}$$

Equation (3.3) explains why even small changes in the velocity vector $\boldsymbol{v}$ of the shock front produce massive disparities in synthetic light curves when viewed from different directions.

3.5.3 Magnitude Conversion and IAU Standard

To facilitate a direct comparison between the theoretical luminosity outputs of our models and real-world astronomical observations, the calculated bolometric luminosity L (expressed in erg s^{-1}) is converted into the absolute bolometric magnitude M.

Following the nominal standard established by the International Astronomical Union (IAU), the conversion is defined by the logarithmic (Pogson's) relation:

$$M = M_{\mathrm{bol},\odot} - 2.5\log_{10}\left(\frac{L}{L_\odot}\right), \tag{3.4}$$

where $M_{\mathrm{bol},\odot} = 4.74$ is the nominal absolute bolometric magnitude of the Sun and $L_\odot = 3.828\times10^{33}$ erg s^{-1} represents the solar luminosity. In our post-processing and visualization pipeline, Equation (3.4) is implemented in a linearized form to compute the secondary z-axis of the light curve plots:

$$M = 88.6974 - 2.5\log_{10}(L). \tag{3.5}$$

This calibration ensures that the high-energy transients produced in our simulations are presented in a standard unit system familiar to observational astrophysics, allowing for an immediate assessment of the event's peak brightness.

3.5.4 Mathematical Formulation

To quantify instantaneous luminosity, we adopt the semi-implicit radiative cooling scheme proposed by van Marle and Keppens (2011). The evolution of the energy density e due to radiative sink terms is expressed as:

$$e^{n+1} = e^n - n_i^n n_e^n \Lambda(T^{n+1})\Delta t^n, \tag{3.6}$$

where n_i and n_e are the densities of local ion and electron numbers, and $\Lambda(T)$ represents the tabulated cooling function dependent on the future temperature T^{n+1}. For the purpose of our analytical light curve reconstruction, we adopt a characteristic cooling rate of $\log_{10}(\Lambda) = -23.25$ [erg cm^3 s^{-1}]. This specific value was obtained from a fit to the cooling curve in the temperature range relevant to our simulated shock fronts, ensuring that the estimated luminosity reflects the physical state of the shocked gas. By integrating this local energy loss across the entire grid for each time step, we derive the total bolometric luminosity $L(t)$, effectively generating the synthetic light curve for the simulated event.

3.5.5 Light Curve Generation in the *SEDONA* Code

Reconstruction of observables, such as light curves and spectra, is achieved in *SEDONA* through a multi-dimensional, time-dependent Monte Carlo (MC) radiation transport scheme (Kasen et al., 2006). This method avoids directly solving the complex partial differential equations of radiation transfer by simulating the stochastic behavior of the radiation field.

Discretization into Energy Packets

The fundamental principle of the *SEDONA* code is the discretization of the radiation field into a large number of individual ”energy packets.” Each packet represents a collection of photons with a specific total energy and frequency. These packets are emitted from energy sources within the ejecta.

Stochastic Transport and Interactions

Once emitted, the propagation of each packet is followed through the expanding envelope as a series of stochastic events:

- **Random walks**: Packets travel along paths determined by the local opacity of the medium, which includes both continuum and line interactions.
- **Scattering and absorption**: When a packet interacts with the gas, it is either scattered or absorbed and immediately re-emitted. The probability of these events is calculated using physical cross-sections and atomic line data, often employing the Sobolev approximation for line opacities in expanding flow (Chen et al., 2025).
- **Doppler effects**: As packets move between velocity layers in the expanding ejecta, their frequencies are explicitly Doppler-shifted, ensuring that the energy exchange between radiation and matter is accurately captured.

Packet Collection and Time-Binning

The final light curve is generated by collecting packets that reach the outer boundary of the computational domain. Each escape packet is characterized by its energy, frequency, and exit direction. These packets are then ”binned” into discrete time intervals based on their arrival time at a virtual observer.

The total luminosity at a given time $L(t)$ is determined by the sum of the energies of all packets that arrive within that specific time bin. This statistical approach allows *SEDONA* to produce synthetic light curves that account for the 3D geometry of the explosion and the viewing angle of the observer.

3.6 Results and Light Curve Analysis

Based on the analytical reconstruction and the radiative transfer calculations described in the previous section, we present the synthetic light curves for our three distinct scenarios. These scenarios involve a SN expanding into the environment of a SMBH, varying either the distance from the SMBH ($R = 10^3\ R_\mathrm{g}$ vs. $R = 10^4\ R_\mathrm{g}$) or the mass of the SMBH ($M_\bullet = 10^8\,M_\odot$ vs. $M_\bullet = 10^9\,M_\odot$).

To account for the viewing angle and the relativistic nature of the environment, we present both ”left” and ”right” side light curves for each scenario (relative to the observer’s line of sight). Furthermore, we distinguish between the total bolometric luminosity, calculated in the frequency range $10^{14} - 3\times10^{16}$ Hz, and the visual luminosity, calculated in the frequency range $4\times10^{14} - 7.9\times10^{14}$ Hz.

3.6.1 Individual Scenarios

Scenario A: $R = 10^3\ R_g$, $M_\bullet = 10^8\ M_\odot$

Figure 3.23 displays the reconstructed light curve for the SN exploding at a distance of $R = 10^3\ R_g$ from an SMBH of mass $10^8\ M_\odot$.

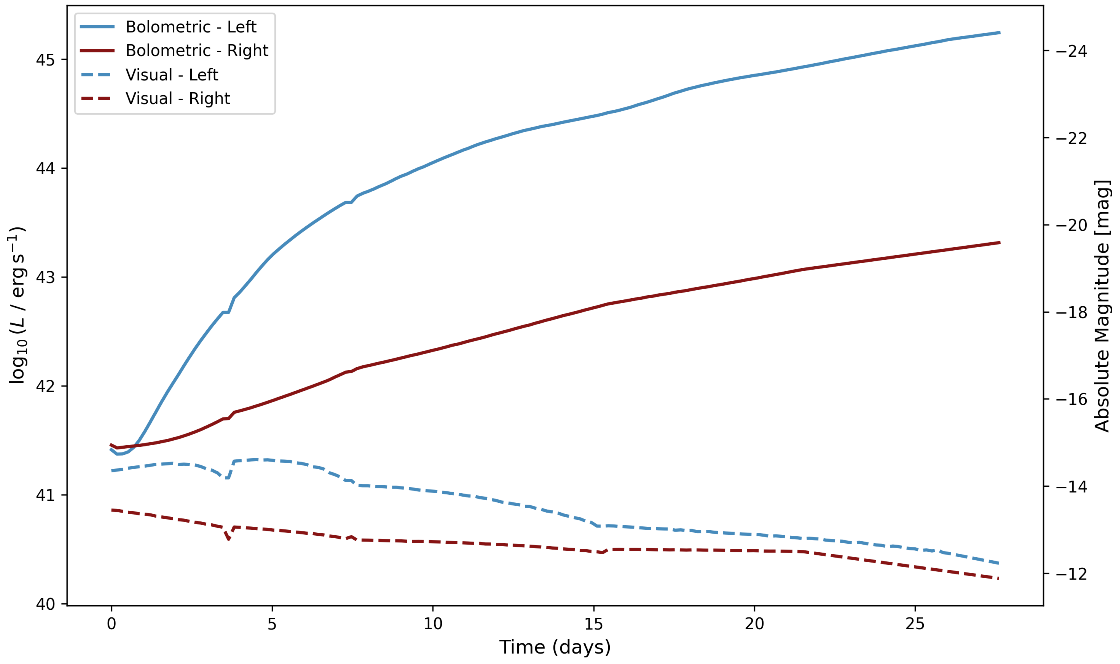

Figure 3.23: Light curves for the $R = 10^3\ R_g$, $M_\bullet = 10^8\ M_\odot$ scenario. Solid lines represent the bolometric luminosity, while dashed lines show the visual luminosity. Blue and red curves correspond to the left and right sides of the ejecta (from the observer's perspective), respectively. The right vertical axis indicates the absolute bolometric magnitude.

The most prominent feature is the stark asymmetry between the left (blue) and right (red) sides. The left side exhibits a significantly higher luminosity, reaching a peak that is approximately two orders of magnitude higher than that on the right side. This is a direct consequence of the relativistic Doppler beaming effect described in Section 3.5.2.

According to Equation (3.3), the flux amplification is proportional to D^4. The material on the left side of the orbit is moving towards the observer ($\cos\theta \approx 1$) at relativistic speeds, which maximizes the Doppler factor D from Equation (3.1), blue-shifting the emission and strongly amplifying the observed flux. In contrast, the right side recedes ($\cos\theta \approx -1$), leading to a minimized Doppler factor D, a corresponding red-shift, and severe dimming of the signal.

Scenario B: $R = 10^3\ R_g$, $M_\bullet = 10^9\ M_\odot$

In Figure 3.24, we present the results for a more massive SMBH ($M_\bullet = 10^9\ M_\odot$) at the same orbital distance ($R = 10^3\ R_g$).

Increasing the mass of the central body by an order of magnitude fundamentally alters the temporal evolution of the event. The most striking difference is the extreme compression

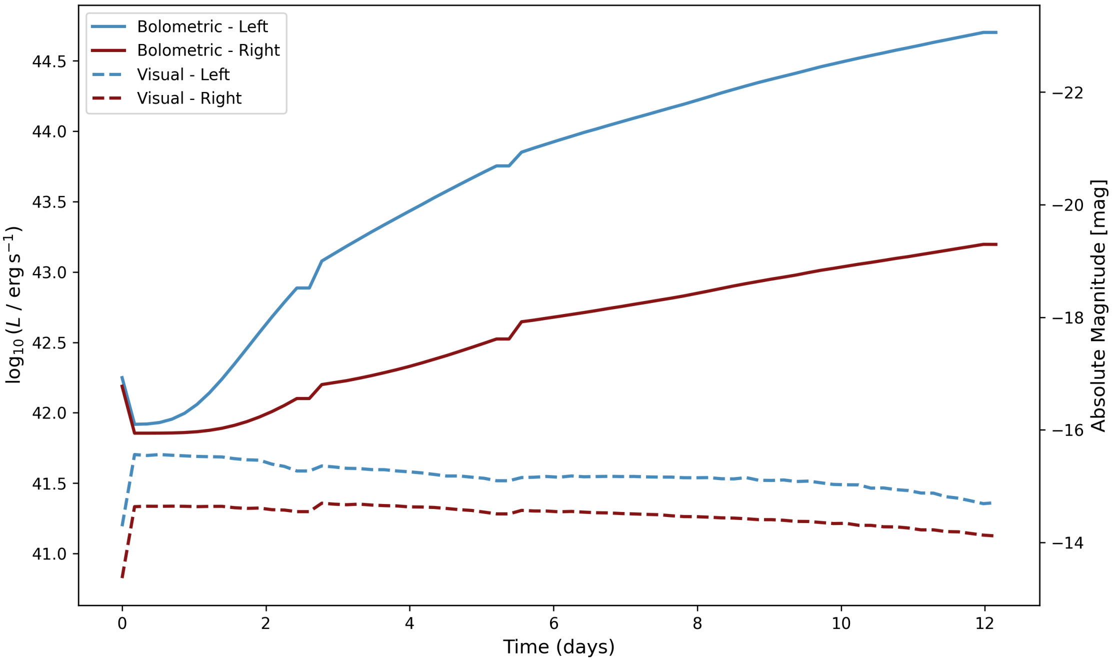

Figure 3.24: Light curves for the $R = 10^3\ R_g$, $M_\bullet = 10^9\ M_\odot$ scenario, displaying a significantly compressed time scale compared to Scenario A.

of the time scale. While the $10^8\ M_\odot$ case evolves over nearly 30 days, this scenario unfolds in approximately 12 days. The stronger gravitational field dictates higher orbital velocities and faster dynamical evolution of the shocked material.

Scenario C: $R = 10^4\ R_g$, $M_\bullet = 10^8\ M_\odot$

Figure 3.25 illustrates the scenario in which the SN explodes further away from the SMBH ($R = 10^4\ R_g$), but with a lower mass ($10^8\ M_\odot$).

As expected, increasing the distance from the SMBH mitigates the extreme relativistic effects. The temporal scale is significantly extended, and the light curve develops over roughly 80 days. Moreover, the gap between the left and right luminosities, while still present due to orbital motion, is narrower compared to the $R = 10^3\ R_g$ case. The lower orbital velocity at this larger radius results in a smaller value of β, leading to a much less pronounced Doppler beaming effect as predicted by Equation (3.1).

3.6.2 Comparative Analysis and Physical Interpretation

To fully grasp the dependencies on the SMBH parameters, Figure 3.26 provides a direct comparison of all three scenarios.

The Role of SMBH Mass and Distance

The distance R, on the other hand, strongly dictates the magnitude of the relativistic asymmetry. Closer to the SMBH, where the orbital velocity approaches the speed of

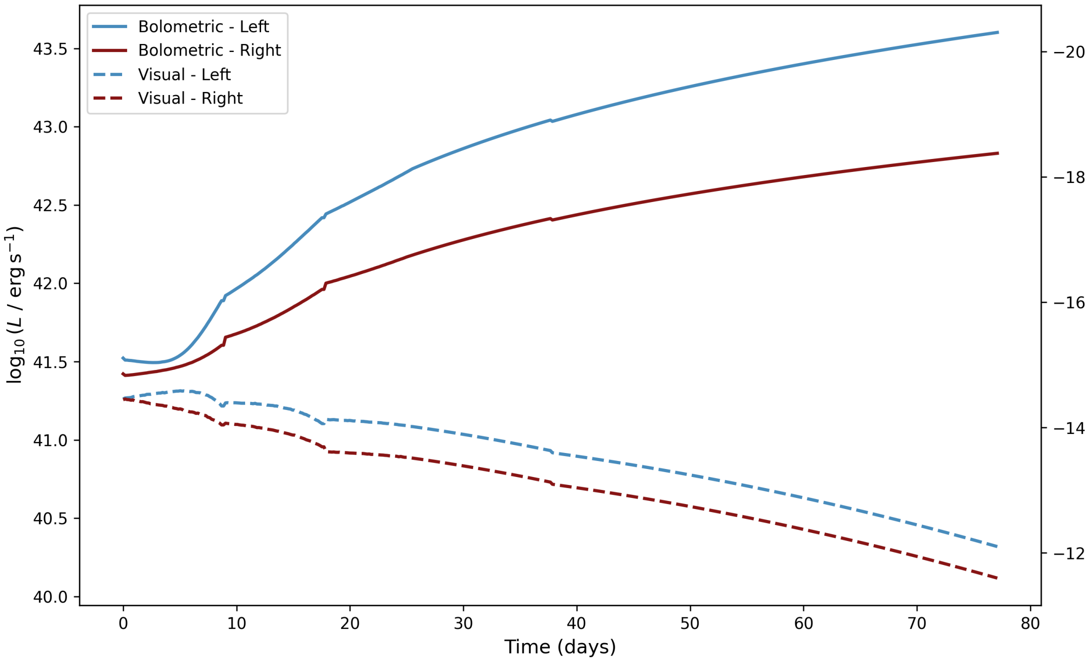

Figure 3.25: Light curves for the $R = 10^4\ R_\mathrm{g}$, $M_\bullet = 10^8\,M_\odot$ scenario. Note the extended time scale and reduced left-right asymmetry.

light ($\beta \longrightarrow 1$), the Doppler factor D from Equation (3.1) diverges heavily between the two sides, creating a massive disparity in luminosity (Equation (3.3)) for the approaching side compared to the receding side. Moving further out ($R = 10^4\ R_\mathrm{g}$) ”flattens” the difference, as the orbital velocities are lower.

Bolometric vs. Visual Luminosity: The Reprocessing Effect

In all examined models, a fundamental characteristic is the immense difference between the bolometric (solid lines) and visual (dashed lines) luminosities. The visual luminosity is consistently several orders of magnitude lower than the total bolometric output. Furthermore, their temporal trends differ: while the bolometric luminosity generally climbs over time as the shock sweeps up more material and dissipates kinetic energy, the visual luminosity exhibits a flatter or even declining trend.

This discrepancy highlights the physical state of the shocked gas. The interaction between the SN ejecta and the dense accretion disk environment generates extreme temperatures. Consequently, the vast majority of the radiant energy is not emitted in the optical (visual) spectrum. Instead, the emission peaks at much higher energies (X-ray or UV). As this high-energy radiation propagates through the surrounding, potentially dusty or dense layers of the non-shocked disk material, it is absorbed and re-emitted at longer wavelengths. This extensive ”reprocessing” leads to a scenario where the bulk of the observable energy eventually escapes in the infrared (IR) bands, leaving the visual band heavily depleted relative to the total energy budget.

Numerical Discontinuities and the *Embiggener* Tool

A critical examination of the light curves, particularly for the $M = 10^9\,M_\odot$ scenario (Fig. 3.24), reveals several sharp, non-physical jumps or discontinuities (e.g., around $t \approx 2.5$ and $t \approx 5.5$ days).

These sudden shifts in the luminosity values are not physical phenomena (such as sudden energy injections or phase transitions) but artifacts originating from the post-processing pipeline. Due to the immense computational cost of high-resolution hydrodynamic simulations, it is standard practice to output the full data snapshots only at specific, discrete intervals.

To bridge the temporal gaps between these snapshots for the purpose of continuous radiative transfer calculations (in *SEDONA*), a tool called *Embiggener* is employed. *Embiggener* acts as an interpolator, mapping the low-resolution or temporally sparse grid states onto a finer grid required for the Monte Carlo packet transport. The observed "teeth" or jumps in the light curves correspond exactly to the moments when *Embiggener* switches its base interpolation from one physical snapshot to the next. The slight inconsistencies in the density and internal energy fields between these discrete snapshots manifest as abrupt changes in the integrated luminosity. While these numerical artifacts affect the smoothness of the curves, they do not invalidate the overarching physical trends, the overall energy scale, or the clear left-right asymmetries observed in our results.

3.7 Photometric Evolution: AB Magnitudes

To directly connect the hydrodynamic evolution with observable signatures, we reconstructed the light curves using standard photometric filters. Figure 3.27 presents the evolution of AB magnitudes in the U, B, V, R, and I bands, compared to the total bolometric magnitude. This specific dataset corresponds to the $10^9\,M_\odot$ model at a radial distance of $10^3\,R_\mathrm{g}$, viewed from the perspective of a left-oriented observer.

3.7.1 Mathematical Formulation of AB Magnitudes

To quantify the observable photometric signatures and compare the bolometric luminosity with specific filter bands, the radiative output must be converted into the standard AB magnitude system. Following the methodology for radiation transfer post-processing of hydrodynamic models as detailed by Kurfürst et al. (2026), the AB magnitude in a specific frequency filter band b at a given time t and viewing angle θ (in the calculations represented in Fig. 3.27, $\theta = \pi/2$) is calculated as

$$M_\mathrm{AB}(t,\theta,b) = -2.5\log_{10}\left[\frac{\int T_b(\nu)\nu^{-1} f_\nu(t,\theta)\,\mathrm{d}\nu}{\int T_b(\nu)\nu^{-1}\,\mathrm{d}\nu}\right] - 48.60. \tag{3.7}$$

In this expression, $T_b(\nu)$ represents the frequency-dependent transmission function for the given filter band. The weighting factor ν^{-1} is included to account for the photon energy-counting response typical for CCD detectors (Kurfürst et al., 2026; Blanton and Roweis, 2007). The variable f_ν denotes the monochromatic spectral flux density, scaled to a standard reference distance of $d = 10\,\mathrm{pc}$. This approach allows for a consistent comparison between our numerical results and the observed characteristics of strongly interacting SNe.

Applying this formulation to the simulated spectral energy distribution allows us to properly isolate the flux captured by the ultraviolet bands, as well as the U, B, V, R, and I visual filters, and directly contrast it with the total integrated bolometric output. The entire calculation and convolution process was performed using the dedicated light-curve calculation tool implemented within the *SEDONA* code.

3.7.2 UV Dominance and Bolometric Discrepancy

The most prominent feature of the photometric data is the substantial difference between the bolometric magnitude and the visual band magnitudes. This discrepancy is primarily driven by the extremely high temperatures within the interaction zone. Due to these extreme thermal conditions and the relatively short duration of the simulated phase, the spectral energy distribution remains heavily dominated by ultraviolet (UV) bands throughout the entire simulation. Because most of the radiative flux peaks in the UV regime—well outside the range fully captured by the standard visual filters—the bolometric luminosity is orders of magnitude higher (brighter) than the flux recorded in the U, B, V, R, or I bands alone.

3.7.3 Infrared Contribution

Furthermore, the bolometric curve is likely amplified by emission in the infrared (IR) bands. While our plotted AB magnitudes include the I-band filter, the true bolometric calculation encompasses a much wider range of wavelengths, particularly extending deep into the IR. The dense dusty environment of the nuclear accretion disk acts as an efficient reprocessing medium, converting high-energy shock emission into thermal IR radiation. Since these deep IR bands are not represented in the plotted AB magnitudes, their contribution further widens the observed gap between the visual filters and the total bolometric output.

3.7.4 Long-term Evolution and Future Work

The current simulation tracks the SNR expansion for approximately 12 days, capturing the early, violently hot interaction phase. A critical question remains as to how these photometric profiles would evolve beyond this 12-day window.

As the remnant continues to expand and the shock-heated gas gradually cools, the peak of the emission is expected to shift progressively from the UV to the optical and, eventually, the infrared bands. Tracking this spectral evolution over longer timescales (e.g., several months to years) would likely show the visual magnitudes narrowing the gap with the bolometric curve. Investigating this long-term cooling phase and the corresponding shifts in the observable light curves stands as an important objective for future modeling efforts.

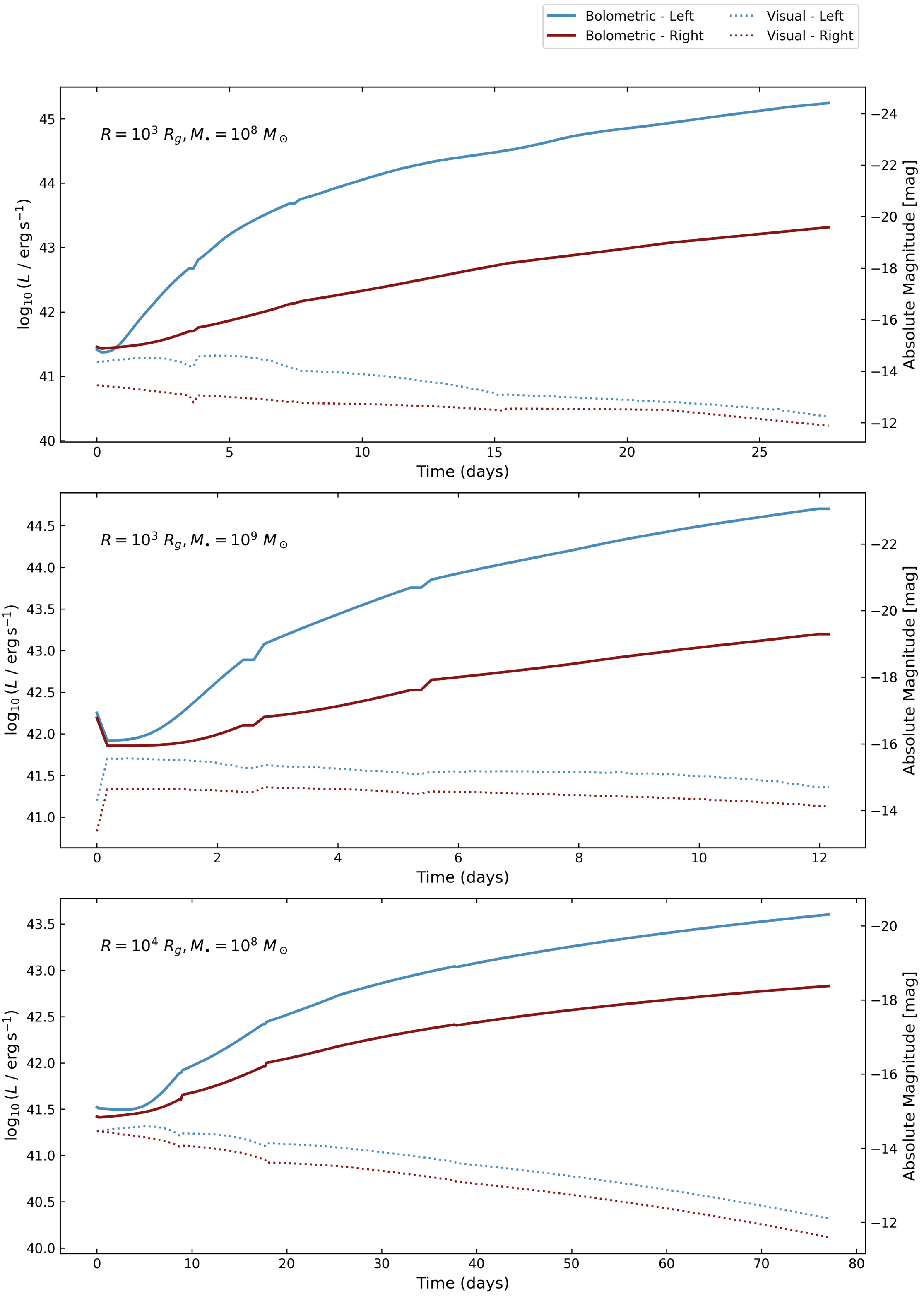

Figure 3.26: A comparative overview of the bolometric and visual light curves for all three simulated scenarios: $R = 10^3\ R_\mathrm{g}$, $M_\bullet = 10^8\,M_\odot$ (top panel), $R = 10^3\ R_\mathrm{g}$, $M_\bullet = 10^9\,M_\odot$ (middle panel), and $R = 10^4\ R_\mathrm{g}$, $M_\bullet = 10^8\,M_\odot$ (bottom panel).

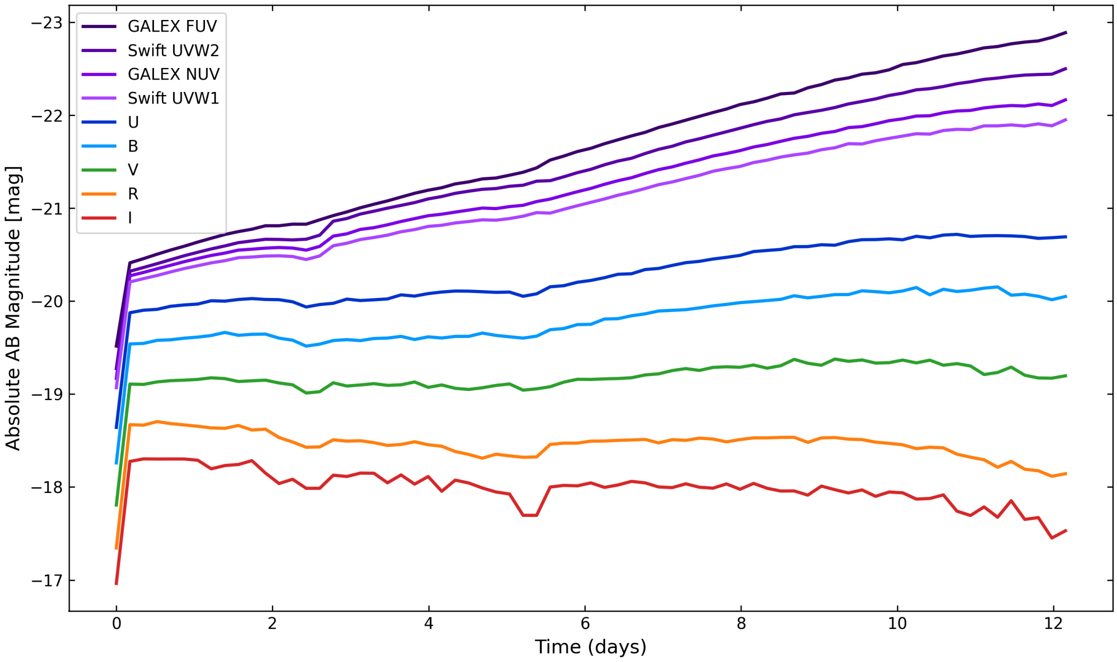

Figure 3.27: Evolution of the AB magnitudes in the ultraviolet and standard visual filters (U, B, V, R, and I) for the $R = 10^3\,R_\mathrm{g}$, $M_\bullet = 10^9\,M_\odot$ model in pericenter, calculated for the left-oriented observer's perspective. The clear dominance of the UV bands highlights that the bulk of the emitted energy falls outside the standard optical range, indicating that the total bolometric luminosity is significantly higher than the flux captured by the visual filters alone.

Discussion

The numerical simulations presented in this work provide a comprehensive overview of how the extreme gravitational and hydrodynamic environment of an AGN accretion disk shapes the evolution of SNRs. However, several physical and numerical factors must be taken into account when interpreting these results.

Thermodynamic Simplifications and Radiation

The models presented here are primarily adiabatic, utilizing an ideal gas equation of state with a constant adiabatic index of $\gamma = 5/3$. Although this approach effectively captures the initial shock dynamics and mechanical interaction with the disk, the omission of radiative cooling represents a significant simplification. In dense environments of an accretion disk, radiative losses are expected to be substantial, potentially leading to faster shock deceleration and earlier fragmentation of the remnant.

Integrating full radiation hydrodynamics would undoubtedly refine the accuracy of the shock's thermal evolution. However, implementing radiation in these models poses significant computational challenges, particularly with respect to the expansion of the computational domain. As the shock front moves across the grid, a larger domain is required to track its progress; however, the computational cost of radiation solvers scales steeply with grid size, making long-term radiative simulations prohibitively expensive within the scope of this study.

Temporal Evolution and Pericenter Dynamics

This study focused on the initial phases of the SN explosion, capturing the first few months of expansion. Modeling longer time intervals would likely reveal further interesting phenomena, such as the complete mixing of the ejecta with the disk material or the eventual fallback of gas onto the SMBH. This is particularly relevant for the pericenter models, where the interaction is exceptionally violent due to the high orbital velocities. In these cases, the rapid lateral drift caused by the progenitor's inherited momentum leads to the remnant exiting the computational domain relatively quickly, limiting our observation to the early-stage morphology.

Numerical Challenges and SMBH Artifacts

A known limitation in the current numerical setup involves the treatment of the central SMBH. In the *Castro* code, it is non-trivial to place a point mass outside or at the very edge of the active computational domain without introducing numerical artifacts. Consequently, the high-gravity region near the SMBH can exhibit small-scale fluctuations or instabilities in the density and pressure fields. Although these artifacts remain localized and do not significantly alter the global evolution of the SNR shock at larger radii, they represent a numerical constraint that could be addressed in future work through the use of alternative boundary conditions or specialized gravity solvers.

Physical Implications of Light Curve Profiles

The reconstructed light curves provide important insight into the physical mechanisms that govern the observables. The distinct shapes of the curves directly map the asynchronous shock breakout within the stratified medium of the disk. The steepness of the rise time and the duration of the peak are determined by the rate at which the shock front processes the dense ambient gas. However, our analytical light curve reconstruction relies on the optically thin approximation, which acts as a fundamental simplification.

In a fully coupled radiation hydrodynamic regime, the high optical depth of the unshocked accretion disk would actively reprocess the escaping radiation. This reprocessing would likely lead to a smoothing of the sharpest peaks, extending the rise time and causing a substantial wavelength shift, where the initial X-ray and UV photons are re-emitted in the infrared bands.

Additionally, the sparse temporal resolution of the physical data snapshots requires interpolation via the Embiggener tool. Although this introduces minor numerical discontinuities or ‘teeth’ in the curves (e.g., in Figure 3.24), it does not alter the underlying physical trends, the total energy scale, or the clear left-right asymmetries that dominate the observable profile.

Scope and Future Directions

It is important to note that this thesis aimed to provide a broad perspective on the problem rather than focusing on a single, specific astrophysical event. The parameter space involving SNe in an AGN is vast, including variations in disk viscosity, magnetic fields, and a wider range of eccentricities. Covering every permutation of these variables within a single bachelor’s thesis is not feasible.

By exploring a variety of SMBH masses (10^8 and $10^9\,M_\odot$) and radial distances (10^3 to $10^5\,R_\mathrm{g}$), this work serves as a foundational overview of the dominant physical regimes. The findings highlight that orbital phase and distance are primary drivers of the morphology of the SNR, providing a framework for more detailed, case-specific studies in the future.

Comparison with Analytical Models (She et al., 2025)

Our numerical results extend the analytical framework established by She et al. (2025), who investigated SN asymmetry in AGN disks induced by migration acceleration and pressure gradients. While their study assumes relatively low velocities between the progenitor and the disk, our simulations explore extreme kinematic regimes at $10^3\,R_\mathrm{g}$, where orbital velocities reach 6×10^9 cm/s.

In this high-speed limit, dynamic shear and ram pressure become the dominant drivers of anisotropy, transforming the elliptical cavities predicted by She et al. (2025) into highly distorted remnants. Furthermore, our light curve analysis identifies relativistic Doppler beaming as the primary source of flux asymmetry. This contrasts with the density-driven luminosity discrepancies in their model, demonstrating that inherited orbital momentum can overwhelm local environmental gradients during the expansion phase.

Conclusions

This thesis investigated the hydrodynamic evolution of SNRs in the extreme environments of AGN. By employing the Castro code to perform 2D Cartesian simulations with a resolution of 2048×2048 cells, we modeled the explosion of a $15\,M_\odot$ progenitor star in the vicinity of SMBHs with masses ranging from $4 \times 10^6\,M_\odot$ to $10^9\,M_\odot$. The primary focus was to determine how the orbital dynamics of the progenitor, specifically its velocity and position on an elliptical orbit with an eccentricity of $e = 0.6$, influence the resulting morphology and physical properties of the shock wave.

The results of this study lead to several significant conclusions:

- **Dominance of orbital momentum:** The inherited orbital velocity of the progenitor is a critical factor in determining the morphology of the SNR. In models near the pericenter of a $10^9\,M_\odot$ SMBH, where orbital velocities reach approximately $6 \times 10^9\,\mathrm{cm/s}$, the expansion of the SN is almost entirely overwhelmed by orbital motion. This leads to extreme shearing and a comet-like deformation of the remnant.
- **Radial scaling of distortion:** The distortive influence of the SMBH environment follows a clear radial dependency. At distances of $10^5\,R_\mathrm{g}$, the SNR retains high degrees of spherical symmetry, as the tidal forces and orbital shear are minimized. In contrast, at $10^3\,R_\mathrm{g}$, the vertical density gradient of the accretion disk and the Keplerian rotation cause the SNR to evolve into an asymmetric "hour-glass" shape.
- **Apocenter vs. pericenter evolution:** Comparing explosions at different orbital phases revealed that the apocenter provides a relatively more stable environment for SNR expansion due to lower orbital velocities. This allows the shock to be tracked within the computational domain for longer durations compared to pericenter models, where the remnant quickly exits the domain due to high lateral drift.
- **Thermodynamic signatures:** The interaction between the SN shock and the dense, high-pressure disk medium produces extreme temperatures exceeding $10^9\,\mathrm{K}$. Such conditions suggest that these events would be observable as transient, high-energy X-ray sources.
- **Characteristic light curve profiles:** The analytical reconstruction of synthetic light curves revealed that the temporal evolution of the radiant energy is strongly shaped by the progenitor's velocity vector. The light curve profiles are highly asymmetrical due to Doppler beaming: the approaching side of the orbit produces a steep rise time and a bright peak, while the receding side produces a flat, subdued profile. The overall shape of the curves—ranging from narrow, sharply decaying peaks near the

pericenter to broad plateaus at larger radii—serves as a primary diagnostic tool for the dynamical state of the SN.

In summary, this thesis demonstrates that the “stationary” assumption for SNe in galactic nuclei is insufficient when the progenitor resides on an eccentric orbit. The orbital history of the star is effectively “imprinted” onto the remnant’s morphology. These findings emphasize that any comprehensive model of feedback or observational transients in AGN must account for the velocity vector of the progenitor.

Appendix A

Hydrodynamics and Basic Equations

A.1 Cylindrical Polar Coordinates

A.1.1 Coordinate Transformation and Basis Vectors

Taking into account the cylindrical symmetry of the system under study, it is advantageous to use equations in cylindrical polar coordinates (R, ϕ, z) (Binney and Tremaine (2008)). This coordinate system is defined by the radial distance R from the z-axis, the azimuthal angle ϕ measured from the x-axis, and the vertical height z. The formal transformation rules and the properties of the cylindrical basis are detailed in Arfken et al. (2012).

The transformation between the Cartesian coordinates (x, y, z) and the cylindrical coordinates (R, ϕ, z) is given by:

$$x = R\cos\phi, \quad y = R\sin\phi, \quad z = z. \tag{A.1}$$

The unit basis vectors in this system are $\hat{\boldsymbol{e}}_R, \hat{\boldsymbol{e}}_\phi$, and $\hat{\boldsymbol{e}}_z$. In cylindrical coordinates, the directions of $\hat{\boldsymbol{e}}_R$ and $\hat{\boldsymbol{e}}_\phi$ change as the azimuthal angle ϕ varies. We can express these basis vectors in terms of Cartesian unit vectors $(\hat{\boldsymbol{x}}, \hat{\boldsymbol{y}}, \hat{\boldsymbol{z}})$ as follows:

$$\hat{\boldsymbol{e}}_R = \cos\phi\,\hat{\boldsymbol{x}} + \sin\phi\,\hat{\boldsymbol{y}}, \quad \hat{\boldsymbol{e}}_\phi = -\sin\phi\,\hat{\boldsymbol{x}} + \cos\phi\,\hat{\boldsymbol{y}}. \tag{A.2}$$

By differentiating these expressions with respect to ϕ, we find the fundamental spatial relationships:

$$\frac{\partial \hat{\boldsymbol{e}}_R}{\partial \phi} = \hat{\boldsymbol{e}}_\phi, \quad \frac{\partial \hat{\boldsymbol{e}}_\phi}{\partial \phi} = -\hat{\boldsymbol{e}}_R. \tag{A.3}$$

A.1.2 Differential Operators

To accurately enforce the conservation laws of hydrodynamics in cylindrical geometry, we define the fundamental differential operators for scalar and vector fields. These operators account for the radial curvature, enabling precise spatial derivatives (Arfken et al. (2012); Frank et al. (2002)) in the cylindrical coordinate system.

The gradient of a scalar field $f(R,\phi,z)$, which gives the direction and magnitude of the steepest ascent of a physical quantity, is defined as

$$\nabla f = \frac{\partial f}{\partial R}\hat{\boldsymbol{e}}_R + \frac{1}{R}\frac{\partial f}{\partial \phi}\hat{\boldsymbol{e}}_\phi + \frac{\partial f}{\partial z}\hat{\boldsymbol{e}}_z, \tag{A.4}$$

where the factor $1/R$ in the azimuthal component converts the angular variation into the physical distance.

The divergence of a vector field $\boldsymbol{A} = A_R\hat{\boldsymbol{e}}_R + A_\phi\hat{\boldsymbol{e}}_\phi + A_z\hat{\boldsymbol{e}}_z$, which is essential for describing the net flux of a quantity out of an infinitesimal volume, is

$$\nabla\cdot\boldsymbol{A} = \frac{1}{R}\frac{\partial(RA_R)}{\partial R} + \frac{1}{R}\frac{\partial A_\phi}{\partial\phi} + \frac{\partial A_z}{\partial z}. \tag{A.5}$$

The radial term includes a geometric correction reflecting the increased area of radial shells moving away from the z-axis.

To capture flow rotation, we require the curl operator, which is defined as

$$\nabla\times\boldsymbol{A} = \left(\frac{1}{R}\frac{\partial A_z}{\partial\phi} - \frac{\partial A_R}{\partial z}\right)\hat{\boldsymbol{e}}_R + \left(\frac{\partial A_R}{\partial z} - \frac{\partial A_z}{\partial R}\right)\hat{\boldsymbol{e}}_\phi + \frac{1}{R}\left[\frac{\partial(RA_\phi)}{\partial R} - \frac{\partial A_R}{\partial\phi}\right]\hat{\boldsymbol{e}}_z. \tag{A.6}$$

The Laplacian Δf, crucial for pressure-Poisson equations and thermal diffusion, takes the form

$$\Delta f = \frac{1}{R}\frac{\partial}{\partial R}\left(R\frac{\partial f}{\partial R}\right) + \frac{1}{R^2}\frac{\partial^2 f}{\partial\phi^2} + \frac{\partial^2 f}{\partial z^2}. \tag{A.7}$$

Together, these operators provide the complete mathematical foundation required for solving hydrodynamic equations in a three-dimensional cylindrical volume.

A.1.3 Velocity and Acceleration in Cylindrical Coordinates

In the context of fluid dynamics, we must account for the fact that the basis vectors themselves change over time as the fluid moves.

The position vector is $\boldsymbol{r} = R\hat{\boldsymbol{e}}_R + z\hat{\boldsymbol{z}}$. Differentiating $\boldsymbol{r}$ with respect to time t (using the product rule) yields the velocity vector $\boldsymbol{v}$:

$$\boldsymbol{v} = \frac{\mathrm{d}}{\mathrm{d}t}(R\hat{\boldsymbol{e}}_R + z\hat{\boldsymbol{z}}) = \dot{R}\hat{\boldsymbol{e}}_R + R\dot{\hat{\boldsymbol{e}}}_R + \dot{z}\hat{\boldsymbol{z}}. \tag{A.8}$$

Using the chain rule, $\dot{\hat{\boldsymbol{e}}}_R = (\partial\hat{\boldsymbol{e}}_R/\partial\phi)\,\mathrm{d}\phi/\mathrm{d}t = \dot{\phi}\hat{\boldsymbol{e}}_\phi$. Substituting this into Equation (A.8), we get

$$\boldsymbol{v} = \dot{R}\hat{\boldsymbol{e}}_R + (R\dot{\phi})\hat{\boldsymbol{e}}_\phi + \dot{z}\hat{\boldsymbol{z}} = v_R\hat{\boldsymbol{e}}_R + v_\phi\hat{\boldsymbol{e}}_\phi + v_z\hat{\boldsymbol{z}}. \tag{A.9}$$

Differentiating the velocity vector $\boldsymbol{v}$ with respect to time t gives acceleration $\boldsymbol{a}$. This step reveals important terms that are vital for the hydrodynamic equations, specifically those describing non-inertial effects (Kurfürst, 2015):

$$\boldsymbol{a} = \frac{\mathrm{d}}{\mathrm{d}t}[\dot{R}\hat{\boldsymbol{e}}_R + (R\dot{\phi})\hat{\boldsymbol{e}}_\phi + \dot{z}\hat{\boldsymbol{z}}]. \tag{A.10}$$

Expanding Equation (A.10) using the product rule and substituting the time derivatives of the basis vectors ($\dot{\hat{\boldsymbol{e}}}_R = \dot{\phi}\hat{\boldsymbol{e}}_\phi$ and $\dot{\hat{\boldsymbol{e}}}_\phi = -\dot{\phi}\hat{\boldsymbol{e}}_R$) gives

$$\boldsymbol{a} = (\ddot{R} - R\dot{\phi}^2)\hat{\boldsymbol{e}}_R + (R\ddot{\phi} + 2\dot{R}\dot{\phi})\hat{\boldsymbol{e}}_\phi + \ddot{z}\hat{\boldsymbol{z}}. \tag{A.11}$$

In fluid dynamics, these components are typically written using the velocity components (v_R, v_ϕ, v_z):

$$a_R = \frac{\mathrm{d}v_R}{\mathrm{d}t} - \frac{v_\phi^2}{R}, \qquad a_\phi = \frac{\mathrm{d}v_\phi}{\mathrm{d}t} + \frac{v_R v_\phi}{R}. \tag{A.12}$$

Here, a_R is the radial acceleration, including the centrifugal term, and a_ϕ is the azimuthal acceleration, including the Coriolis term.

A.2 Cauchy Stress Tensor

The state of stress in the fluid is described by the symmetric Cauchy stress tensor σ_{ij}, which accounts for both the isotropic pressure and the viscous dissipative forces. For a compressible Newtonian fluid, it is defined as (Landau and Lifshitz, 1987)

$$\sigma_{ij} = -p\delta_{ij} + \tau_{ij}. \tag{A.13}$$

Here, δ_{ij} is the Kronecker delta, p is the thermodynamic pressure, and τ_{ij} is the viscous stress tensor. These components incorporate the specific geometry of the flow, which is essential for modeling dense circumstellar or galactic disks (Kurfürst et al., 2018). For a Newtonian fluid, it is expressed as

$$\tau_{ij} = \eta\left(\frac{\partial v_i}{\partial x_j} + \frac{\partial v_j}{\partial x_i}\right) + \left(\zeta - \frac{2}{3}\eta\right)\frac{\partial v_k}{\partial x_k}\delta_{ij}, \tag{A.14}$$

where η is the dynamic shear viscosity, and ζ is the bulk (volume) viscosity. The relationship between the dynamic viscosity and the kinematic viscosity ν is given by:

$$\nu = \frac{\eta}{\rho}. \tag{A.15}$$

A.2.1 Cauchy Stress Tensor in Cylindrical Polar Coordinates

In cylindrical coordinates (R, ϕ, z), the components of the Cauchy stress tensor take the following form, incorporating the specific geometry of the galactic disk:

$$\sigma_{RR} = -p + 2\eta\left(\frac{\partial v_R}{\partial R}\right) + \left(\zeta - \frac{2}{3}\eta\right)\boldsymbol{\nabla}\cdot\boldsymbol{v}, \tag{A.16}$$

$$\sigma_{\phi\phi} = -p + 2\eta\left(\frac{1}{R}\frac{\partial v_\phi}{\partial \phi} + \frac{v_R}{R}\right) + \left(\zeta - \frac{2}{3}\eta\right)\boldsymbol{\nabla}\cdot\boldsymbol{v}, \tag{A.17}$$

$$\sigma_{zz} = -p + 2\eta\left(\frac{\partial v_z}{\partial z}\right) + \left(\zeta - \frac{2}{3}\eta\right)\boldsymbol{\nabla}\cdot\boldsymbol{v}. \tag{A.18}$$

The off-diagonal (shear) components, which represent internal friction between fluid layers, are

$$\sigma_{R\phi} = \eta \left[R \frac{\partial}{\partial R} \left(\frac{v_\phi}{R} \right) + \frac{1}{R} \frac{\partial v_R}{\partial \phi} \right], \tag{A.19}$$

$$\sigma_{Rz} = \eta \left(\frac{\partial v_z}{\partial R} + \frac{\partial v_R}{\partial z} \right), \tag{A.20}$$

$$\sigma_{\phi z} = \eta \left(\frac{1}{R} \frac{\partial v_z}{\partial \phi} + \frac{\partial v_\phi}{\partial z} \right). \tag{A.21}$$

The divergence of the velocity field in cylindrical coordinates, as defined previously in Equation (A.5), is

$$\nabla \cdot \boldsymbol{v} = \frac{1}{R} \frac{\partial (R v_R)}{\partial R} + \frac{1}{R} \frac{\partial v_\phi}{\partial \phi} + \frac{\partial v_z}{\partial z}. \tag{A.22}$$

A.3 Hydrodynamics

The fundamental principles of hydrodynamics play a key role in galactic dynamics, both because hydrodynamic and stellar systems behave in a similar way and because gas-dynamics is central to galaxy formation and shock wave propagation (Binney and Tremaine, 2008). This chapter reviews the key hydrodynamic concepts employed herein.

A.4 Conservation Laws

A.4.1 Continuity Equation (Conservation of Mass)

In the fluid dynamics of galactic disks, the conservation of mass serves as the fundamental basis upon which all subsequent derivations are constructed. To obtain the governing equation, we consider an arbitrary fixed control volume V in space, bounded by a closed surface S. The total mass $M(t)$ of the fluid within this volume is expressed as the volume integral of the mass density $\rho(\boldsymbol{x}, t)$:

$$M(t) = \int_V \rho(\boldsymbol{x}, t) \, \mathrm{d}^3\boldsymbol{x}. \tag{A.23}$$

The temporal rate of change of mass inside V balances the net mass flux across the bounding surface S. With $\boldsymbol{v}(\boldsymbol{x}, t)$ representing the velocity field, the mass flowing out through an infinitesimal surface element $\mathrm{d}\boldsymbol{S}$ per unit time is $\rho \boldsymbol{v} \cdot \mathrm{d}^2\boldsymbol{S}$. Conservation thus mandates:

$$\frac{\mathrm{d}M}{\mathrm{d}t} = -\oint_S \rho \boldsymbol{v} \cdot \mathrm{d}^2\boldsymbol{S}. \tag{A.24}$$

By substituting the integral expression for M into Equation (*A.24*) and applying Gauss's theorem — which states $\int_V \nabla \cdot \boldsymbol{F} \, \mathrm{d}^3\boldsymbol{x} = \oint_S \boldsymbol{F} \cdot \mathrm{d}^2\boldsymbol{S}$ for any vector field $\boldsymbol{F}$—to convert the surface integral into a volume integral, we obtain

$$\int_V \left[\frac{\partial \rho}{\partial t} + \nabla \cdot (\rho \boldsymbol{v}) \right] \mathrm{d}^3\boldsymbol{x} = 0. \tag{A.25}$$

Since this relation must hold for any arbitrary volume V, the integrand itself must be equal to zero. This leads to the continuity equation in differential form:

$$\frac{\partial \rho}{\partial t} + \boldsymbol{\nabla} \cdot (\rho \boldsymbol{v}) = 0. \tag{A.26}$$

Source and Sink Terms

Astrophysical environments, such as the initial phase of a SN explosion or ionized media with significant recombination, may add local mass sources or sinks to the system. In such cases, the continuity equation generalizes to

$$\frac{\partial \rho}{\partial t} + \boldsymbol{\nabla} \cdot (\rho \boldsymbol{v}) = \beta, \tag{A.27}$$

where β represents the volumetric mass production or destruction rate (positive for sources and negative for sinks). However, in this thesis, specifically when modeling the expansion of the shock wave after the initial energy injection, we assume the ISM is non-reacting and that the total mass is conserved. Therefore, we can set $\beta = 0$ (F02).

A.4.2 Navier–Stokes Equation (Conservation of Momentum)

The conservation of momentum extends Newton's second law to a fluid continuum. It states that the rate of change of momentum of a fluid element is equal to the sum of the forces acting upon it. In Eulerian coordinates, this is expressed as

$$\rho \frac{\mathrm{D}\boldsymbol{v}}{\mathrm{D}t} = \boldsymbol{f}_{\mathrm{ext}} + \boldsymbol{f}_{\mathrm{int}}, \tag{A.28}$$

where ρ is the fluid density, $\boldsymbol{v}$ is the velocity field, $\mathrm{D}/\mathrm{D}t$ is the material derivative, $\boldsymbol{f}_{\mathrm{ext}}$ represents external body forces (e.g., gravitation), and $\boldsymbol{f}_{\mathrm{int}}$ represents internal surface forces.

The material derivative $\mathrm{D}\boldsymbol{v}/\mathrm{D}t$ represents the acceleration of a fluid particle. Because the velocity field $\boldsymbol{v}(\boldsymbol{x}, t)$ depends on both position and time, the acceleration must be expanded into its local and advection components:

$$\frac{\mathrm{D}\boldsymbol{v}}{\mathrm{D}t} = \frac{\partial \boldsymbol{v}}{\partial t} + (\boldsymbol{v} \cdot \boldsymbol{\nabla})\boldsymbol{v}. \tag{A.29}$$

Here, $\partial \boldsymbol{v}/\partial t$ denotes local acceleration, while $(\boldsymbol{v} \cdot \boldsymbol{\nabla})\boldsymbol{v}$ represents the advection of momentum as the fluid moves through gradients in the velocity field.

Internal forces in a fluid arise from the interaction between adjacent fluid layers and are quantified by the divergence of the Cauchy stress tensor σ (Equation A.13), yielding a force per unit volume of $\nabla \cdot \sigma$. Substituting into the momentum balance (Equation A.28) gives the general form of the equations of motion for a viscous fluid, as derived in the classic work by Landau and Lifshitz (1987):

$$\rho \frac{\mathrm{D}\boldsymbol{v}}{\mathrm{D}t} = -\nabla p + \nabla \cdot \tau + \rho \boldsymbol{g}, \tag{A.30}$$

where $\boldsymbol{g}$ is the gravitational acceleration. For Newtonian fluids, which are characteristic of the ISM, the viscous tensor τ relates linearly to the rate of strain. For a compressible flow, the viscous tensor τ is given by Equation (A.14).

Inserting Equation (A.14) into the momentum equation (A.30) yields the full compressible Navier–Stokes equation:

$$\rho\left[\frac{\partial \boldsymbol{v}}{\partial t}+(\boldsymbol{v}\cdot\boldsymbol{\nabla})\boldsymbol{v}\right]=-\nabla p+\eta\nabla^2\boldsymbol{v}+\left(\zeta+\frac{1}{3}\eta\right)\nabla(\nabla\cdot\boldsymbol{v})+\rho\boldsymbol{g}. \tag{A.31}$$

In modeling SNRs within the dense environment of a galactic disk, where shock speeds greatly exceed the local escape velocity ($v_{\mathrm{sw}} \gg v_{\mathrm{esc}}$), the external gravitational field $\boldsymbol{g}$ is neglected ($\rho\boldsymbol{g} \approx 0$) during the early and intermediate stages of expansion (Branch and Wheeler, 2017). Consequently, the Navier–Stokes equation (A.31) simplifies to its purely hydrodynamic form:

$$\rho\left[\frac{\partial \boldsymbol{v}}{\partial t}+(\boldsymbol{v}\cdot\boldsymbol{\nabla})\boldsymbol{v}\right]=-\nabla p+\eta\nabla^2\boldsymbol{v}+\left(\zeta+\frac{1}{3}\eta\right)\nabla(\nabla\cdot\boldsymbol{v}). \tag{A.32}$$

A.4.3 Conservation of Total Energy

The third main equation in hydrodynamics is the conservation of total energy. This comes from the first law of thermodynamics for moving fluids. For a SN explosion in the galactic disk, the total energy per unit volume E is the sum of the kinetic energy $K(\boldsymbol{x},t)=1/2(\rho v^2)$ and the internal (thermal) energy $U(\boldsymbol{x},t)=\rho\epsilon$:

$$E=\frac{1}{2}\rho v^2+\rho\epsilon, \tag{A.33}$$

where ϵ is the specific internal energy (internal energy per unit mass). While gravity can add potential energy, we ignore self-gravity and external fields, such as magnetic fields, to focus purely on hydrodynamic and thermodynamic evolution.

The evolution of kinetic energy is derived directly from the momentum equation (Newton's second law, Equation A.30), where gravitational forces are neglected. To obtain the rate of kinetic energy change, we take the dot product of this equation with the velocity vector $\boldsymbol{v}$:

$$\boldsymbol{v}\cdot\left(\rho\frac{\mathrm{D}\boldsymbol{v}}{\mathrm{D}t}\right)=\boldsymbol{v}\cdot(\nabla\cdot\sigma). \tag{A.34}$$

With the help of the identity $\boldsymbol{v}\cdot\mathrm{D}\boldsymbol{v}/\mathrm{D}t=\mathrm{D}/\mathrm{D}t(v^2/2)$, the left-hand side represents the material change in kinetic energy per unit volume. The right-hand side can be expanded using the tensor identity $\nabla\cdot(\boldsymbol{A}\cdot\boldsymbol{B})=\boldsymbol{A}\cdot(\nabla\cdot\boldsymbol{B})+\boldsymbol{B}:\nabla\boldsymbol{A}$:

$$\rho\frac{\mathrm{D}}{\mathrm{D}t}\left(\frac{1}{2}v^2\right)=\nabla\cdot(\boldsymbol{v}\cdot\sigma)-\sigma:\nabla\boldsymbol{v}, \tag{A.35}$$

where the colon (:) denotes the double-dot product between two second-rank tensors. Substituting the stress tensor decomposition as in Equation (A.13), the term $\sigma:\nabla\boldsymbol{v}$ becomes

$-p(\nabla\cdot\boldsymbol{v})+\Psi$, where $\Psi=\tau_{ij}(\partial v_i/\partial x_j)$ is the viscous dissipation function (Kundu et al., 2015). Thus:

$$\rho\frac{\mathrm{D}}{\mathrm{D}t}\left(\frac{1}{2}v^2\right)=\nabla\cdot(\boldsymbol{v}\cdot\sigma)+p(\nabla\cdot\boldsymbol{v})-\Psi. \tag{A.36}$$

Equation (A.36) shows that kinetic energy changes due to surface forces (stresses) but loses a portion to internal energy through pressure work and viscous friction.

The internal (thermal) energy ϵ (per unit mass) follows the first law of thermodynamics, which states that the change in internal energy equals the heat added to the system minus the work done by the system:

$$\rho\frac{\mathrm{D}\epsilon}{\mathrm{D}t}=\text{work of compression}+\text{viscous heating}-\text{heat flux}. \tag{A.37}$$

To understand the origin of heat flux, we must relate the internal energy ϵ to the entropy s. From Gibbs' relation, which combines the first and second laws for reversible processes, we have

$$T\,\mathrm{d}s=\mathrm{d}\epsilon+p\,\mathrm{d}\left(\frac{1}{\rho}\right)=\mathrm{d}\epsilon-\frac{p}{\rho^2}\mathrm{d}\rho. \tag{A.38}$$

By taking the material derivative $\mathrm{D}/\mathrm{D}t$ and multiplying by density ρ, we obtain the rate of change of internal energy in terms of entropy and compression:

$$\rho\frac{\mathrm{D}\epsilon}{\mathrm{D}t}=\rho T\frac{\mathrm{D}s}{\mathrm{D}t}+\frac{p}{\rho}\frac{\mathrm{D}\rho}{\mathrm{D}t}. \tag{A.39}$$

Using the continuity equation, $\mathrm{D}\rho/\mathrm{D}t=-\rho(\nabla\cdot\boldsymbol{v})$, the second term on the right side becomes $-p(\nabla\cdot\boldsymbol{v})$. Thus:

$$\rho\frac{\mathrm{D}\epsilon}{\mathrm{D}t}=\rho T\frac{\mathrm{D}s}{\mathrm{D}t}-p(\nabla\cdot\boldsymbol{v}). \tag{A.40}$$

For a fluid element, entropy changes due to heat exchange with the surroundings and internal irreversible processes (e.g., friction). This is expressed by the entropy balance equation,

$$\rho\frac{\mathrm{D}s}{\mathrm{D}t}=-\nabla\cdot\boldsymbol{s}_{\text{flux}}+\sigma_{\text{entropy}}, \tag{A.41}$$

where $\boldsymbol{s}_{\text{flux}}=\boldsymbol{q}/T$ is the entropy flux associated with heat flow, and $\sigma_{\text{entropy}}\geq 0$ is the entropy production. For a viscous, heat-conducting fluid, the heat generation must satisfy:

$$\rho T\frac{\mathrm{D}s}{\mathrm{D}t}=-\nabla\cdot\boldsymbol{q}+\Psi. \tag{A.42}$$

Substituting this into Equation (A.40), we get the internal (thermal) energy evolution that corresponds to Equation (A.37):

$$\rho\frac{\mathrm{D}\epsilon}{\mathrm{D}t}=-p(\nabla\cdot\boldsymbol{v})+\Psi-\nabla\cdot\boldsymbol{q}. \tag{A.43}$$

Here, the term $-p(\nabla\cdot\boldsymbol{v})$ refers to the work done by pressure (heating during compression), Ψ is the irreversible conversion of mechanical energy into heat (Kundu et al., 2015), and $\nabla\cdot\boldsymbol{q}$ represents the energy loss or gain due to heat conduction (Fourier's law).

To find the equation for the total energy E, we sum the kinetic energy rate (A.36) and the internal energy rate (A.43) as

$$\rho \frac{\mathrm{D}}{\mathrm{D}t}\left(\frac{1}{2}v^2 + \epsilon\right) = \nabla \cdot (\boldsymbol{v} \cdot \sigma) + p(\nabla \cdot \boldsymbol{v}) - \Psi - p(\nabla \cdot \boldsymbol{v}) + \Psi - \nabla \cdot \boldsymbol{q}. \tag{A.44}$$

We can see that the terms $p(\nabla \cdot \boldsymbol{v})$ and Ψ have opposite signs and cancel out. This cancelation matters physically: it represents the conversion of energy from mechanical to thermal form entirely within the system. This simplifies to

$$\rho \frac{\mathrm{D}}{\mathrm{D}t}\left(\frac{E}{\rho}\right) = \nabla \cdot (\boldsymbol{v} \cdot \sigma - \boldsymbol{q}). \tag{A.45}$$

We can use the continuity equation (A.26) to convert the material derivative to the conservative (Eulerian) form, which is the preferred formulation for modern Riemann-based numerical solvers (Toro, 2009; Almgren et al., 2010):

$$\frac{\partial E}{\partial t} + \nabla \cdot (E\boldsymbol{v}) = \nabla \cdot (\boldsymbol{v} \cdot \sigma - \boldsymbol{q}). \tag{A.46}$$

With one last adjustment, $\boldsymbol{v} \cdot \sigma = -p\boldsymbol{v} + \boldsymbol{v} \cdot \tau$, we get the final form used in numerical codes:

$$\frac{\partial E}{\partial t} + \nabla \cdot [(E + p)\boldsymbol{v}] = \nabla \cdot (\boldsymbol{v} \cdot \tau - \boldsymbol{q}). \tag{A.47}$$

A.5 Equation of State

The system of conservation laws derived in previous sections remains undetermined until a relation between the state variables is provided. The equation of state (EoS) provides the connection between pressure, density, and internal (thermal) energy, which reflects the physical nature of the gas in the galactic disk.

The relationship between internal energy and mechanical work is described by the first law of thermodynamics. For a unit mass, we can write it in the form:

$$\mathrm{d}\epsilon = \mathrm{d}q + \frac{p}{\rho^2}\mathrm{d}\rho, \tag{A.48}$$

where $\mathrm{d}q$ is the heat exchanged with the surroundings. In the context of the rapid expansion of SNRs, many processes can be viewed as adiabatic ($\mathrm{d}q = 0$). Under these conditions, the gas follows the polytropic relation $p/\rho^\gamma = \text{const.}$, where γ is the adiabatic index (or Poisson's ratio), defined as the ratio of specific heats (c_p/c_v).

In most interstellar environments, the gas is sufficiently dilute to be treated as an ideal gas. Its EoS relates pressure, density, and temperature as follows:

$$p = \frac{k_\mathrm{B}}{\mu m_\mathrm{u}}\rho T. \tag{A.49}$$

Here, k_B is the Boltzmann constant, m_u is the atomic mass unit, and μ is the mean molecular weight, which characterizes the chemical composition and ionization state of the gas. In the context of the ISM, this is often taken from the comprehensive models of Draine (2011):

$$\frac{1}{\mu} = \sum_i \frac{X_i}{A_i}(1 + n_{e,i}), \tag{A.50}$$

where X_i and A_i are the mass fraction and atomic mass of element i, respectively, and $n_{e,i}$ represents the free electrons per atom/ion.

For numerical simulations, it is necessary to express pressure directly in terms of density and internal energy (Almgren et al., 2010). For a calorically perfect gas, this relation can be derived from the fundamental definition of specific enthalpy and thermodynamic state relations. Specific enthalpy h combines specific internal energy ϵ with flow work as

$$h = \epsilon + p\mathcal{V}, \tag{A.51}$$

where the specific volume is $\mathcal{V} = 1/\rho$. For a calorically perfect gas, we assume that the specific heat capacities c_p and c_v are constants that are independent of temperature. Under these assumptions, we can express the specific internal energy ϵ and enthalpy h as

$$\epsilon = c_v T, \qquad h = c_p T. \tag{A.52}$$

By substituting the expressions from Equation (A.52) into the definition of enthalpy (A.51), we can isolate the term containing pressure:

$$\frac{p}{\rho} = (c_p - c_v)T. \tag{A.53}$$

By employing the previously defined adiabatic index $\gamma = c_p/c_v$, substituting the difference of specific heats yields

$$c_p - c_v = c_v(\gamma - 1). \tag{A.54}$$

Now we can substitute Equation (A.54) back into (A.53), replace the temperature with its energy-based equivalent ($T = \epsilon/c_v$), cancel c_v, and multiply by ρ to yield the caloric equation of state:

$$p = (\gamma - 1)\rho\epsilon. \tag{A.55}$$

This relation assumes a gas lacking internal degrees of freedom (e.g., molecular rotation or vibration), which is characteristic of the strong shock regime in the early adiabatic expansion phase of SNRs (Sedov, 1946; Branch and Wheeler, 2017).

The propagation of pressure disturbances through the medium can be represented by the speed of sound a. It acts as the fluid's "communication speed," determining how fast one part of the galactic disk reacts to an incoming SN blast wave. In general, $a^2 = \partial p/\partial\rho$.

The transition between the adiabatic and isothermal regimes depends on the radiative cooling rates of the plasma, detailed in Draine (2011).

1. **The Adiabatic Case:** Within the SN bubble, the gas is extremely hot and dilute. Here, the characteristic time for radiative cooling is much longer than the dynamical timescale of the expansion ($t_{\mathrm{cool}} \gg t_{\mathrm{dyn}}$). The energy remains trapped within the fluid element, and the sound speed is defined as

$$\left(a^2\right)_S = \frac{\gamma p}{\rho} = \frac{\gamma k_{\mathrm{B}} T}{\mu m_{\mathrm{u}}}. \tag{A.56}$$

2. **The Isothermal Case:** As the shock hits the dense, dusty galactic disk, radiative cooling becomes highly efficient ($t_{\mathrm{cool}} \ll t_{\mathrm{dyn}}$). The gas radiates away the heat generated by the shock almost instantaneously, maintaining a constant temperature T. In this limit, $\gamma \longrightarrow 1$, and the sound speed reduces to

$$\left(a^2\right)_T = \frac{p}{\rho} = \frac{k_{\mathrm{B}} T}{\mu m_{\mathrm{u}}}. \tag{A.57}$$

A.6 Gravitational Potential and Forces

In the extreme environment of the galactic center, gravity is the dominant force governing the equilibrium of the nuclear disk and the motion of the ISM. To maintain physical consistency within the fluid equations, gravity must be treated as a conservative force field derived from a scalar potential Φ.

A.6.1 Poisson's Equation

The relationship between a general mass distribution ρ_{mass} and the resulting gravitational potential is defined by the Poisson equation (Binney and Tremaine, 2008):

$$\nabla^2 \Phi = 4\pi G \rho_{\text{mass}}. \tag{A.58}$$

The Laplacian operator ∇^2 (or Δ) is applied according to the cylindrical geometry of the system, as previously defined in Equation (A.7).

A.6.2 Central Point Mass

For the scope of this study, the gravitational potential is dominated by the SMBH. In the numerical implementation, this is treated as a central point mass $M_\bullet$ (Almgren et al., 2010). The potential Φ for such a point source is given by

$$\Phi(r) = -\frac{GM_\bullet}{r}, \tag{A.59}$$

where $r = \sqrt{R^2 + z^2}$ represents the spherical distance from the central singularity.

A.6.3 Gravitational Acceleration in Cylindrical Coordinates

The gravitational acceleration $\boldsymbol{g}$ acting on a fluid element is the negative gradient of the potential $\boldsymbol{g} = -\nabla\Phi$. Expressing this operator in cylindrical polar coordinates according to Equation (A.4) and assuming azimuthal symmetry ($\partial\Phi/\partial\phi = 0$), the acceleration components are

$$g_R = -\frac{\partial \Phi}{\partial R} = -\frac{GM_\bullet R}{(R^2 + z^2)^{3/2}}, \quad g_\phi = 0, \quad g_z = -\frac{\partial \Phi}{\partial z} = -\frac{GM_\bullet z}{(R^2 + z^2)^{3/2}}. \tag{A.60}$$

The resulting volumetric force $\rho\boldsymbol{g}$ is integrated into the momentum conservation equation (A.30). This term provides the necessary centripetal acceleration to balance the centrifugal forces and pressure gradients, thereby maintaining the stability of the rotating nuclear disk (Binney and Tremaine, 2008).

A.7 Wave Propagation

A.7.1 Acoustic Waves

Before discussing shock fronts, it is essential to consider the propagation of small disturbances in a compressible fluid. Infinitesimally small pressure and density perturbations travel through the medium at the local speed of sound, defined as $a = \sqrt{\gamma p/\rho}$, where γ is the adiabatic index, p is the thermodynamic pressure and ρ is the mass density.

As long as the fluid velocity remains subsonic (i.e., the Mach number $\mathcal{M} = v/a < 1$), these disturbances propagate smoothly as continuous acoustic waves. However, when the flow accelerates to supersonic speeds ($\mathcal{M} > 1$), pressure waves can no longer propagate upstream to warn the ambient medium of the approaching gas. Consequently, the continuous wave profile steepens, ultimately forming an abrupt discontinuity known as a shock wave (Kurfürst, 2017).

A.7.2 Rankine-Hugoniot Relations

In the highly supersonic regime typical for early SN expansions, macroscopic fluid properties experience sudden and drastic jumps across the thin shock front. To determine the state of the gas on both sides of this discontinuity, we applied the fundamental conservation laws of mass, momentum, and energy. Assuming a one-dimensional steady flow and neglecting external body forces across the infinitesimally thin shock layer, the hydrodynamic equations in a frame of reference co-moving with the shock front can be written as (Kurfürst, 2017):

$$\rho_1 v_1 = \rho_0 v_0, \tag{A.61}$$

$$\rho_1 v_1^2 + p_1 = \rho_0 v_0^2 + p_0, \tag{A.62}$$

$$\frac{\gamma}{\gamma - 1}\frac{p_1}{\rho_1} + \frac{v_1^2}{2} = \frac{\gamma}{\gamma - 1}\frac{p_0}{\rho_0} + \frac{v_0^2}{2}. \tag{A.63}$$

Here, the subscript 0 denotes the upstream quantities (the non-shocked ambient medium), and the subscript 1 refers to the downstream quantities (the shocked gas). The variable u represents the velocity of the gas flow relative to the shock front.

By algebraically manipulating this system, the relative velocities can be expressed in terms of the pressure and density jumps (Kurfürst, 2017; Zel'dovich and Raizer, 1967):

$$u_0^2 = \frac{\rho_1 (p_1 - p_0)}{\rho_0 (\rho_1 - \rho_0)}, \quad u_1^2 = \frac{\rho_0 (p_1 - p_0)}{\rho_1 (\rho_1 - \rho_0)}. \tag{A.64}$$

Consequently, the density ratio across the shock front is given by

$$\frac{\rho_1}{\rho_0} = \frac{p_1 \frac{\gamma+1}{\gamma-1} + p_0}{p_1 + \frac{\gamma+1}{\gamma-1} p_0}. \tag{A.65}$$

The Strong Shock Limit

During the adiabatic expansion phase of an SNR, the expansion velocity significantly exceeds the local speed of sound, creating a "strong shock" where the downstream pressure is vastly greater than the upstream pressure ($p_1 \gg p_0$). Applying this condition simplifies the density compression ratio to

$$\frac{\rho_1}{\rho_0} = \frac{\gamma + 1}{\gamma - 1}. \tag{A.66}$$

For a monatomic ideal gas ($\gamma = 5/3$), which is the standard approximation for the ISM, the maximum density compression across an adiabatic shock is strictly limited to a factor of 4. Furthermore, the velocity ratio and the downstream pressure in the strong shock limit become

$$\frac{v_1}{v_0} = \frac{\gamma - 1}{\gamma + 1}, \quad p_1 = \frac{2}{\gamma + 1}\rho_0 v_0^2. \tag{A.67}$$

A.7.3 Isothermal Shocks

As discussed in Section 1.2, SNRs eventually transition from the adiabatic Sedov–Taylor phase into the radiative phase. During this later stage, the shocked gas cools highly efficiently through radiative emission. If the cooling timescale is significantly shorter than the dynamical timescale of the system, the thermal energy is radiated away almost instantly behind the shock front.

In this extreme limit, the temperature of the post-shock gas drops rapidly to match the pre-shock temperature ($T_1 \approx T_0$), resulting in an isothermal shock. For an isothermal process, the energy conservation equation is replaced by the condition of constant temperature. Consequently, the density compression across the shock is no longer restricted to the adiabatic limit of 4. Instead, utilizing the isothermal equation of state, the density ratio scales directly with the square of the Mach number (Kurfürst, 2017):

$$\frac{\rho_1}{\rho_0} = \mathcal{M}^2. \tag{A.68}$$

Because the Mach number of SN shocks can be very large, isothermal shocks allow for extremely high compression ratios. This mechanism is crucial for the formation of the dense, cold gas filaments typically observed in older SNRs.

Appendix B

Video Documentation of Simulations

Table B.1: List of SN explosion visualizations and simulation parameters.

ID	Progenitor State	Mass $M_\bullet$ $[M_\odot]$	Distance $[R_g]$	Link (YouTube)
1	Stationary	10^8	10^3	7RtNqmZqwwY
2	Stationary	10^9	10^3	VBieCu0U4r0
3	Stationary	10^9	10^4	y3-tlUnHY2c
4	Stationary	10^8	10^5	c1hz5DkQk7M
5	Orbital- Apocenter	10^8	10^3	qHpHsSG-JLI
6	Orbital- Pericenter	10^8	250	QYwucAJboUI
7	Orbital- Apocenter	10^9	10^3	m-JGojcxEXg
8	Orbital- Pericenter	10^9	250	MyrZyvAITb4
9	Orbital- Apocenter	10^8	10^4	1NVEIO9mIgs
10	Orbital- Pericenter	10^8	2.5×10^3	i9P4v9UkQsE
11	Orbital- Apocenter	10^9	10^4	ETLUhhQMt8k
12	Orbital- Apocenter	10^8	10^5	sTdakGmULN8
13	Orbital- Pericenter	10^8	25×10^3	ukwydDOJgcA

References

Almgren, A. S., Beckner, V. E., Bell, J. B., Day, M. S., Howell, L. H., Joggerst, C. C., Lijewski, M. J., Nonaka, A., Singer, M., and Zingale, M. (2010). CASTRO: A new compressible astrophysical solver. I. hydrodynamics and self-gravity. *The Astrophysical Journal*, 715(2):1221–1238.

Almgren, A. S., Bell, J. B., Colella, P., Howell, L. H., and Welcome, M. L. (1998). A Conservative Adaptive Projection Method for the Variable Density Incompressible Navier-Stokes Equations. *Journal of Computational Physics*, 142(1):1–46.

Arfken, G. B., Weber, H. J., and Harris, F. E. (2012). *Mathematical Methods for Physicists: A Comprehensive Guide*. Academic Press, 7th edition.

Binney, J. and Tremaine, S. (2008). *Galactic Dynamics*. Princeton University Press, 2nd edition.

Bland-Hawthorn, J. and Gerhard, O. (2016). The galaxy in context: Structural, kinematic, and integrated properties. *Annual Review of Astronomy and Astrophysics*, 54(1):529–596.

Blanton, M. R. and Roweis, S. (2007). K-Corrections and Filter Transformations in the Ultraviolet, Optical, and Near-Infrared. , 133(2):734–754.

Branch, D. and Wheeler, J. C. (2017). *Supernova Explosions*. Astronomy and Astrophysics Library. Springer Berlin, Heidelberg.

Chen, X., Braga-Neto, U., Wang, L., Kasen, D., Liu, Z., Roepke, F. K., Zhong, M., and Jeffery, D. J. (2025). *SEDONA*-gesarat: an ai-accelerated radiative transfer program for 3-d supernova simulations. *arXiv preprint arXiv:2507.11767*.

Chini, R., Nielbock, M., Sieutrewicz, R., et al. (2004). The formation of a massive star through the accretion of gas from a disk. *Nature*, 429:67–69.

Colella, P. and Woodward, P. R. (1984). The Piecewise Parabolic (PPM) Method for Gas-Dynamical Simulations. *Journal of Computational Physics*, 54(1):174–201.

Courant, R., Friedrichs, K., and Lewy, H. (1928). Über die partiellen differenzengleichungen der mathematischen physik. *Mathematische Annalen*, 100(1):32–74.

Crocker, R. M., Ali Kazemi, M., Treister, E., Mackey, J., Ong, S. J., Tsuji, K., Yusef-Zadeh, F., Eichmann, B., Eriksen, K. A., Heesen, A., Hörandel, J. R., Maron, G., Merten, L., Nishiyama, T., Ohm, S., Rowell, G., and Ružičková, J. (2020). Supernova remnant feedback and the dynamical evolution of galactic centre clouds. *Astronomy & Astrophysics*, 642.

Draine, B. T. (2011). *Physics of the Interstellar and Intergalactic Medium*. Princeton University Press.

ESO/NASA/ESA (2013). A star explodes: The supernova remnant SNR 0509-67.5. Online. Accessed: 2026-02-22.

Event Horizon Telescope Collaboration (2022). First Sagittarius A* Event Horizon Telescope Results. I. The Shadow of the Supermassive Black Hole in the Center of the Milky Way. *The Astrophysical Journal Letters*, 930(L12).

Event Horizon Telescope Collaboration, Akiyama, K., Algaba, J. C., and others (2021). First M87 Event Horizon Telescope Results. VII. Polarization of the Ring. , 910(1):L12.

Frank, J., King, A., and Raine, D. J. (2002). *Accretion Power in Astrophysics*. Cambridge University Press, 3rd edition.

Genzel, R., Eisenhauer, F., and Gillessen, S. (2010). The galactic center massive black hole and nuclear star cluster. *Reviews of Modern Physics*, 82(4):3121–3195.

Hester, J. J. (2008). The Crab Nebula. *Annual Review of Astronomy and Astrophysics*, 46:127–155. Image credit: NASA, ESA, J. Hester and A. Loll (Arizona State University).

Heywood, I., Rammala, I., Camilo, F., Cotton, W. D., Yusef-Zadeh, F., Abbott, T. D., et al. (2022). The 1.28 GHz meerkat galactic center mosaic. *The Astrophysical Journal*, 930(1):6. Image credit: SARAO.

Kasen, D., Thomas, R. C., and Nugent, P. (2006). Time-dependent monte carlo radiative transfer calculations for three-dimensional supernova spectra, light curves, and polarization. *The Astrophysical Journal*, 651(1):366–380.

Krtička, J., Owocki, S. P., and Meynet, G. (2011). Angular momentum loss from critically rotating stars. *Astronomy and Astrophysics*, 527.

Kundu, P. K., Cohen, I. M., and Dowling, D. R. (2015). *Fluid Mechanics*. Academic Press, 6th edition.

Kurfürst, P. (2015). *Models of hot star decretion disks*. Ph.d. dissertation, Masarykova univerzita, Přírodovědecká fakulta.

Kurfürst, P. (2017). Radiation magnetohydrodynamics. Učební text / Lecture notes, Brno.

Kurfürst, P. (2018). *Astrofyzika supernov*. Masarykova univerzita. Přednáškové materiály / učební text.

Kurfürst, P., Bless, G., Fišák, J., Holoubek, F., Krtička, J., Kubátová, B., Kubát, J., and Zajaček, M. (2026). Supernova interactions with aspherical circumstellar material I: calculations of light curves, AB magnitudes, spectra, and polarisation. *Astronomy & Astrophysics*. manuscript no. main, arXiv:2601.15428v2.

Kurfürst, P., Feldmeier, A., and Krtička, J. (2018). Time-dependent modeling of extended thin decretion disks of critically rotating stars. *Astronomy & Astrophysics*, 613:A75.

Kurfürst, P., Krtička, J., and Feldmeier, A. (2014). Viscous evolution of circumstellar decretion disks. *Astronomy and Astrophysics*, 569.

Kurfürst, P., Pejcha, O., and Krtička, J. (2020). Supernova explosions interacting with aspherical circumstellar material: implications for light curves, spectral line profiles, and polarization. *Astronomy & Astrophysics*, 642:A214.

Landau, L. D. and Lifshitz, E. M. (1987). *Fluid Mechanics*, volume 6 of *Course of Theoretical Physics*. Pergamon Press, 2nd edition.

Li, F.-L., Liu, Y., Fan, X., et al. (2023). Light curves of core-collapse supernovae in agn disks. *The Astrophysical Journal*, 950(161).

Lynden-Bell, D. (1969). Galactic nuclei as collapsed old quasars. *Nature*, 223(5207):690–694.

Miller, G. H. and Colella, P. (2002). A High-Order Lagrangian-Remap Shock-Capturing Scheme for Multi-Fluid Hydrodynamics. *Journal of Computational Physics*, 183(1):26–82.

Mineshige, S. et al. (2009). Review: Accretion disk theory. *ResearchGate*. Schematic diagram of angular momentum transport.

Morris, M. and Serabyn, E. (1996). The galactic center environment. *Annual Review of Astronomy and Astrophysics*, 34:645–701.

NASA, ESA, CSA, and STScI (2022). Mid-infrared view of the nucleus of ngc 628. Image release (PHANGS-JWST team). Image processing: J. Schmidt. Available at: `https://esawebb.org/images/weic2211b/`.

Rees, M. J. (1984). Black hole models for active galactic nuclei. *Annual Review of Astronomy and Astrophysics*, 22(1):471–506.

Schmidt, M. (1963). A star-like object with large red-shift. *Nature*, 197:1040.

Sedov, L. I. (1946). Propagation of strong shock waves. *Journal of Applied Mathematics and Mechanics*, 10:241–250.

Shakura, N. I. and Sunyaev, R. A. (1973). Black holes in binary systems. observational appearance. *Astronomy and Astrophysics*, 24:337–355.

She, J.-Z., Liu, T., Huang, B.-Q., Wei, Y.-F., Li, F.-L., Geng, J.-J., and Wu, X.-F. (2025). Anisotropy of core-collapse supernovae effected by the disks of active galactic nuclei. *The Astrophysical Journal*, 990(17):1–9.

Toro, E. F. (2009). *Riemann Solvers and Numerical Methods for Fluid Dynamics: A Practical Introduction*. Springer, 3rd edition.

Toro, E. F., Spruce, M., and Speares, W. (1994). Restoration of the contact surface in the HLL-Riemann solver. *Shock Waves*, 4(1):25–34.

Urry, C. M. and Padovani, P. (1995). Unified schemes for radio-loud active galactic nuclei. *Publications of the Astronomical Society of the Pacific*, 107:803–845.

van Marle, A. J. and Keppens, R. (2011). Radiative cooling in numerical astrophysics: The need for adaptive mesh refinement. *Computers & Fluids*, 42(1):44–53.

Vink, J. (2012). Supernova remnants: the x-ray perspective. *Astronomy & Astrophysics Review*, 20.

Wheeler, J. C. (2017). *Cosmic Catastrophes: Exploding Stars, Black Holes, and Mapping the Universe*. Cambridge University Press.

Wilson, T. L., Ruf, K., Walmsley, C. M., Martin, R. N., Pauls, T. A., and Batchelor, D. R. (1982). Ammonia in the Galactic center - The structure of the Sgr A cloud. *Astronomy and Astrophysics*, 115:185–195.

Zel'dovich, Y. B. and Raizer, Y. P. (1967). *Physics of Shock Waves and High-Temperature Hydrodynamic Phenomena*, volume 1. Academic Press, New York.

Zhang, W., Almgren, A., Beckner, V., Bell, J., Blaschke, J., Chan, C., Day, M., Friesen, B., Gott, K., Jordan, I., et al. (2019). AMReX: Block-Structured Adaptive Mesh Refinement for Multiphysics Applications. *Journal of Open Source Software*, 4(37):1370.